Visualizing the pH profile inside the catholyte of a CO_2 electrolysis cell

MSc: Sustainable Energy Technology

Maxime Hoogland

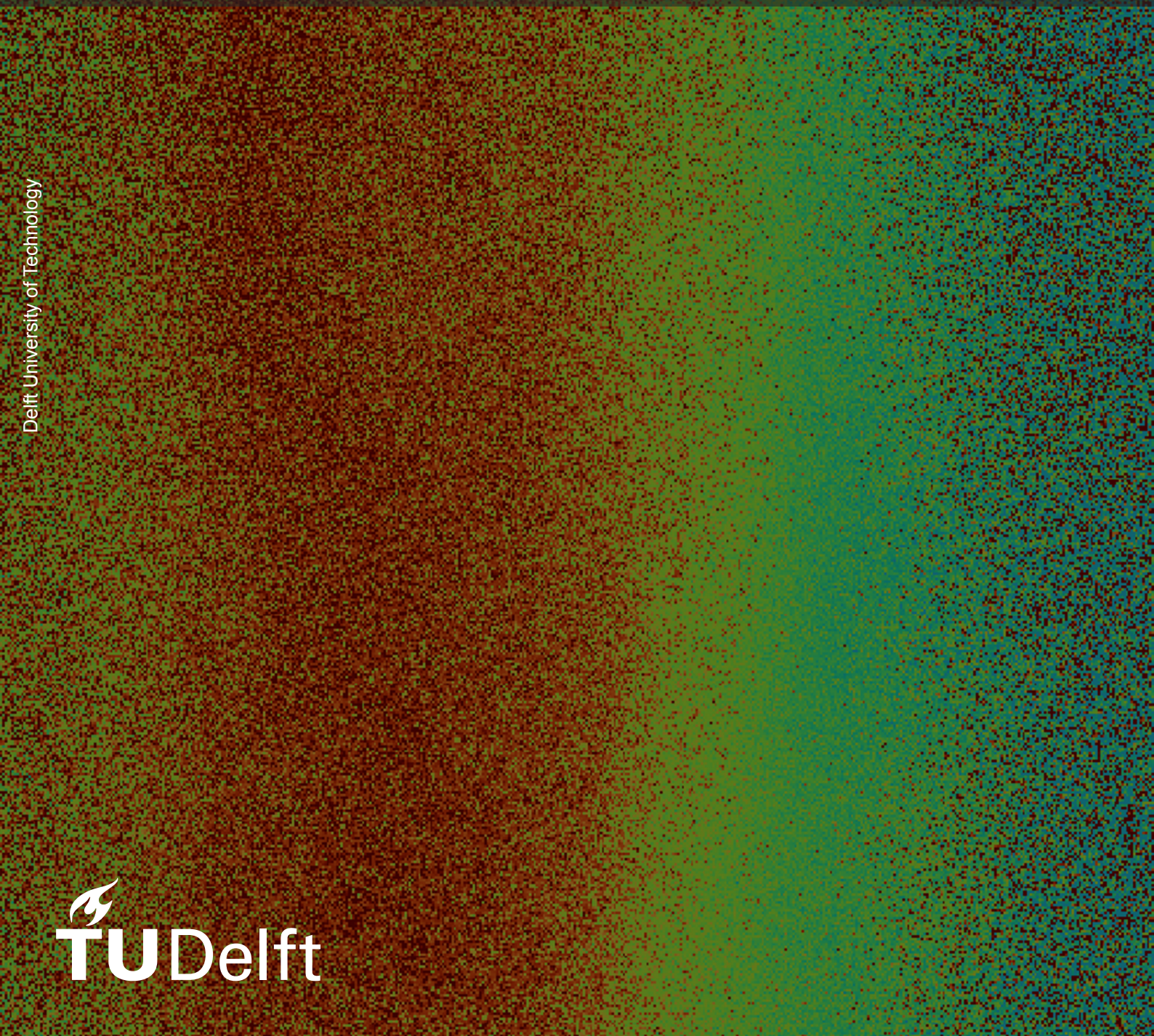

Delft University of Technology

TU Delft

Visualizing the pH profile inside the catholyte of a CO_2 electrolysis cell

by

Maxime Hoogland

to obtain the degree of Master of Science
at the Delft University of Technology,
to be defended on Wednesday May 3, 2023.

Student number:	4397134	
Faculty:	Electrical Engineering, Mathematics & Computer Science (EEMCS)	
Master:	Sustainable Energy Technology	
Tracks:	Energy Storage, Biomass Energy & Economics and Society	
Supervisors:	Dr. D.A. Vermaas	Transport Phenomena, AS
	L.M. Baumgartner	Transport Phenomena, AS
	A.P. Kahn	Transport Phenomena, AS
Thesis Committee:	Dr. D.A. Vermaas	Transport Phenomena, AS
	Prof. Dr. J.J.C Geerlings	Materials for Energy Conversion and Storage, AS
	Dr. W.F. Jager	Advanced Soft Matter, AS
Project Duration:	July, 2021 - May, 2023	
Faculty:	Faculty of Applied Sciences	
Department:	Chemical Engineering	
Section:	Transport Phenomena	
Group:	David Vermaas Lab - Electrochemical Flow Systems	

This thesis is confidential and cannot be made public until May 3, 2023.

TU Delft

Abstract

CO_2 electrolysis to form CO with the use of electricity from renewable sources is a promising technique in closing the carbon cycle. Via the electrochemical reduction CO_2 can be converted into different hydrocarbon products. These value-added products are for example CO, HCOOH, CH_3OH or C_2H_4. The direct electrochemical route of CO_2 reduction is often tested on three metrics: the faradaic efficiency, the current density and the energy efficiency. The implementation of CO_2 reduction has some technical challenges. One of which is controlling the local pH and carbonate formation inside the electrochemical cell producing hydrocarbon products. Controlling the pH inside the electrochemical cell becomes an issue because of the production of hydroxide anions that increase the pH. A high faradaic efficiency is affected by the local pH. With an increasing pH CO_2 is consumed to form carbonate and Hydrogen Evolution Reaction (HER) is favored. Mass transfer limitations result in the pH increasing near the electrode. The local pH is dependent on the electrochemical reaction, buffering reactions inside the electrolyte and mass transfer within the electrolyte flow. Previous studies have used numerical modelling to obtain a 2D transport model to present concentration gradient along the cathode or inside the cathode. Other studies that show the pH experimentally do this using scanning probe techniques or measure the intensity of dye sensitive to pH.

In this project the effects on the local pH are studied with the use of Fluorescence Lifetime Imaging Microscopy (FLIM). This method is able to image the local pH with the use of a fluorescent dye that has a lifetime dependent on the local surroundings. This thesis researched the effects of three process parameters: electrolyte anion type and concentration, the catholyte flow rate and the current density. The electrolytes studied are: 0.1 M $KHCO_3$, 1 M $KHCO_3$ and 0.4 M K_2SO_4. The catholyte flow rates studied are corresponding to Reynolds number 0.8, 8 and 47. The different current densities are -1, -5, -10 and $-50\,\mathrm{mA\,cm^{-2}}$. The effect of these parameters was studied with performing electrochemical tests and studying the cell potential.

This study obtains a fluorescence lifetime-pH calibration curve inside an electrochemical cell. From this calibration curve could be concluded that we have a clear trend above pH 9 to the phase-shift fluorescence lifetime. We also concluded that the used salt $KHCO_3$ is likely to have an effect on the performance of the alpha dye. An unexpected effect of using FLIM onto the spatial resolution in an electrolyser was due to the presence of bubbles. We suggest a more elaborate study into the effects of the settings used in the FLIM method.
The results show that the characteristics affected by the anion type and concentration of electrolytes can be described in the buffer capacity and conductivity of the electrolytes. With increasing buffer capacity and bicarbonate concentration the pH difference between the bulk and near the cathode decreased. The study also found that the overall cell potential was increasing with increasing conductivity of the electrolyte. We cannot distinguish a clear effect of the concentration overpotential as an effect of the buffer capacity onto the overall cell potential.
Additionally, the study found that a higher Reynolds number leads to a decrease in potential due to lower concentration overpotential and better gas removal. From a study on the current density and its effects could be concluded that even though we expect laminar flow with these Reynolds number mass transfer is occurring perpendicular to the flow of the electrolyte. This is an effect of the formation of hydrogen or carbon monoxide bubbles inside the electrolyte that improve mixing. This was also shown in the decrease of pH increase near the cathode with increasing Reynolds number. For the highest current density an overall increase of the bulk pH was linked to the improved mixing due to gas bubbles. The effect of gas bubbles onto the local pH and the cell potential should not be underestimated. Improvement of gas removal with a higher Reynolds number of the electrolyte flow rate or in other ways remains a recommended field of research. We suggest the use of Particle Image Velocimetry along side of FLIM to obtain more insights into the flow profile inside the catholyte affected by the formation and removal of gas bubbles. Finally, we recommend to research the system with the implementation of the gas channel and different types of membranes.

List of Figures

List of Tables

Acronyms

CO_2RR CO_2 Reduction Reaction.

AEM Anion Exchange Membrane.

BPM Bipolar Membrane.

CCUS Carbon Capture, Utilization and Storage.
CE Counter Electrode.
CEM Cation Exchange Membrane.

EE Energy Efficiency.

FE Faradaic Efficiency.
FLIM Fluorescence Lifetime Imaging Microscopy.

GDE Gas Diffusion Electrode.

HER Hydrogen Evolution Reaction.

MEA Membrane Electrode Assembly.
MRE Microreference Electrode.

OER Oxygen Evolution Reaction.

RHE Reversible Hydrogen Electrode.

WE Working Electrode.

Nomenclature

Dimensionless Numbers

Re	Reynolds number	–
Sc	Schmidt number	–
Sh	Sherwood number	–

Greek symbols

β	Buffer capacity	$\mathrm{mol\,L^{-1}}$
κ	Conductivity	$\mathrm{S\,cm^{-1}}$
ν	Kinematic viscosity	$\mathrm{m^2\,s^{-1}}$
ρ	Density	$\mathrm{g\,m^{-3}}$
τ_M	Modulation fluorescence lifetime	ns
τ_ϕ	Phase-shift fluorescence lifetime	ns

Other symbols

A	Electrode area	$\mathrm{m^2}$
c_i	Concentration of species i	$\mathrm{mol\,L^{-1}}$
D	Diffusion coefficient	$\mathrm{m^2\,s^{-1}}$
D_H	Hydraulic diameter	m
E	Potential	V
I	Current	A
i	Current	A
j	Current density	$\mathrm{mA\,cm^{-2}}$
k_m	Mass transport coefficient	$\mathrm{m\,s^{-1}}$
Le	Dimensionless length	–
n_e	The number of electrons in the reaction towards product i	–
N_i	Product reaction rate towards product i	$\mathrm{mol\,s^{-1}}$
R	Resistance	Ω
T	Temperature	K
v	Flow velocity	$\mathrm{m\,s^{-1}}$
W	Width of the channel	m
Z	Height of the channel	m
z_i	The charge of species i	–

Physical constants

F	Faraday constant	$9485\,\mathrm{C\,mol^{-1}}$
R	Universal gas constant	$8.3145\,\mathrm{J\,K^{-1}\,mol^{-1}}$

Contents

1 Introduction

CO_2 electrolysis to form CO with the use of electricity from renewable sources is a promising technique in closing the carbon cycle. This electrochemical reduction is part of a suite of technologies grouped under the name Carbon Capture, Utilization and Storage (CCUS). These technologies are seen as an important aspect of reducing the amount of the greenhouse gas CO_2 present in our atmosphere. In this process the captured CO_2 can be reused together with green hydrogen to produce fuels, plastics and chemicals. As stated by the Dutch government it can be used to obtain negative emissions and is therefore part of their *Klimaatakkoord* as written in 2019 [1]. Especially in the transportation sector and the chemical industry fossil fuel feedstock is still heavily relied upon. Both these sectors show challenges to find alternative feedstocks [2]. The reuse of carbon acts, beside lowering the CO_2 concentration in the air, as a solution to this challenge .

In CCUS CO_2 is captured from the air or from point sources and either stored or reused. Via electrochemical reduction with renewable electricity the captured CO_2 can be converted into different hydrocarbon products. These value-added products are for example CO, HCOOH, CH_3OH or C_2H_4. These products can be converted further with green hydrogen to chemicals. This complete pathway shows challenges for CO_2 reduction when the operating conditions of the other aspects in the pathway are considered [3].

The cell components and feedstock characteristics have a large effect on the performance of the cell [4]. The direct electrochemical route of CO_2 reduction is often tested on three metrics [5]–[7]:

1. the Faradaic Efficiency (FE) towards the desired product,
2. the current density, and
3. Energy Efficiency (EE).

To implement CO_2 reduction on a large scale the following challenges were identified from techno-economic analyses [7][8]. These four challenges of importance are presented here.

1. The high energy requirements to break the bond in CO_2.
2. A high selectivity towards the desired product to limit high separation costs later in the process to materials or fuels.
3. A stable performance of the electrocatalyst.
4. The overall rate of reaction should not be limited by mass transfer. Mass transfer limitations by the consumption of CO_2 are already partly reduced in a gas-fed electrolyser.

A combination of the second and fourth challenge is combined in another main technical challenge: controlling the local pH and carbonate formation inside the electrochemical cell producing hydrocarbon products [5] [7]. A high selectivity or FE is affected by the local pH since with an increasing pH the competing reaction Hydrogen Evolution Reaction (HER) is favored more. Mass transfer limitations result in the pH increasing more near the electrode. Overall, the pH and composition of the electrolyte show a

range of effects on the current density and overpotential [9]. The local pH is dependent on the electrochemical reaction, buffering reactions inside the electrolyte and mass transfer within the electrolyte flow.

$$CO_{2,(aq)} + H_2O + 2\,e^- \rightarrow CO + 2\,OH^- \tag{1.1}$$

Controlling the pH inside the electrochemical cell becomes an issue because of the production of hydroxide anions that increase the pH. These hydroxide anions are produced with the reduction of CO_2 as shown in Equation 1.1. In a CO_2 electrolyser a slightly alkaline pH will lead to the consumption of CO_2 to form bicarbonate and carbonate. When this happens inside the catalyst layer of the GDE the FE towards CO will be lower [10]. The objective of this project is to further investigate the effect of process parameters onto the local pH inside the cell.

Previous work includes numerical modelling of the reactor to obtain insights in the effect of different process parameters. 2-Dimensional transport model is used to present concentration gradients along the flow cell. It also displays the effects of the local pH inside the catalyst layer of the gas diffusion electrode [10]. Others that show the pH inside an electrolyte or at a cathode experimentally use characterization techniques such as scanning probe techniques [11]. Other techniques measure the intensity of a dye that is sensitive to its pH surroundings [12].

The pH characterization technique used in this thesis is Fluorescence Lifetime Imaging Microscopy (FLIM). This method uses the fluorescence lifetime of dye molecules to obtain a 2D image. The fluorescence lifetime of these dye molecules is dependent on the local environment. In this project we aim for a pH dependent lifetime to investigate the local pH. FLIM should not be affected by the intensity of the charged dye molecules being influenced by migration of these molecules inside the cell.

In this thesis we aim to get a better understanding of the influence of the anion type, the concentration and flow rate of the electrolyte on the pH profile and the cell potential in a CO_2 electrolyser. This is done by using FLIM to obtain more insights in the the pH boundary layer near the cathode. The cell potential of the electrochemical cell and parts of the cell are obtained to gather insights on the effects of the process parameters. To achieve this objective the following research questions are posed:

- What is the pH accuracy and spatial resolution of using FLIM in an electrochemical cell?
- What are the effects of the concentration and the anion type of the catholyte on the local and bulk pH inside the catholyte channel?
- What are the effects of the concentration and the anion type of the catholyte on the cell potential?
- What are the effects of the flow rate and thus the Reynolds number of the catholyte on the local and bulk pH inside the catholyte channel?

This study contains the following chapters to answer the research questions:

The theoretical background used in this thesis is presented in chapter 2. It starts with an introduction into CO_2 reduction in an electrochemical cell. This is followed by an overview of the different cell components. Subsequently, mass transport inside the electrolyte is discussed. Next, the cell potential and its different contributors are described. Finally, techniques for local pH measurements and especially the technique FLIM are explained.

In chapter 3 the experimental methods that are used in this project are described. This includes a description of the electrochemical cell set-up, the electrochemical tests and the use of FLIM.

The data that is obtained is shown and discussed in chapter 4. It starts with a discussion of FLIM as the used method. This is followed by showing the effect of the electrolyte concentration and anion type on the local pH and the cell potential. The effect of the current density is shown with the obtained pH profiles over the width of the catholyte channel. Next, the final process parameter, the Reynolds number, and its effects are displayed with the through FLIM obtained images and profiles and effect on the potential.

Finally, in chapter 5 the conclusions are presented based on the obtained results and the recommendations are given in chapter 6.

2

Theory

This chapter gives an introduction to CO_2 reduction. It also describes the most important aspects of reactor engineering of CO_2 reduction. It describes mass transport phenomena inside the electrolyte. Next, an overview of the different parts of the cell potential is given. Finally, the local pH imaging with Fluorescence Lifetime Imaging Microscopy (FLIM) is explained.

2.1. CO_2 reduction in an electrochemical cell

The electrochemical reduction of CO_2 results in different products (e.g., CO, HCOOH, or C_2H_4). The type of catalyst as well as the electrode and the design of the reactor have an effect on the range of products formed [13]. A silver electrode has a higher selectivity towards carbon monoxide (CO) [6] [14]. In this thesis the main product is aimed to be CO. Therefore, the electrochemical reactions that take place during CO_2 reduction towards CO are described.

2.1.1. Cathodic half-cell

The reduction reaction occurs at the cathode. The cathode is the negative electrode in an electrolytic cell. In this thesis is focused on two of the most important reaction that occur in CO_2 electrolysis: CO_2 Reduction Reaction (CO_2RR) towards CO and Hydrogen Evolution Reaction (HER). The reaction are presented with their standard potential against the Reversible Hydrogen Electrode (RHE) [15] [16].

CO_2 Reduction Reaction towards CO

The CO_2RR producing CO follows different pathways dependent on the pH of the local environment. Here, the pathway in a neutral or alkaline environment is given in (Equation 2.1) [16] with its equilibrium potential [14] [8].

$$CO_{2,(aq)} + H_2O + 2\,e^- \rightarrow CO + 2\,OH^- \quad -0.11\,V \text{ vs RHE} \tag{2.1}$$

Hydrogen Evolution Reaction

The competing reaction occurring at the cathode is the Hydrogen Evolution Reaction (HER). The reaction path and its standard potential is as follows [17]:

$$2\,H_2O + 2\,e^- \rightarrow H_2 + 2\,OH^- \quad 0.00\,V \text{ vs RHE} \tag{2.2}$$

Faradaic Efficiency

An important performance target is a high Faradaic Efficiency (FE) [6]. The FE gives the selectivity towards a specific product. The number of electrons to the product i over the total number of electrons in the current applied are the FE. This is given in the following equation:

$$FE_i = \frac{n_e N_i F}{i} \tag{2.3}$$

where FE_i is the Faradaic Efficiency of product i, n_e are the number of electrons needed in the reaction towards this favored product i (-), N_i is the product reaction rate (mol s^{-1}), F is the Faraday constant ($96\,485$ C mol^{-1}) and i is the current (A).

The FE is influenced by different parameters: the catalyst [14], local pH [10] and CO_2 mass transfer which is influenced by the reactor design and electrode design [13].

2.1.2. Anodic half-cell

The anode in an electrolytic cell is the positive electrode. The oxidation reaction occurs at the anode. In CO_2 electrolysis this is the Oxygen Evolution Reaction (OER) displayed in Equation 2.4 [17].

Oxygen Evolution Reaction

$$2\,OH^- \rightarrow \frac{1}{2}\,O_2 + 2\,H_2O + 2\,e^- \quad 1.229\,V \text{ vs RHE} \tag{2.4}$$

2.2. Cell design for electrochemical CO_2 reduction

An electrochemical cell performing CO_2RR consists of multiple components. Also different cell configurations are used which will first be described briefly.

2.2.1. Cell configurations

Main performance indicators of an electrochemical reactor are the Faradaic Efficiency (FE) and the Energy Efficiency (EE) [13]. This means we want both high FE and EE or in other words a high product output at high current density but at low cell potential. The cell configuration or cell design largely affects the electrochemical performance. Different cell designs are made and tested. Two larger umbrella types are depicted: H-cells and flow cell reactors [18] [19]. Under the latter fall again four different types: basic gas fed, Membrane Electrode Assembly (MEA), microfluidic reactor and solid oxide electrolysis reactor (SOEC). Flow cell reactors are reactors with an electrolyte in continuous flow. They have some advantages compared to batch: increase mass transfer, improve mixing and provide better temperature and heat management [4] [19]. Liquid-liquid configurations are limited by maximum achievable current density [20]. The reason for this is the low solubility of gaseous CO_2 into the electrolyte. Therefore is often chosen for a gas-fed cell design.

2.2.2. Cell components

The cell components are described in this section. It is important to note that a choice for each of these components limits the choice for other components. The different components each have their effect on the electrochemical performance of the cell [9].

Cathode: Gas Diffusion Electrode and the Catalyst

A Gas Diffusion Electrode (GDE) is often used in CO_2RR, because when CO_2 is only supplied in its aqueous form it leads to mass transfer limitations for the reduction of CO_2. In this case the HER takes over, because water is plenty available in an water-based electrolyte. Another reason is the rather low concentration of CO_2 in the electrolyte when fully saturated. This leads to gas-fed cell configuration in which a gas channel is present. Between the catholyte channel and the gas channel a GDE is placed. Such an electrode is designed to have gas on one side and a liquid on the other side. A GDE has three layers of which each has its own function: the gas diffusion layer, the micro-porous layer and the catalyst layer.

On the catalyst layer of the GDE the catalyst is coated together with in a binder. Different catalysts result in different products of the electrochemical CO_2 reduction [2] [16] [8] [4]. Ag or Au have CO as a main product. Sn, Pb, Hg or Cd results in the main product being formic acid (CH_2O_2). Cu leads to C_2H_4 as the main product. With the use of a catalyst it also important to keep in mind the abundance of the metal.

Since we want to focus on the reduction of CO_2 towards CO we use Ag nanoparticles coated onto the GDE with Nafion ionomer. A catalyst very often used for the reduction towards CO is Ag [16].

Membrane
A membrane is used to separate the anode and cathode sides of an electrolyzer. The purpose of the membrane is to separate the two sides, mediate the flow of ions from one side to the other and limit product crossover [4]. In its goal to mediate the flow of ions three different types of membranes are typically used [9]. The type of membrane also effect the choice of electrolyte type and concentrations (and thus pH). The membrane also has an effect on the potential drop over over the cell.

- Cation Exchange Membrane (CEM): Positive ions flow from anode to cathode. When using this type of membrane the same electrolyte on both sides should be used otherwise the pH is not stable [13].
- Anion Exchange Membrane (AEM): Negative ions flow from cathode to anode. A stable pH is reported with a membrane electrode assembly as well as typically high performance for CO_2 reduction [21]. However, product crossover from cathode to anode occurs inside a MEA even at relatively low current densities [22]. Next to product crossover the ions that move through the AEM are often ${CO_3}^{2-}$ and ${HCO_3}^{-}$ (present when an alkaline environment gets into contact with CO_2). This results in CO_2 being present in the anode outlet when the ions react with the hydrogen ions because of OER at the anode [23] [24]. This reaction however also leads to a rather stable pH inside the anolyte [23].
- Bipolar Membrane (BPM): Water dissociates inside the membrane and hydrogen ions flow to the cathode and hydroxide ions flow to the anode. This is when the BPM is placed in the reverse bias. When using a BPM a neutral catholyte can be used in combination with an alkaline anolyte [25] [26]. However, when using a BPM a voltage drop is added because of the water dissociation reaction inside the BPM [27].

Anode
The anode in a CO_2 reduction cell performs the OER. Vass, Kormányos, Kószó, *et al.* reviewed multiple articles which used different anode materials and stated that in 47% of the cases Ir was used, 30% used Ni, 14% used Pt. Metals, metal alloys or carbon made up the last 9 % [28]. Often the material used for the anode is dependent on the pH of the anode environment or anolyte solution. Also, the material that is considered for the anode should preferably be a cheap and abundant transition metal.

For CO_2 reduction with a KOH anolyte the abundant available Nickel is often used. Ni is a good catalyst for OER. However, it is only stable in very alkaline solutions [29].

In neutral environments an often used option is Ir. The use of Ir is however not preferred since it a very rare metal. It has good catalytic properties [29]. Beside that it is stable in neutral and lower pH environments. Ir can also be used in alkaline environment since the reaction at the anode neutralizes the solution at the anode surface [30]. We use an Ir coated anode, because of the neutral pH of our electrolyte that we use on both sides.

Apart from the environment the anode is placed in the configuration at the anode side is also important on the effect on the anode material and its stability [28] [31]. This means that the type of membrane and the use of an anolyte layer between membrane and anode or a zero-gap configuration should also have an effect on the choices being made for the anode material.

The structure of the anode is also important especially in combination with the zerogap. The geometries are for example foams or perforated plates. In this thesis we wanted to limit the effect of the gas bubbles at the anode side. Therefore an open woven structure was chosen for the anode geometry that made it easy for gas to be removed from the anode.

Electrolyte
The electrolyte type and the way the electrolyte is supplied in a cell affect the reactions taking place [32] [13]. It affects the selectivity as well as the required overpotential. The choice for the electrolyte is also dependent on the choice for anode and cathode material and membrane type. For example, for a system with two electrolyte compartments (anolyte and catholyte) and a CEM only more acidic anolytes can be used [32].

The faradaic efficiency towards the desired product is influenced by the pH and buffer concentration of the electrolyte [32]. Aside the pH and the buffer concentration, the ionic strength or conductivity of the

electrolyte have an effect on the energy losses over the cell [32]. The conductivity will be discussed more in depth in section 2.4.

Composition In CO_2RR and the production of CO the cation of the electrolyte plays an important role in the reaction mechanism towards CO.

A metal cation helps to stabilize the reaction intermediate. Marcandalli, Monteiro, Goyal, *et al.* state that they found that when only hydrogen ions were present as the cations no CO could be formed even on good catalysts towards CO as for example Ag [34]. Another important effect of the cation is the buffering of the interfacial pH. A cation can be hydrated near the cathode surface. This helps to buffer the pH near the electrode. However, this is only effective if electrolytes are rather neutral, the pKa of the hydrated cation is close to local pH of electrolyte and where the reactant concentration is pH dependent [35]. The pKa of the hydrated cations decreases with size of the cation and thus the buffering capability increases in the order: $Li^+ < Na^+ < K^+ < Rb^+ < Cs^+$ [36].

There are three mechanisms behind the effect of anions on CO_2 reduction [35]:

1. anions can buffer the local pH.
2. anions can donate a proton and play a role in the electrochemical conversion.
3. anions can have an effect on the surface by adsorption and poisoning.

In our project we look at two anions: $KHCO_3{}^-$ and $SO_4{}^{2-}$. The main difference between these two anions is their pKa value. This is described in the first mechanism above. From these values we know that $HCO_3{}^-$ ($pKa = 6.4$) is a better buffer to balance the pH of the electrolyte than $SO_4{}^{2-}$ ($pKa = 1.9$) [37]. This was stated to be the main role of the anion to buffer the pH near the cathode [38].

The second mechanism considers the available proton donors. A higher availability of proton donors result in HER [33]. This is linked to the concentration of anions or proton donors inside the electrolyte. We use two concentrations in this project: 0.1 M and 1 M $KHCO_3$. A higher concentration of anion that can donate a proton would lead to the HER increasing in activity [35]. We have to limit the takeover by HER to obtain a high FE towards CO.

However, Verma, Lu, Ma, *et al.* showed that FE towards CO increased with increasing concentration of the electrolyte [38]. This was independent of the anion type. They suggest the reason for this not being the anion concentration but the cation (K^+) concentration and its stabilization properties. Another important effect of the increasing concentration is the increasing conductivity due to the higher number of ions.

pH The composition of the electrolyte is linked to the pH of the solution. The pH of the electrolyte has an effect on the favoured reactions. Bondue, Graf, Goyal, *et al.* showed that hydrogen evolution is suppressed by the electrochemical reaction of CO_2, because the protons at the surface are used to make water in the consumption reaction with CO_2 [39].

Verma, Lu, Ma, *et al.* showed that an electrolyte with a higher pH such as KOH compared to KCl suppresses HER. This however was thought to be an effect of the anion on the available sites. The hydroxide anions were less likely to directly interact with the surface, while the Cl^- ions directly interacted with the surface of the cathode [38].

Buffer capacity We translate the first mechanism of the anion effect into the buffer capacity of the electrolyte. We calculate a buffer capacity using the van Slyke equation as stated below. The buffer capacity (β) is defined as the moles of OH^- or H^+ per liter of the buffer to change the pH of the buffer with 1 pH units [40].

$$\beta = 2.3 \cdot c_{\text{total}} \frac{K_a \cdot [H^+]}{(K_a + [H^+])^2} \tag{2.5}$$

With c_{total} the total concentration of the buffer, K_a the acid constant and $[H^+]$ the concentration of H^+.

Buffering reactions Aside the buffer capacity we have the effect of the buffering reactions of bicarbonate and carbonate [41]. These are the homogeneous reactions as presented by the following equations. Equation 2.6 and Equation 2.7 mostly occur in alkaline environment and Equation 2.8 and Equation 2.9 in a more acidic. These are followed by the dissociation of water, Equation 2.10.

$$CO_{2,(aq)} + OH^- \rightleftarrows HCO_3{}^- \tag{2.6}$$

$$HCO_3{}^- + OH^- \rightleftarrows CO_3{}^{2-} + H_2O \tag{2.7}$$

$$CO_{2,(aq)} + H_2O \rightleftarrows H^+ + HCO_3{}^- \tag{2.8}$$

$$HCO_3{}^- \rightleftarrows CO_3{}^{2-} + H^+ \tag{2.9}$$

$$H_2O \rightleftarrows OH^- + H^+ \tag{2.10}$$

The reaction rate constants in these reactions are given in Table 2.1. From these reaction rate constants as well as the stoichiometry in the reactions we see that bicarbonate has a buffering effect. This bicarbonate and carbonate are already present when a liquid is saturated with CO_2.

Table 2.1: Overview of reaction rate constants [42].

Reaction equation	Forward rate constant	Backward rate constant
Equation 2.6	$2.23\,\mathrm{m^3\,mol^{-1}\,s^{-1}}$	$5.23 \times 10^{-5}\,\mathrm{s^{-1}}$
Equation 2.7	$6 \times 10^{6}\,\mathrm{m^3\,mol^{-1}\,s^{-1}}$	$1.25 \times 10^{6}\,\mathrm{s^{-1}}$
Equation 2.8	$3.71 \times 10^{-2}\,\mathrm{s^{-1}}$	$8.7 \times 10^{1}\,\mathrm{m^3\,mol^{-1}\,s^{-1}}$
Equation 2.9	$5.94 \times 10^{1}\,\mathrm{s^{-1}}$	$1.24 \times 10^{9}\,\mathrm{m^3\,mol^{-1}\,s^{-1}}$
Equation 2.10	$1\,\mathrm{mol\,m^{-3}\,s^{-1}}$	$1 \times 10^{8}\,\mathrm{m^3\,mol^{-1}\,s^{-1}}$

2.3. Mass transport inside the electrolyte channel

There are three modes of mass transfer for charged species inside an environment under an electrical potential:

1. Diffusion: Transport because of concentration gradient.
2. Migration: Transport of a charged species under the influence of a gradient of electrical potential.
3. Convection: Natural or forced convection.

In Equation 2.11 the Nernst-Planck equation is given [15]. In this equation the total flux is given by three terms. The first term is the flux because of diffusion, second term because of migration and final term due to convection.

$$J_i(x) = -D_i \frac{\delta c_i(x)}{\delta x} - \frac{z_i F}{RT} D_i c_i \frac{\delta \phi(x)}{\delta x} + c_i v(x) \tag{2.11}$$

In this equation $J_i(x)$ is the flux of species i at distance x from the surface, D_i is the diffusion coefficient of species i, $\frac{\delta c_i(x)}{\delta x}$ is the concentration gradient at distance x, z_i is the charge, c_i is the concentration of species i, $\frac{\delta \phi(x)}{\delta x}$ is the potential gradient at distance x and $v(x)$ the velocity. It also contains F the Faraday's constant, T temperature and R the gas constant.

This equation is important because it describes all three modes of mass transport. From literature is known that the FE towards CO is limited because of mass transfer [7] [8]. This is mostly because of the flux of reactant towards the cathode as well as removal of the product of the reaction away from the cathode. When the CO_2 concentration near the cathode is low it will limit the reaction, because the reaction is dependent on concentration of reactant species. HER will take over because water is available in abundance. Another effect when the products of the reaction are not taken away from the cathode is the following. When the hydroxide anions are not taken away from the electrode, the pH increases near the electrode. It leads to the consumption of aqueous CO_2 and limits the reaction towards CO and promotes HER.

There are multiple ways to improve mass transport towards the electrode as well as away from the electrode inside the electrolyte channel:

- Irregularities in the electrode surface.
- Irregularities in the electrolyte flow.
- The effect of the flow profile which can be related to the Reynolds number and other dimensionless numbers.

The third way to improve mass transport is described in the next section with the explanation of dimensionless numbers. This is followed by an overview of the mass transport correlations.

Dimensionless numbers

Reynolds number The Reynolds number is defined as the ratio between inertial and viscous forces in a flowing liquid [43].

$$Re = \frac{vD_H}{\nu} \tag{2.12}$$

with ν the kinematic viscosity of the liquid ($m^2\,s^{-1}$), v the flow velocity ($m\,s^{-1}$) and D_H the hydraulic diameter (m).

The hydraulic diameter is often used to describe a non circular pipe. The equation is given by:

$$D_H = \frac{4A}{P} = \frac{2WZ}{W+Z} \tag{2.13}$$

with $A = WZ$ the area in m^2 and $P = 2(W+Z)$ the perimeter in m. W is the width of the channel and Z the height of the channel both in m.

Schmidt number The Schmidt number represent the ratio between the momentum diffusivity and the mass diffusivity [43]. It can also be described as the relation between the relative velocity and concentration boundary layer thicknesses.

$$Sc = \frac{\nu}{D} \tag{2.14}$$

with ν the kinematic viscosity ($m^2\,s^{-1}$) of the liquid and D the diffusion coefficient ($m^2\,s^{-1}$).

Sherwood number Sherwood number is used in representing mass transport in electrochemical reactors. Dimensionless concentration gradient at the surface. It gives the ratio between convective mass transfer to diffusive mass transport [43]. It can also be described as a function of the Reynolds and Schmidt numbers or the Sherwood Schmidt Reynolds correlation. The Sherwood number increases with increasing convective mass transfer, increasing characteristic length and decreasing mass diffusivity.

$$Sh = \frac{k_m D_H}{D} \tag{2.15}$$

with k_m the mass transport coefficient, D_H the hydraulic diameter and D the diffusion coefficient.

Mass transport correlations

The Sherwood number can be described as a function of the Reynolds, Schmidt and the dimensionless length ($Le = \frac{L}{D_H}$, L the length of the electrode in the direction of the flow and D_H the hydraulic diameter):

$$Sh = aRe^b Sc^c Le^d \tag{2.16}$$

The cell is designed such that the flow at the electrode is a fully developed laminar flow meaning that the velocity boundary layer over the whole electrode length is stable. The concentration boundary layer however is not yet fully developed. With low Re numbers the flow is laminar. Which means there should be no convection in the y-direction.

Local mass transfer coefficient (k_m) changes with the length of the electrode since the boundary thickness changes also still with the length of the electrode.

$$k_m = \frac{-D \frac{\delta C_i}{\delta y}|_{y=0}}{C_{i,s} - C_{i,\infty}} \tag{2.17}$$

This equation shows that the concentration in the boundary layer in comparison to the bulk concentration influences the mass transfer coefficient. This coefficient determines the rate of species transfer from or towards the boundary layer by convection.

$$k_m = \frac{n_i}{A \Delta C_i} \tag{2.18}$$

Since k_m is dependent on the concentration boundary layer it will be affected by migration and the homogeneous reactions. As well as forced convection because of bubbles.

For a set of conditions a mass transport correlation is given. The conditions are: fully developed laminar flow, $58 < Re < 2000$, $2850 < Sc < 5140$, $0.17 < Le < 12.5$ and $S/B = 0.167$ or 0.175 [44].

$$Sh = 2.54 Re^{0.3} Sc^{0.3} Le^{0.3} \tag{2.19}$$

Theoretically derived for fully developed laminar flow assuming infinitely wide electrodes ($ReSc(D_H/L) > 10^4$ and $Le \leq 35$):

$$Sh = 1.85 \chi Re^{1/3} Sc^{1/3} Le^{1/3} \tag{2.20}$$

χ corrects for a finite width between the electrodes [45].

From the Sherwood-Reynolds-Schmidt correlation makes it possible to calculate the mass-transfer coefficient for modeling purposes. From [46]:

$$k_m = \left(\frac{D}{L}\right) 0.664 \left(\frac{vL}{\nu}\right)^{1/2} \left(\frac{\nu}{D}\right)^{1/3} \tag{2.21}$$

Hashiba, Weng, Chen, *et al.* shows the effect of the buffer capacity of the electrolyte on the reactant species at the cathode surface with the use of simulations. They show that the thickness of the boundary layer has an important effect of the mass transport of the reactant species, CO_2 [47]. Others have used numerical modelling to show a 2D image of the concentration inside the electrolyte near the cathode [10] [46].

2.4. Cell potential

A low cell potential is an important performance target [6]. This cell potential is incorporated in the Energy Efficiency (EE) of a system. The energy efficiency is described as follows: a comparison of the energy that is chemically-bonded and leaving the system as a product and the electrical energy supply.

In this concept the Faradaic Efficiency (FE) is integrated. This concept is explained in subsection 2.1.1. The EE is the product of this FE and the voltage efficiency. The voltage efficiency is made up of the thermodynamic cell voltage divided by the actual cell voltage. Combining this gives:

$$EE = \frac{\sum_i E_i^0 FE_i}{E_{cell}} \tag{2.22}$$

With EE the energy efficiency, $E^0_{\text{cell,i}}$ the equilibrium cell potential for product i, FE_i the faradaic efficiency towards product i and E_{cell} the cell potential. This shows the importance of the cell potential and its large effect on the energy efficiency.

The cell potential (E_{cell}) is made up of multiple parts: the standard potentials as well as multiple overpotentials. These are anodic and cathodic kinetic activations, mass transport limitations and the ohmic resistances (over anode, cathode, membrane and electrolytes) [8] [48]. Next these different contributions to the cell potential are discussed.

Standard potential The standard potential of a cell (E^0_{cell}) is correlated to the standard Gibbs free energy change (ΔG^0):

$$\Delta G^0 = -nFE^0_{\text{cell}} \tag{2.23}$$

with n the number of electrons transferred in the cell reaction and F the Faraday constant.

Equilibrium potential The equilibrium potential is given by the Nernst equation for the complete cell [15]:

$$E_{\text{cell}} = E^0_{\text{cell}} + \frac{RT}{n_e F} \ln Q \tag{2.24}$$

with E^0_{cell} the standard cell potential, R the gas constant, T the temperature, n_e the stoichiometric number of electrons involved in the reaction. And finally, Q the reaction quotient.

Ohmic overpotential Ohmic overpotential is a result of ohmic internal resistances inside the electrochemical cell. These resistances are inside the electrodes, the electrolyte, the membrane. Also outside the actual cell are resistances such as the contact and the current collectors of the electrodes. This overpotential is displayed in the following formula:

$$\eta_{\text{ohmic}} = iR \tag{2.25}$$

Here, η_{ohmic} is the ohmic overpotential, i the applied current (A), R the internal resistance. From this is seen that the overpotential increases linearly with the applied current. Ohmic overpotentials can be limited by electrode design, conductivity of used materials and reactor design.
One of the design choices and its effect is shown in the equation that describes the ohmic drop over the electrolyte:

$$\eta_{\text{electrolyte}} = \frac{jl}{\kappa} \tag{2.26}$$

with j the current density (mA cm^{-2}), l the length of the electrolyte (cm) and κ the conductivity of the electrolyte(S cm^{-1}). This length of the electrolyte can be described as the path the the electrons have to travel to go from one side to the other. In short a thinner electrolyte would theoretically result in a smaller ohmic drop over the electrolyte channel. However, the path can also be affected by the presence of gas bubbles inside the electrolyte. This effect will be described later.

Activation overpotential The activation overpotential to produce a specific current is defined as the difference between in potential in comparison to the equilibrium potential to overcome the activation energy of the cell. The activation overpotential can be taken from the Butler-Volmer equation where the current (i) is given as a function of the activation overpotential (η_{a}):

$$i = i_0[\exp\left\{-\frac{\alpha n F \eta_{\text{a}}}{RT}\right\} - \exp\left\{\frac{(1-\alpha n F \eta_{\text{a}})}{RT}\right\}] \tag{2.27}$$

with i_0 the exchange current, α the transfer coefficient, n the stoichiometric number of electrons involved, F Faraday constant, R gas constant and T the temperature. Rewriting this equation gives a function for the activation overpotential:

$$\eta_{\text{a}} = \frac{RT}{\alpha n F} \ln i_0 - \frac{RT}{\alpha n F} \ln i \tag{2.28}$$

Concentration overpotential The concentration overpotential is because of the concentration difference between the bulk electrolyte and on the electrode surface. This overpotential increases when the reactions are fast but mass transfer is slow. Concentration overpotentials can be reduced by improving mass transfer.

The concentration overpotential is described by a part of the Nernst equation [49]:

$$\eta_{\text{conc}} = \frac{RT}{nF} \ln \frac{c_{\text{surface}}}{c_{\text{saturated}}} \tag{2.29}$$

The effect of bubbles Gas bubbles have effects on the ohmic overpotential, activation overpotential and the concentration overpotential.

- Ohmic overpotential affected by bubbles on the electrode: Surface-attached bubbles will not only impose an added resistance by preventing current to reach a portion of the electrocatalytic area, but they will induce a non-uniform current density distribution in the area adjacent to the bubbles, affecting the charge transfer and overall overpotential losses in those regions [50].
- Ohmic potential affected by bubbles dispersed in bulk phase of electrolyte: A relation between the effective conductivity and conductivity in absence of bubbles can be described by a relation of the bulk void fraction [50], [51]. Different relations between the gas bubble volume fraction and the ratio between the conductivity in the absence of bubbles and the effective electrolyte conductivity are for example linear or Bruggeman.

$$\frac{\kappa}{\kappa_0} = \begin{cases} (1-\epsilon_\mathrm{b}) & \text{Linear} \\ (1-\epsilon_\mathrm{b})^{1.5} & \text{Bruggeman} \end{cases} \tag{2.30}$$

- Activation overpotential affected by attached bubbles: In gas evolving electrodes, attached bubbles effectively decrease the electrocatalytic surface, resulting in an increase in overpotential for a given current density. Relation between the fractional bubble coverage of electrode (σ) and the current density [50]:

$$j = \frac{i}{A(1-\sigma)} \tag{2.31}$$

- Concentration overpotential affected by gas bubbles in the electrolyte: Bubbles may decrease the concentration overpotential by absorbing dissolved gas products and decreasing supersaturation levels in the electrolyte.
- Concentration overpotential affected by gas bubbles growing and detaching: The growth and detachment of gas bubbles leads improved convective mass transfer [50]. This minimizes the concentration differences and therefore the concentration overpotential.

2.5. Techniques for local pH measurements in electrochemistry

As stated in subsection 2.2.2 the local pH has an effect of the reactions taking place. Because of this it is interesting to see the effect of the current applied onto the local pH. An interesting example is the research into the dependence of the local pH onto the applied potential [52]. Henckel, Counihan, Holmes, *et al.* have studied the local pH on a Cu electrode in a flow cell under the influence of a potential. This was studied using Raman spectroscopy. This technology is an example of a technique used to visualize the local pH at an electrode.

Visualisation of the pH profile at an electrode also gives more insight in the mass transport inside the cell as well as the buffer capacity of the electrolyte. Monteiro and Koper gave an overview of the different measuring techniques used in electrochemistry in 2021. Based on this article an overview is given in Table 2.2.

Aside from using these techniques individually combinations of methods are also used in research. These techniques have both drawbacks and benefits compared to each other.

Scanning probe techniques

A major drawback of the scanning probe techniques is that it is an invasive technique. The used probe can have effects on the concentration profile that is being measured [11]. Its advantages are the range of pH that can be studied and the high spatial resolution that can be obtained. This last is however dependent on the location of the probe.

Fluorescence microscopy

In comparison to the scanning probe techniques fluorescence microscopy is relatively non-invasive. However, the added fluorescent particles into the electrolyte can affect the electrolyte and change the composition. Another drawback is that the pH range that can be investigated is dependent on the

Table 2.2: An overview of some of the techniques discussed by Monteiro and Koper grouped in two types of methods: direct or indirect measurements [53].

Local pH measurement techniques	
Direct method **Monitor proton concentration** **Scanning probe techniques**	**Indirect method** **Monitor species dependent on proton concentration** **Optical techniques**
Scanning Electrochemical Microscopy (SECM)	Fluorescence microscopy Confocal laser scanning microscopy
Scanning Ion Conductance Microscopy (SICM)	Infrared absorption spectroscopy
Scanning Ion-selective Electrode Technique (SIET)	Raman spectroscopy

species that are used for the fluorescence measurements. The pH range is typically determined by the specific pKa of the indicator used.

Time-resolved confocal fluorescence microscopy was successfully done to obtain insights into the pH change near an electrode because of the reduction of oxygen when a current is applied [12]. In this case the intensity of the dye is used to calculate the pH Pande, Chandrasekar, Lohse, *et al.* conclude that the fluorescent dye molecules are influenced by the concentration of the electrolyte. This is due to migration. This effects the concentration of the dye molecules which in its way influences the intensity of the dye molecules.

The fluorescence microscopy methods as discussed by Pande, Chandrasekar, Lohse, *et al.* and Monteiro and Koper use the intensity of the dye molecules to convert to the pH profile. In biological research a different technique with fluorescence microscopy is used to dictate the local environment. This method can also be used to determine the pH profile in a sample. The technique uses the dependency of the lifetime of dye molecules on the local environment [54]. The method is called Fluorescence Lifetime Imaging Microscopy (FLIM) and will be further explained in the next section.

2.6. Fluorescence Lifetime Imaging Microscopy

Fluorescence Lifetime Imaging Microscopy (FLIM) was first used by Lakowicz, Szmacinski, Nowaczyk, *et al.* They used fluorescence lifetime measurements in combination with 2D imaging to obtain an image which showed the different lifetimes measurements as contrast in this image [54]. The use of FLIM has some great advantages compared to fluorescence microscopy based on the intensity of the dye molecules:

- FLIM is largely independent of the concentration of the fluorescent molecules.
- FLIM is largely independent of the laser intensity.
- FLIM is largely independent of any reflections inside the liquid due to for example bubbles.

As described in the section before and as the name Fluorescence Lifetime Imaging Microscopy (FLIM) suggest the technique uses the lifetime of the dye molecules and its dependency on the local environment to obtain the profile of the sample. Therefore we will first introduce the fluorescence lifetime.

2.6.1. Fluorescence lifetime

In Figure 2.1 a schematic of the Jablonski diagram is displayed. This diagram illustrates the different levels of excitation an electron can be in as well as the different phenomena that occur when it changes from one level to another. The excitation of an electron happens when light is absorbed by a molecule at ground state. The energy of this light should be at least as big as the higher energy levels. After the excitation the electron it releases some energy via vibrational relaxation. When the electron is at the lowest level of the excited levels fluorescence can occur. The photon that is now emitted has a lower energy than the photon that was absorbed. The light that is emitted is of a longer wavelength than the absorbed light. This is known as Stokes' shift. The average time before the fluorophore emits a fluorescence photon after excitation is known as the fluorescence lifetime (τ). The lifetime is recorded in one of two ways: time-domain or frequency-domain.

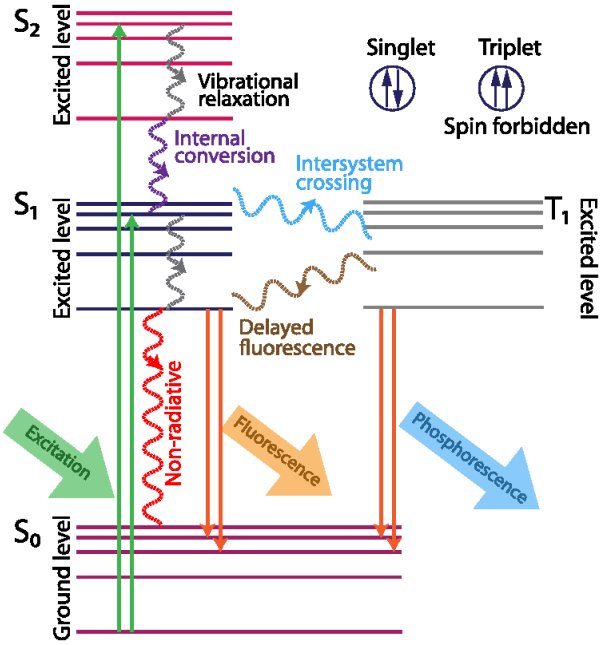

Figure 2.1: A schematic of the Jablonski diagram (Datta, Heaster, Sharick, *et al.* 2020)

2.6.2. Time-Domain vs Frequency-Domain

Time-domain FLIM

In time-domain measurements the decay of the fluorescence is recorded after the sample has been illuminated with a single short pulse of light. The fluorescence intensity after the very short pulse of light is described by the following equation:

$$I_{\text{pulse}}(t) = \frac{1}{\tau} \cdot \exp\left\{\frac{-t}{\tau}\right\} \tag{2.32}$$

Frequency-domain FLIM

For frequency-domain measurements the sample is continuously illuminated with sinusoidally modulated excitation light. The light that is emitted by the sample also comes back in this periodic character but it is shifted, so called phase-shift ($\Delta\phi$), and there is a decrease in the modulation depth ($M = \frac{AC_E}{AC_E}$). The way of recording used for this thesis is with these frequency-domain measurements. With the use of these two changes in the fluorescent light that comes back the lifetime is determined.

$$\tau_\phi = \frac{\tan(\phi_{\text{em}} - \phi_{\text{ex}})}{\omega} \tag{2.33}$$

$$\tau_{\text{M}} = \frac{1}{\omega}\sqrt{\frac{1}{(\frac{M_{\text{em}}}{M_{\text{ex}}})^2 - 1}} \tag{2.34}$$

The lifetime is displayed by τ with its subscript indicating if it is calculated from the phase shift (ϕ) or the modulation depth (M). To calculate the lifetime from the phase shift or the modulation both the phase or modulation depth of the emitted (ϕ_{em} or M_{em}) and the excitation (ϕ_{ex} or Mex) light are needed. ω indicates the angular frequency at which the light is modulated.

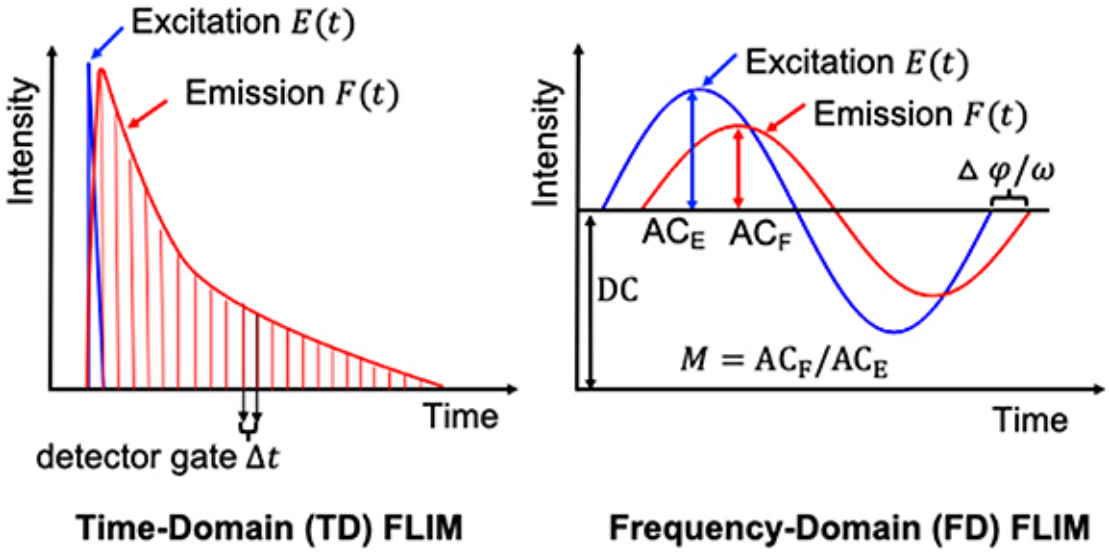

Figure 2.2: Two illustrations to display the difference between time-domain (*left*) and frequency-domain (*right*) measurements. Figure by A. Kahn (2022).

2.6.3. Fluorescent dyes

In FLIM fluorescent dye is mixed into the solution. A dye will be used which has a lifetime which is different depending on the environment around the dye. This is promising for the use of FLIM in combination with pH measurements in an electrochemical cell. If we want to study the pH a dye with a lifetime dependent on the pH is to be used. Since the technique so far is mostly used in biological research the range at which most commonly used dyes are active is around a neutral pH. However, in the case of CO_2 reduction the pH range will be a lot more alkaline. For this reason a dye that has a pKa more in the alkaline region is needed. The dye that is being used in this thesis is the α-dye. This molecule will be further discussed in chapter 3.

3

Methods

This chapter describes the methods used to perform the electrochemical tests and to perform the FLIM on the electrochemical cell.

3.1. Electrochemical cell set-up to perform CO_2 reduction

Firstly, an overview of the electrochemical cell that is used is presented. This is followed by an overview of the different process parameters that were studied in this project. Finally, a description of the electrochemical experiments performed in this project is given.

3.1.1. Electrochemical cell for CO_2 reduction

A schematic overview of the cell configuration used to perform the electrochemical tests is presented in Figure 3.1. The cell consists of the two electrodes, two electrolyte compartments and the membrane. In Figure A.1 a more detailed representation of the cell is shown.

Our Working Electrode (WE) is a Gas Diffusion Electrode (GDE) with silver nanoparticles deposited on the carbon microporous layer of the GDE with a Nafion content of 20wt%. The GDE used had a loading of $1.24\,\mathrm{mg\,cm^{-2}}$. The GDE has a carbon cloth diffusion layer (ELAT LT1400W). This was chosen for its sturdiness inside the cell. We use Ag as the electrocatalyst on the cathode to achieve electroreduction favored towards CO. The coated side of the electrode is facing the catholyte compartment. On the back side of the GDE, Cu tape is secured functioning as the current collector. Silicone glue ensures the catholyte compartment is leak free. It also limits the active area of the cathode to $1\,\mathrm{cm^2}$. Since the used cell can also be operated as a gas-fed system it also contains a gas channel. In this project no gaseous CO_2 was used, so therefore the gas channel is sealed of from the rest of the cell.

The Counter Electrode (CE) is a Ti mesh coated with a $1\,\mu$m layer of Pt that is stable in a neutral environment. The structure of the anode can be described as an open woven structure. At the CE the oxygen evolution reaction takes place. This electrode is in contact with the stainless steel casing of the cell which was used as the current collector. The reference electrodes are both leak-free Ag/AgCl electrodes. One Microreference Electrode (MRE) is placed in a T-union at the inlet of the catholyte. The other MRE is placed through the stainless steel casing, through the anode and almost touching the membrane. Doing this positions the MRE between the anode and the membrane. The membrane is located between the anode and the catholyte compartment, creating a zerogap configuration for the anode side. The membrane used is an anion exchange membrane (Selemion AMV).

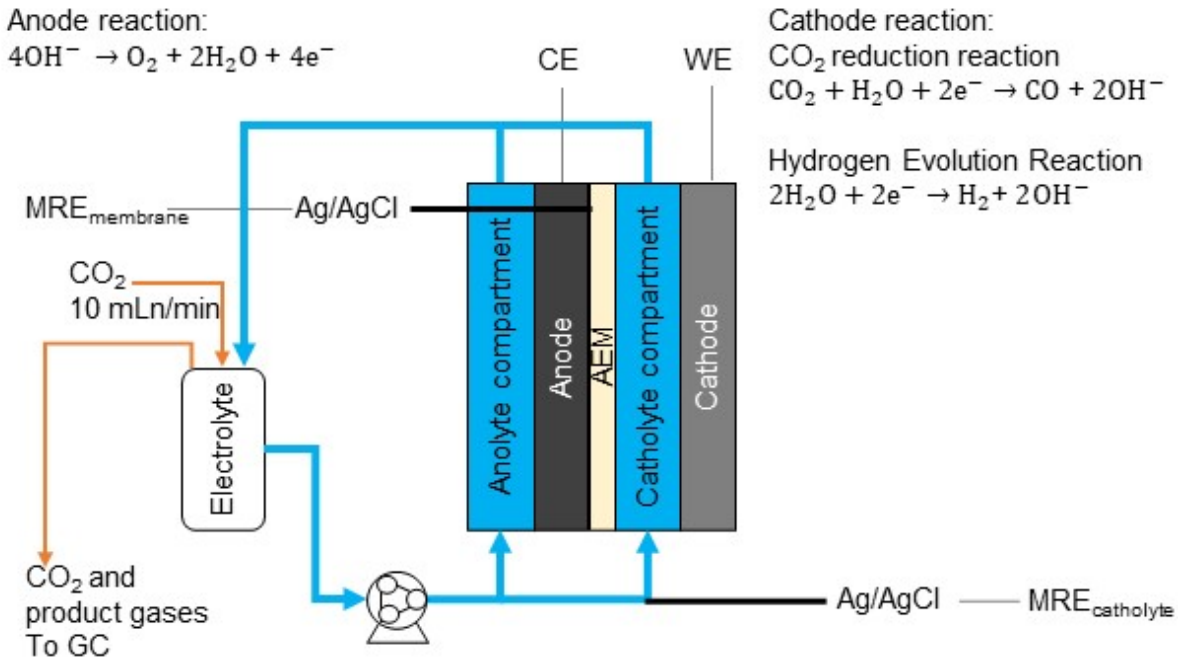

Figure 3.1: A schematic of the cell set-up. The blue lines indicate the pumped flow of the anolyte and catholyte from the electrolyte bottle to the cell and from the cell back to the electrolyte bottle. The orange lines show the gas flow from the gas bottle to continuously saturate the electrolyte and purge the product gasses. From the electrolyte bottle the orange line shows the CO_2 and product gases which can be sampled for GC injection. The schematic also indicates the CE and acrshortwe at the anode and cathode respectively. The two Ag/AgCl MREs are also shown in the schematic. One of which directly measures at the membrane and the other measures inside the inlet of the catholyte flow.

Three different widths of catholyte channels thicknesses were used. For now we focus on the $2\,\text{mm}$ thick flow channel. The height of the channel is $4\,\text{mm}$. To be able to view the inside of the electrolyte channel with FLIM the channel was cut with a diamond milling bit out of a PMMA sheet.

The two liquid electrolytes (anolyte and catholyte) were flowing from bottom to top inside the cell. This was done to help gas removal from the flow channels. These electrolytes were pumped through the cell with a peristaltic pump. Both the electrolytes come from the same electrolyte container and flow back into this container while continuously being stirred by a magnetic stirrer and purged by a CO_2 gas stream.

3.1.2. Overview of process parameters

Electrolyte

Three types of electrolytes were used varying in anion type and concentration:

- 0.4 M K_2SO_4
- 0.1 M $KHCO_3$
- 1 M $KHCO_3$

All three of the electrolyte had a $100\,\mu\text{mol}\,\text{L}^{-1}$ concentration of the so-called alpha dye and were continuously purged with CO_2 at $10\,\text{mL}_\text{n}/\text{min}$ to keep full saturation and flush out any product gases.

Reynolds number or the catholyte flow rate

The Reynolds number varies between three numbers: $Re = 0.8, 8$ and 47. The Reynolds number is obtained by varying the liquid flow rate of the catholyte (F_L). For the three different catholyte channel thicknesses this means different flow rates. The Reynolds number is calculated from the liquid velocity ($u = \frac{F_L}{WD}$ in $\text{m}\,\text{s}^{-1}$), the hydraulic diameter (D_H in m) and the kinematic viscosity (ν) as follows in Equation 3.1. For the kinematic viscosity we assumed the value for water at $20\,°\text{C}$, $\nu = 1 \times 10^{-6}\,\text{m}^2\,\text{s}^{-1}$.

$$Re = \frac{uD_H}{\nu} \tag{3.1}$$

The hydraulic diameter was calculated from the width (W, different for each thickness) and height ($H = 4$ mm) of the channel.

$$D_H = \frac{2HW}{H+W} \tag{3.2}$$

Table 3.1: An overview of the flow rates used for the different channel width to achieve the three desired Reynolds numbers in this project.

Channel width [mm]	D_H [mm]	F_L [mL min^{-1}]		
		$Re = 0.8$	$Re = 8$	$Re = 47$
2	2.7	0.14	1.4	8.5
1	1.6	0.12	1.2	7
0.25	0.5	0.1	1	6

Current density
Each of the parameter sets were tested electrochemically at four different current densities. These four are $-1, -5, -10$ and -50 mA cm^{-2}.

Channel width
Three channel widths were planned to be used in this project. These three catholyte compartments were designed with a thickness of 2, 1 and 0.25 mm.

3.1.3. Electrochemical experiments

As a preparation for the electrochemical tests the cell was assembled and tested for leaks. Next, the electrolyte was saturated with CO_2. The electrolyte bottle was connected to the cell while continuously feeding CO_2 into the liquid. After 1 hour of saturating the electrolyte the pH was measured of the electrolyte to check if it was fully saturated as well as for comparison to the obtained pH with FLIM later. Afterwards the lines were again connected and with the use of the mass flow meter at the gas outlet the leak tightness of the system was checked. When this was achieved a gas sample was taken to be analysed with gas chromatography.

The IviumStat.h potentiostat by Ivium technologies was used to set four steps of current density. In each step we have 30 min for the system to become steady state. To start the program an open cell voltage was set for 60 s. This was followed by a current control at -1 mA cm^{-2}. To ensure steady state we let it stabilize for 30 min before taking multiple FLIM images at all three of the positions inside the cell. In this time also three gas samples were taken to be analysed with gas chromatography. To finalize this first step the cell was put under open cell voltage for 5 min and the cell was flushed with a high liquid flow rate to achieve full gas removal inside the system. This was repeated for the rest of the current densities: $-5, -10$ and -50 mA cm^{-2}.

With the use of the obtained current and potential data from Ivium we could perform calculations to obtain the cell potential as well as potentials over parts of the cell.

3.2. Fluorescence Lifetime Imaging Microscopy

The pH profile was determined using a technique called Fluorescence Lifetime Imaging Microscopy (FLIM). This measurement technique uses the lifetime of the dye molecule and its dependency on the local environment to obtain an image of the sample. In this project the phase-shift fluorescence lifetime is converted to the pH to obtain pH images and profiles over the catholyte channel inside the electrochemical cell.

3.2.1. The FLIM system

The used FLIM set-up consists of multiple components. A picture of the set-up is shown in Figure 3.2. A schematic is given in Figure 3.3 with the blue lines indicating the in going light as coming from the laser and the green lines the fluorescent light as emitted by the dye molecules and being recorded by the FLIM camera.

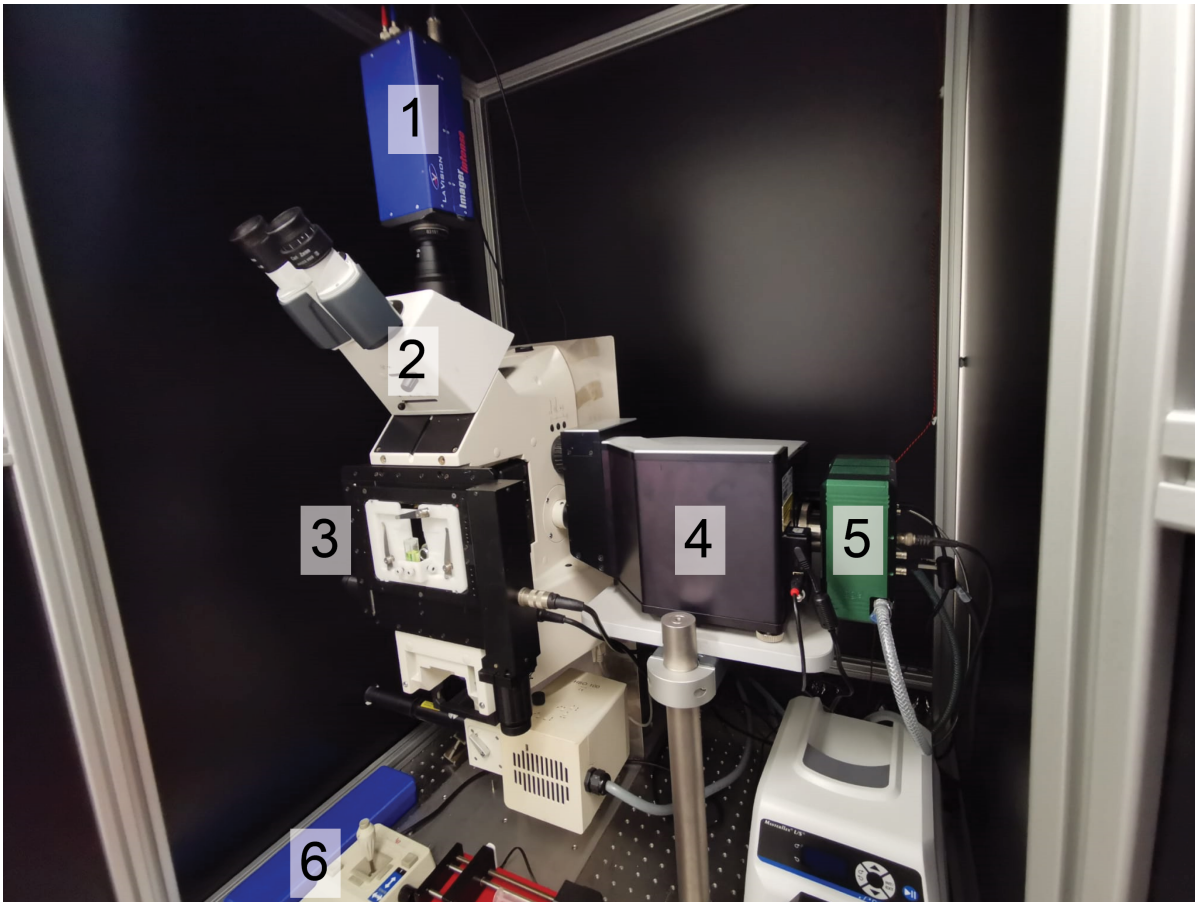

Figure 3.2: Picture of the laser set-up inside the black box to perform FLIM measurements. 1. PIV camera (not used for FLIM, 2. Microscope, 3. Flow cell holder and the traverse plate, 4. Spinning disc, light filters and entry of the laser, 5. Toggel FLIM camera, and 6. Joystick to operate the traverse plate on which the sample holder is placed.

Camera: FLIM Toggel camera by Lambert Instruments. The camera has a resolution of 512 x 470 pixels.

Filters: Multiple filters are used. A clean-up filter is used to filter out any higher wavelength light coming from the laser. The fluorescent light coming back from the sample will be reflected using a dichroic mirror which only reflects the light of a certain wavelength to already filter out more. Before the camera there is one more filter. This is the emission filter which is a long-pass filter with a cutoff at $420\,$nm. This filters out most light from other fluorophores in the sample.

Spinning disk: A spinning disk is a disk with small holes. It is used to record only light that is in the focus plane.

Laser: A modulated diode laser with a wavelength of $405\,$nm is used. The modulation frequency of the laser is set at $20\,$MHz.

Microscope: The 5x objective is used. In combination with the resolution of the camera this means $1\text{pixel} = 4.76\,\mu\text{m}$.

Software: The image processing software LIFA by Lambert Instruments.

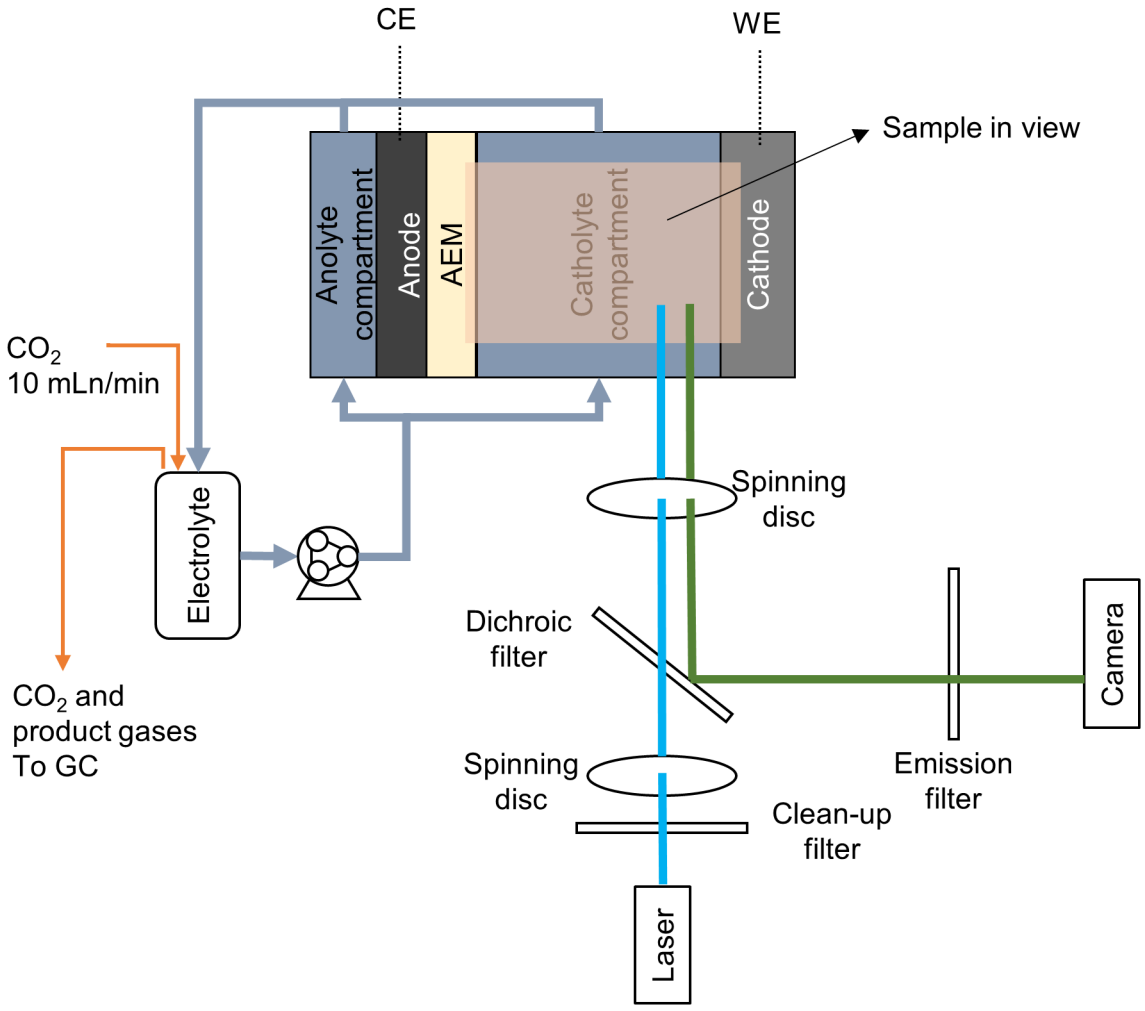

Figure 3.3: A schematic of the experimental set-up with FLIM. The grey lines indicate the liquid flow, the orange lines indicate the gas flow, and the blue and green lines show the light path.

Fluorescent dye The dye used in this project is the so-called alpha dye. The dye was published by Jager, Hammink, Berg, *et al.* to be a useful as an on-off fluorescent pH sensor Jager, Hammink, Berg, *et al.* It is a quinolinium dye (7-amino-1-methylquinolinium) and has a $(CH_2)_3 - NH_2$ tail. The chemical structure of the dye can be seen in Figure 3.4. It was thought that this specific tail gives an interesting fluorescence lifetime-pH gradient for the more alkaline pH-range we want to research.

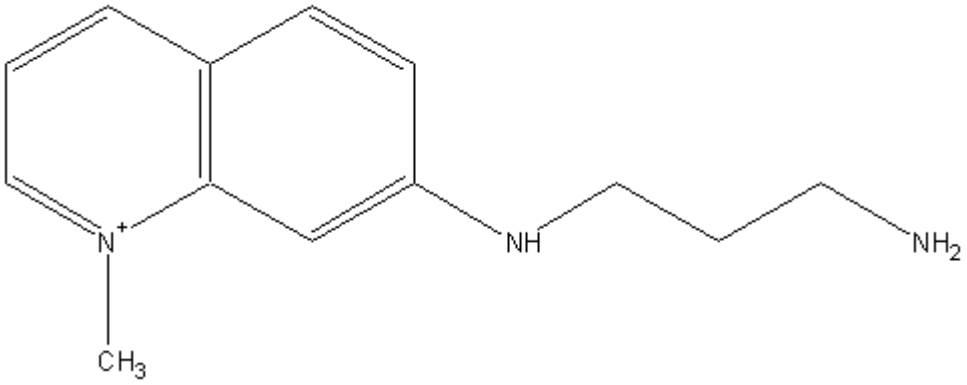

Figure 3.4: The chemical structure of the alpha dye used. It is a 7-amino-1-methylquinolinium with a $(CH_2)_3 - NH_2$ tail.

Calibration To obtain a curve for the fluorescence lifetime-pH conversion two calibrations series were performed. Both were performed with phosphate buffers. The first one was done in a cuvette and the other one in the electrochemical cell as used in this project.

From tests was obtained that is important to keep all settings the same for each of the experiments. Therefore all the FLIM results are obtained using the following settings: alpha dye concentration of $100\,\mu mol\,L^{-1}$, exposure time between 34 to 100 ms, laser power 300 mW, 5x objective is used, 8 number of phases, 20 MHz and the fluorescence lifetime that is being recorded is the phase-shift lifetime (τ_ϕ).

3.2.2. Experimental set-up for FLIM

In Figure 3.3 the electrochemical cell inside the experimental setup with FLIM is shown. In the figure the grey lines indicate the liquid flow through the cell. The orange lines indicate the gas flow through the electrolyte bottle to keep the saturation of the electrolyte.

To be able to record the same positions inside the cell three positions were marked on the outside of the cell. These three positions are indicated with numbered and colored boxes in Figure 3.5. With these three position we could see the pH profile at the beginning, middle and end of the cathode.
One of the limitations of FLIM in this setup is the reproducibility of the positioning of the microscope with regard to the cell. A method was found to do this as good as possible. This method is explained in Figure 3.6. The method uses movements in x, y and z directions, even though the z-y stage cannot be precisely controlled electronically.

Three markings were made on the outside of the catholyte gap to perform the method. These markings indicate three positions inside the cell where the membrane and the cathode are in contact with the electrolyte. A schematic of this is given in Figure 3.6 **a**. In **a** the black lines inside the figure correspond to drawn on black lines on the catholyte channel part. These black lines are visible via the microscope when the outer wall of the catholyte channel is in focus. The three light colored boxes indicate the sample that was viewed.

The method of finding these three positions is described graphically in Figure 3.6 **b**. The catholyte channel part is put in line with the microscope objective using the traverse plate on which the sample holder and electrochemical cell are secured. This is done by moving it in the y- or z-direction. Then the outer wall of the catholyte channel part is placed in focus of the microscope. This is done using the focusing of the microscope itself by moving it in x-direction. On this outer wall the three markings

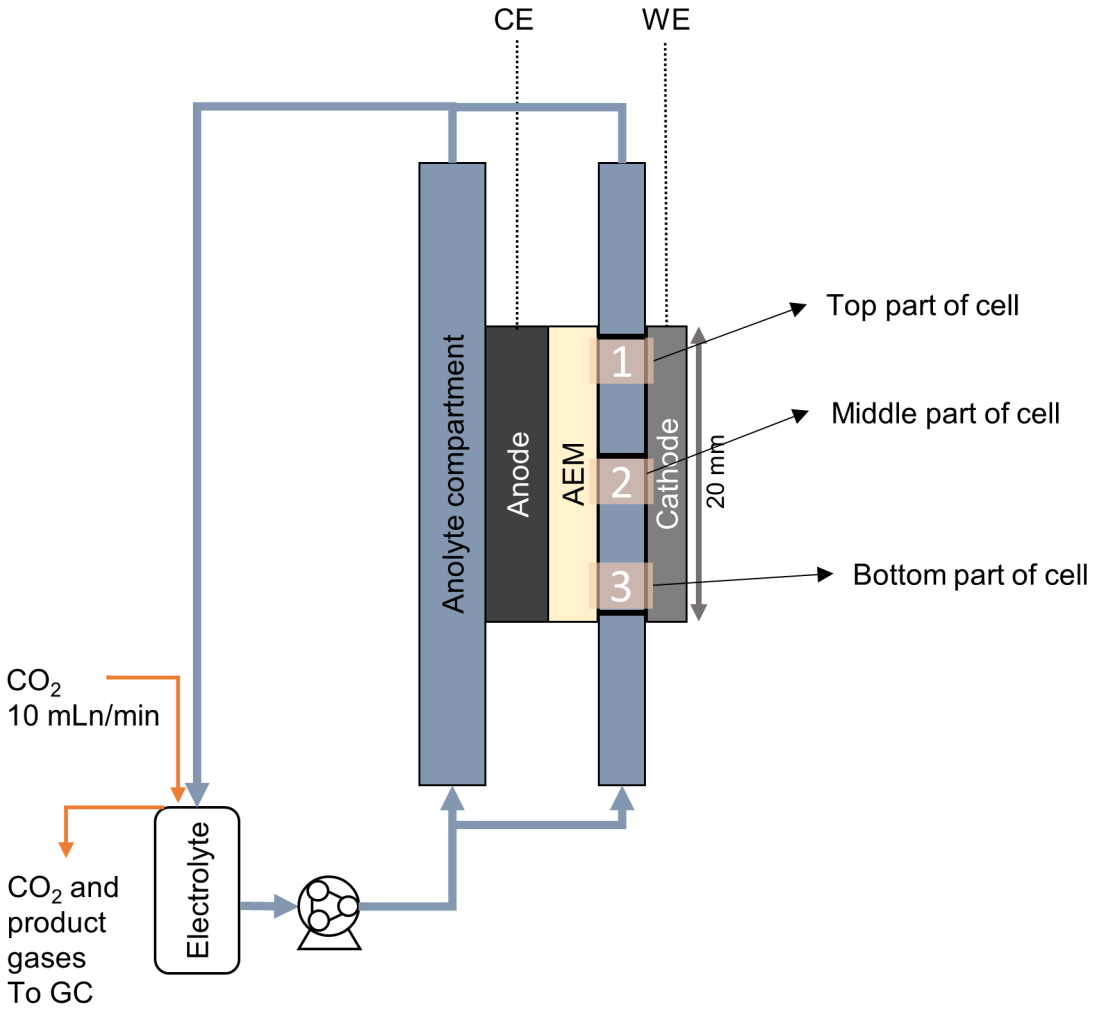

Figure 3.5: The three positions that are imaged inside the cell with FLIM.

can be found. Such a marker is found by moving the sample holder in z-direction (up or downwards). When such a marker is found the sample view is slightly adjusted to be just below or above the marker (as the sample views are indicated in Figure 3.6 **a**). Using DAVIS (automated zooming program) the microscope objective is moved 5 to 6 mm in x-direction. The plane in focus now lies between the first and second wall of the catholyte channel.

After the 30 min stabilization time with the applied the current density at least three images were obtained for each of the positions. The with FLIM obtained images were processed with MATLAB. In this way we were able to convert the images into fluorescence lifetime images and profiles. With the use of the calibration curve we could convert the fluorescence lifetime into pH to obtain pH images and profiles.

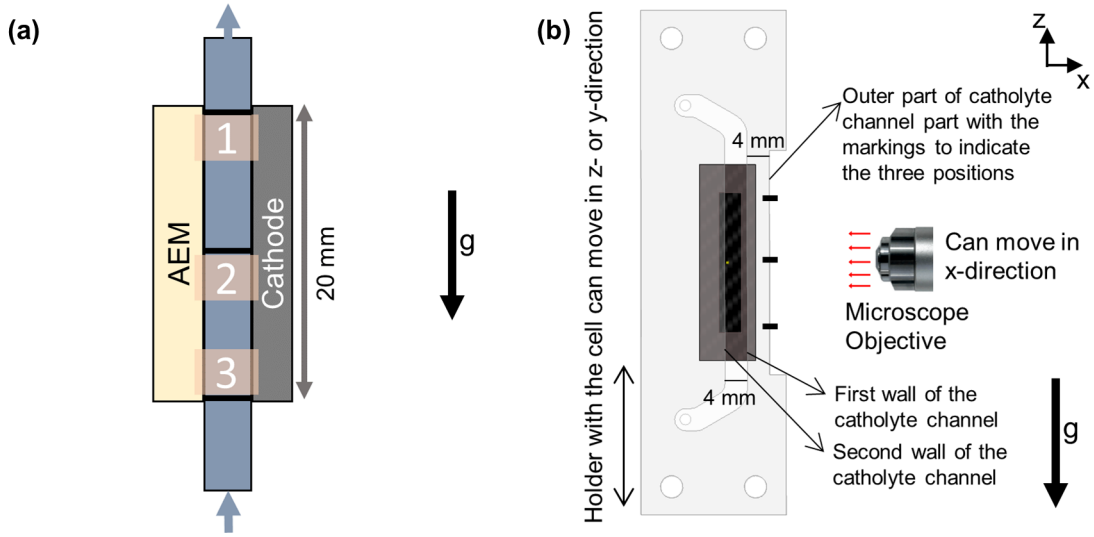

Figure 3.6: On the outside of the cell three positions for the FLIM measurements are indicated. With the use of these markings, the traverse plate and Davis (an automated zooming program) it is possible to move from positions to position and to be between 1 to 2 mm inside the electrolyte channel. **a:** The three positions inside the cell are indicated with their number and a light colored box inside the figure. These positions are marked with black marker on the outside of the catholyte channel as indicated by the black lines in the figure. All three positions are within the part of the electrolyte that is contact with the active part of the cathode and the membrane (AEM) both with a length of 20 mm. The black arrow with g indicated the gravity. The electrolyte is flowing in opposite direction of the gravity as shown by the blue arrows. Position **1** is at the end of the active part of the cathode, **2** is in the middle of the active part and **3** is at the beginning of the active part of the cathode. **b** shows a graphical explanation of how the three positions inside the cell can be found. Firstly, the catholyte channel part is put in line with the microscope objective using the traverse plate on which the sample holder is placed by moving it in y- or z-direction. Then the outer plane of the catholyte channel part is put in focus using the focusing of the microscope (in x-direction). On this plane the three markings are visible. Such a marker is then found by moving the sample holder upwards or downwards (in z-direction). When such a marker is found the sample in view is slightly below the marker (or in case of position 3 above the marker). Using Davis the microscope objective is then moved 5 to 6 mm in x-direction. This means that the plane in focus now lies between the first and second wall of the catholyte channel. The recorded images are flipped vertically by $180°$. The bottom of the FLIM images corresponds to location higher up in the flow channel.

4

Results and Discussion

This chapter will present and discuss the results regarding the use of Fluorescence Lifetime Imaging Microscopy (FLIM) and the effects of the different parameters – namely anion type and concentration of the electrolyte, the liquid flowrate and the applied current density – on the pH profile and the cell potential. First the results to validate the used technique for local pH measurements FLIM are given. This is followed by a presentation of the effect of the anion type and concentration of the electrolyte. Next, the results showing the effect of different current densities are presented. And finally, the Reynolds number and thus the liquid flow rate of the electrolyte affecting the local pH and the cell potential are shown and discussed.

4.1. Validation of Fluorescence Lifetime Imaging Microscopy in an electrochemical cell

This section presents the results to validate the Fluorescence Lifetime Imaging Microscopy (FLIM) method in an electrochemical cell. To validate this method first two calibration curves of the alpha dye are presented. Next, the obtained fluorescence lifetime images and profiles are presented and we discuss how these can be read. This is followed by a comparison of the three types of electrolytes and their measured pH to the calibration curve obtained inside the electrochemical cell. Finally, the effect of different types of bubbles on the fluorescence lifetime images is discussed. Using these results we can discuss the pH accuracy and spatial resolution as well as other implications of FLIM.

4.1.1. Calibration of the alpha dye

Two calibrations were performed to determine the fluorescence lifetime-pH gradient of the alpha dye used to perform FLIM measurements. Both fluorescence lifetime-pH calibration curves are presented in Figure 4.1. The fluorescence lifetime (τ) in ns is shown over the pH. The blue curve shows the modulation fluorescence lifetime (τ_M) for the different pH samples in a cuvette performed by Aron Kahn. The red curve displays the phase-shift fluorescence lifetime (τ_ϕ) measurements for the pH samples inside the electrochemical cell used. This electrochemical flow cell was used during this project. The pH samples used to perform the calibration measurements are $0.4\,\mathrm{mol\,L^{-1}}$ phosphate buffers with a $100\,\mu\mathrm{mol\,L^{-1}}$ alpha dye concentration.

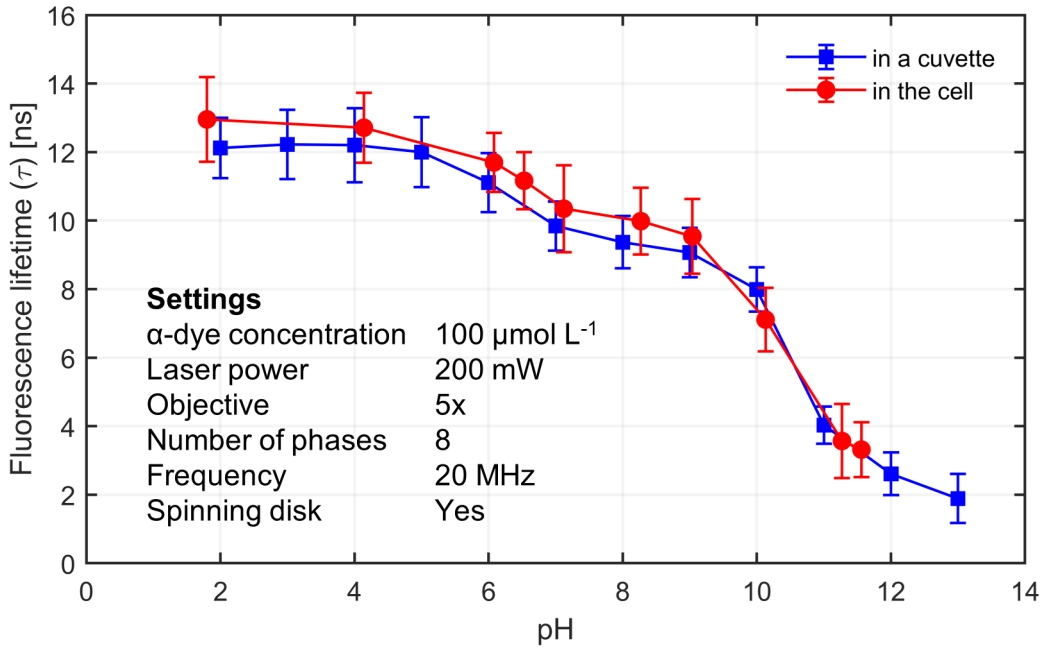

Figure 4.1: The fluorescence lifetime-pH calibration curves of the alpha dye obtained inside a cuvette as well as inside the electrochemical cell used in this project. Both calibration curves follow a similar trend with a clear relation between fluorescence lifetime (τ) and pH above pH 9. For the calibration curve inside a cuvette the modulation lifetime (τ_M) is shown and for the curve inside the electrochemical cell the phase-shift lifetime (τ_ϕ) is shown. The exposure time is different in both settings. The range used in the cuvette calibration is between 100 and 200 ms and for the flow cell the range is between 34 and 100 ms. The light source was a diode laser with a wavelength of 405 nm operating at a modulation frequency of 20 MHz and a power of 200 mW of the maximum capacity of 300 mW. The pH samples used are phosphate buffers with a 100 µmol L^{-1} alpha dye concentration. The 5x objective is used on the microscope in combination with the spinning disk.

Two major observations can be made from Figure 4.1. The first observation is the trend visible in the calibration curves. The second observation is the differences and similarities between the two curves.

Both calibration curves inside the cuvette and inside the electrochemical cell follow a similar trend. A clear relation is visible for pH higher than pH 9 in both the flow cell and the cuvette calibration. Also similar for the two calibrations is that the trend before pH 9 is less distinct. From Figure 4.1 can be stated that when the fluorescence liftetime is above 10 ns the pH is lower than pH 7.

The more distinct trend in the calibration curve at higher pH is due to the specific pKa of the used alpha dye. This pKa is a result of the $(CH_2)_3$ – NH_3 tail that is present in the dye molecule. Its chemical structure is shown in Figure 3.4. If a different fluorescence lifetime-pH gradient needs to be investigated a different tail can be added to the quinolinium dye. This will then change the pKa and thus the pH of deprotonation.

The two calibration curves both show differences and similarities which can be correlated to the measurement settings used to perform the calibrations. For both curves can be seen that they follow a similar trend. However, there is a slight vertical shift between the two. This vertical shift is mainly visible above a lifetime of 8 ns. However, the two curves lie within each others error bars. The error in these measurements is calculated from the noise in the fluorescence lifetime image obtained and we assume that the mean value is rather accurate since it is obtained from a large number of pixels. Therefore, we do consider this shift between the two to be significant to be discussed. The difference between the two curves can be due to differences in the optical parameters (e.g. dye container material, camera exposure times, fluorescent lifetime type).

An important difference between the two calibration is the reservoir in which the measurements are performed. This was important to be researched to determine if the reservoir has an effect on the trend of the curve. There are two differences between the electrochemical cell and the cuvettes. For the

electrochemical cell the PMMA wall in front of the liquid we want to study is thicker (4 mm) than the PS wall of the cuvette (1 mm). This thicker wall does not show to influence the range of the fluorescence lifetime-pH trend of the alpha dye. There is also a difference in the material of the reservoir. The flow channel material is PMMA (polymethyl methacrylate) and the cuvette material is PS (polystyrene). The different material can have an effect on the measured fluorescence lifetime. However, from the two calibration curves this effect could not clearly be desribed or concluded.

The measurements of the two curves had more differences. Firstly, for the samples inside the cuvette the modulation lifetime was measured and for the samples in the electrochemical cell the phase-shift lifetime was measured. Secondly, the range within the exposure time was set was also different for both curves. The range used in the cuvette calibration curve is between 100 to 200 ms and for the flow cell the range is between 34 to 100 ms.

A vertical shift can be caused by the type of fluorescence lifetime displayed: modulation depth lifetime (τ_M) is being used instead of the phase shift lifetime (τ_ϕ) for the calibration inside the cuvette. There can be a difference in the lifetimes calculated from either the phase shift or the change in the modulation depth [57]. The two calculated lifetimes can differ if the emission is due to multiple exponential decay processes. It is stated in literature that in this case τ_ϕ will be lower than τ_M. When comparing the value of τ_ϕ and τ_M of an individual measurement τ_ϕ is indeed lower than τ_M. However, when comparing the two curves to each other the calibration performed in the cell shown in τ_ϕ has a overall higher lifetime than the calibration done in a cuvette measured in τ_M. Therefore we cannot relate this vertical shift to the display of the type of fluorescence lifetime.

The other different setting of the two calibrations curves is the range in the exposure time. A study was done by Jorrit Bleeker and Aron Kahn to obtain insights in the effect of this setting. A lower exposure time leads to a higher τ_M; however, it does not lead to a change in τ_ϕ. The phase-shift lifetime (τ_ϕ) on the other hand is affected by using a different laser power. Any of these correlations could not be linked to the slight shift between the two calibration curves.

From the two observations and their possible explanations the following limitations and implications can be obtained. The calibration curve obtained from the measurements inside the cell show a clear trend for pH above 9 and therefore the alpha dye can be used to show a significant increase in pH inside a sample nicely. It will be more difficult to quantitatively say something about the samples with a lifetime above 10 ns. Above 10 ns the curve is similar to a plateau. In this region a change in τ cannot clearly be linked to a certain pH other than a pH of 7 or lower.

The different settings of the two calibrations could not explain the slight vertical shift between the two curves. Therefore it is important to keep the settings the same during measurements and when comparing measurements. All the FLIM results are obtained using the following settings:

- alpha dye concentration of 100 µmol L^{-1},
- exposure time between 34 to 100 ms,
- laser power 300 mW,
- 5x objective,
- 8 number of phases,
- 20 MHz as modulation frequency,
- recording the phase-shift lifetime (τ_ϕ).

For the FLIM images and pH profiles obtained in this thesis the τ_ϕ was used, because the phase shift lifetime is more sensitive to the faster decaying species (shorter lifetimes) and the modulation depth lifetime is more sensitive to the slower decaying species (longer lifetimes) [57].

We suggest a more elaborate study to be performed into the effect of the settings of the FLIM method. We also recommend to perform a calibration when a new reservoir (different electrochemical cell) is used.

4.1.2. Obtaining fluorescence lifetime images and profiles

Figure 4.2 displays three figures of a flowing 1 M $KHCO_3$ electrolyte fully saturated with CO_2. The different figures give insights into the image that is obtained through FLIM, how the image can be read and how it is transferred into a phase-shift fluorescence lifetime (τ_ϕ) profile.

The FLIM camera records 2D images for which the fluorescence lifetime is determined for each pixel. Figure 4.2 **a** shows how this 2D image can be seen within the electrochemical cell. The flow direction, the estimated location of the AEM and the cathode are indicated inside the image. The black arrow indicates the gravity being in opposite direction of the electrolyte flow.

Figure 4.2 **b** shows the same image of the electrolyte without these indications. The color profile shows the phase-shift lifetime (τ_ϕ) ranging from 0 to 14 ns. The height and width are scaled according to ratio pixels to mm ($4.76\,\mu m = 1$ pixel with the 5x objective).

From the 2D image the mean of the phase-shift lifetime in ns is taken over the width of the FLIM image frame. To obtain this average the mean is taken for the pixels from 100 to 400 over the height of the image as indicated by the black box in **b**. In Figure 4.2 **c** the fluorescence lifetime profile is shown over the channel width (mm).

From Figure 4.2 observations can be made which will have implications on how we further interpret the sample measurements. As can be seen in Figure 4.2 **b** and **c** the location of the cathode and membrane cannot be as easily indicated as those were illustrated in **a**. The illustrations of these components are an estimation of where we expect them to be. In general we can make some estimations to get a clue of the location. For the fluorescence lifetime profile much irregularities can be seen at the sides of the frame width. The noise on both sides of the width of the image is due to a lower intensity of the incoming light. This lower intensity can be because of the absence of dye molecules or no emission at all because it is a non reflective surface.

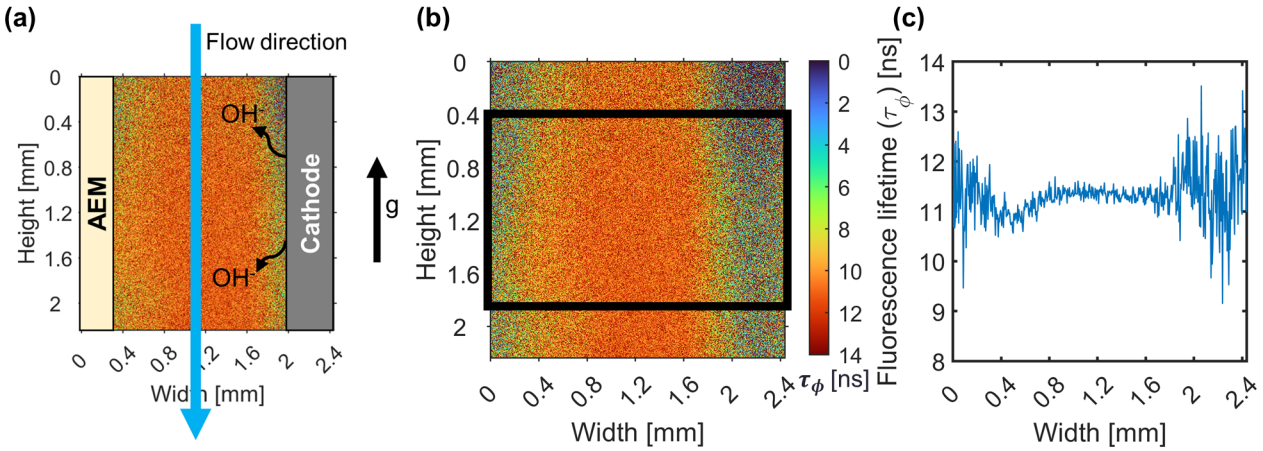

Figure 4.2: An example of a FLIM measurement to show where the cathode and membrane are located inside the FLIM image and to show a fluorescence lifetime profile over the width of the image. The fluorescence lifetime used is the phase-shift lifetime (τ_ϕ). **a** displays a FLIM image with indications of where the cathode and membrane are located and an indication of the direction of the electrolyte flow. The arrow with g indicates the gravity playing in opposite direction of the electrolyte flow. **b** gives the same FLIM image without the indications but with the legend indicating what color corresponds to what value of τ_ϕ in ns. The height and width of the image are scaled according to the ratio $4.76\,\mu m = 1$ pixel with the 5 times objective. **c** shows the fluorescence lifetime (τ_ϕ) profile over the width of the channel. This profile is obtained by averaging the fluorescence lifetime over the height of the image also indicated in **b** by the black box. This is from pixels 100 to 400 pixels with the total pixels being ± 500. Figures **b** and **c** will be used in this thesis to display the lifetime in an image and as a profile for the different measurements. Both can also be converted to a pH image and pH profile using the fluorescence lifetime-pH calibration curve.

These parts of the lifetime profile where the irregularities are located can be extracted from the image. However, it is important to notice that the width of the channel is 2 mm. The channel width sometimes appears to be less than 2 mm in the image. For the 1 M $KHCO_3$ electrolyte the noise on either side can make us extract up to 0.4 mm at the left and from 1.8 mm onwards on the right side. This leads to the width of the channel being 1.4 mm according to this method. This width is smaller than the actual width of the channel. A reason for this apparent channel width being smaller than 2 mm can be that the cell is looked at from a slight angle.

In subsection 3.2.2 the method to create better reproducibility of the positioning of the microscope with regard to the cell was described. This method however still has some restrictions. When the cell is placed lop-sided into the sample holder changing between positions can result into the wall not being present at the same position each time. When moving from one positions to another the cell could

be slightly tilted therefore it would be necessary to also move the cell slightly in a positive or negative sideways (y-)direction. Looking at an angle at the sample is also not resolved using this method.

Because of these issues with positioning the microscope reproducible the edge of the channel can not always be found in the same position in the image. Also the cell can be looked at from a slight angle. This results in the seen width of the channel not being similar to the actual width of the channel. Therefore, the sides are not retracted from the images. The noise in the signal due to the lower intensity is helpful in determining where the cathode starts. The known width of 2 mm also helps to determine what parts can be subtracted from the image.

4.1.3. Fluorescence lifetime measurements for the different electrolytes and the translation to pH images and pH profiles

Before the start of the electrochemical measurements we took a FLIM image of each type of electrolyte. In this case the electrolyte was fully saturated with CO_2 and continuously purged with CO_2 and pumped around. The FLIM image was taken to obtain insight in the fluorescence lifetime of the bulk electrolyte before any current is applied.

The three electrolytes are displayed in Figure 4.3. The top row of the figure (**a**, **b** and **c**) show the phase-shift fluorescence lifetime (τ_ϕ) image ranging from 0 to 14 ns. In these images the AEM is located on the left side and the cathode on the right side of the image. The electrolyte is flowing from top to bottom of the image (against the gravity in the set up). In general a higher fluorescence lifetime (so more red as displayed in the color bar) relates to a lower pH.

The bottom three figures (**d**, **e** and **f**) show the profile of the fluorescence lifetime over the width of the catholyte channel. These profiles are taken from the FLIM images by averaging τ_ϕ over the height of the image. This is indicated by the black box in **a**. In these three fluorescence lifetime profile figures the overall average phase-shift fluorescence lifetime is also displayed.

The information from Figure 4.3 is combined with the pH measurement done with a pH-meter. These pH measurements were performed on the fully saturated electrolytes. An overview of this is given in the table within Figure 4.4. The measurements are also shown within the graph as indicated by the three separate data points.

The bulk measurements are shown together with the fluorescence lifetime-pH calibration curve of the alpha dye as performed inside the electrochemical cell. This is given in Figure 4.4. This is done to show the three measurement with respect to the calibration curve. The bulk pH and fluorescence lifetime of K_2SO_4 fall nicely into the flow cell calibration curve.

The two data points of the $KHCO_3$ both are above the flow cell calibration. The two data points fall slightly outside the errorbars of the calibration curve. However, both do correspond in general to lower/neutral pH and lifetime as was determined from the calibration curve earlier. With this is meant that for the $KHCO_3$ electrolyte with lower pH (0.1 M $KHCO_3$) has a higher lifetime compared to the one with higher pH (1 M $KHCO_3$).

The ion type or ion concentration could have an effect on the fluorescence lifetime. This can be the reason the two $KHCO_3$ measurements lie above of the calibration curve. In this thesis the fluorescence lifetime is studied to gain insights in the pH. However, other characteristics can also have an effect on the fluorescence lifetime.

Within the research group research was done to obtain insights into the effect of different salts on the lifetime. This research was done by LO2 students under supervision of Aron Kahn. These students tested the following electrolytes: Na_2SO_4, K_2SO_4, KCl, $KHCO_3$ and K_2CO_3. In this way they hoped to distinguish the effect of the cations (Na^+ and K^+) and of the anions (SO_4^{2-}, Cl^-, HCO_3^- and CO_3^{2-}). They also studied the salt concentration beside the ion type. From this research was concluded that the salt concentration can have effect on the lifetime; however, no clear trend was observed. Especially the effect of $KHCO_3$ was not studied sufficiently to tell if the lifetime is affected with the presence of HCO_3^- anions.

In other research FLIM is also used to obtain the concentration of a salt in a local environment. Often quenching of the fluorescence as a result of a certain ion type is used to study concentrations. Cl^- and Ca^{2+} can result in quenching of fluorescence of certain dyes [58]. A Cl^-- sensitive dye can be used to study the accumulation of chloride in neurons with the use of FLIM [59].

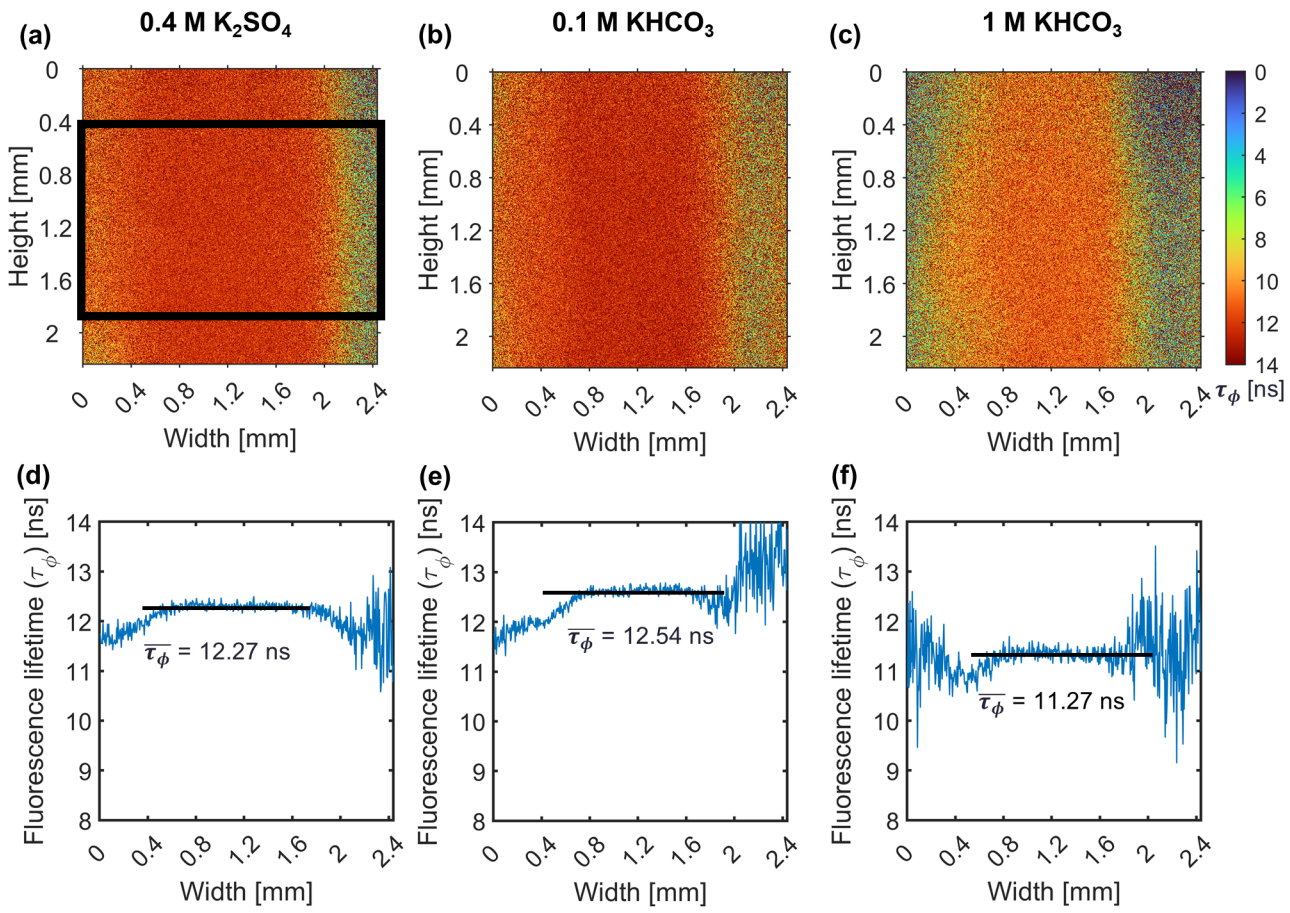

Figure 4.3: The phase-shift fluorescence lifetime (τ_ϕ) image, profile and average per electrolyte type (0.1 M $KHCO_3$, 1 M $KHCO_3$, 0.4 M K_2SO_4) are displayed for the case where the electrolytes are fully saturated with CO_2 before any current is applied. Figures **(a)**, **(b)** and **(c)** display the fluorescence lifetime over the height and width of the frame of the FLIM image obtained inside the catholyte channel. The cathode is located at the right side and the AEM at the left side of the image. The electrolyte flows from top to bottom in the image. For figures **(d)**, **(e)** and **(f)** the fluorescence lifetime is averaged over the middle part of the height of the FLIM image as indicated by the black box in figure **(a)** and shown over the width of the frame. The average values for $\overline{\tau_\phi}$ are calculated taking the mean over the pixels 100 to 400 in both width and height. The height and width of the image are scaled according to the ratio $4.76\,\mu m = 1$ pixel with the 5 times objective. The light source was a diode laser with a wavelength of $405\,nm$ operating at a modulation frequency of $20\,MHz$. The measurements are performed at the maximum power of the laser, $300\,mW$.

The alpha dye its fluorescence lifetime behavior can be affected by the carbonate or hydrogen carbonate concentration. For now, can be stated that not enough research has been done to show or explain the effect of HCO_3^- anions on the lifetime of the alpha dye. The effect of $KHCO_3$ should be further researched. A calibration needs to be carried out with a $KHCO_3/K_2CO_3$ buffer series to obtain a correction of the error in the difference from the initial calibration curve.

In Figure 4.5 the two curves are given for the two types of electrolyte as used for conversion of fluorescence lifetime to pH in the rest of this thesis. When using the calibration curve as displayed in Figure 4.4 to calculate the pH for the $KHCO_3$ electrolytes the higher lifetime will result in lower pH values than the pH values measured before and after an experiment. Therefore a different calibration curve is suggested and displayed in Figure 4.5 **a** and used for the lifetime-pH calibration for the samples with $KHCO_3$ electrolyte. In this calibration the two bulk measurements for $KHCO_3$ are added to the calibration cruve performed in the electrochemical cell. This curve is shown in red in both Figure 4.1 and Figure 4.4. The two measurement of the bulk for $KHCO_3$ replace the data points of the curve above $10\,ns$. This adjust the calibration curve and caps of the lifetime to pH at pH 6.6. We assume that there is no acidification that is of interest.

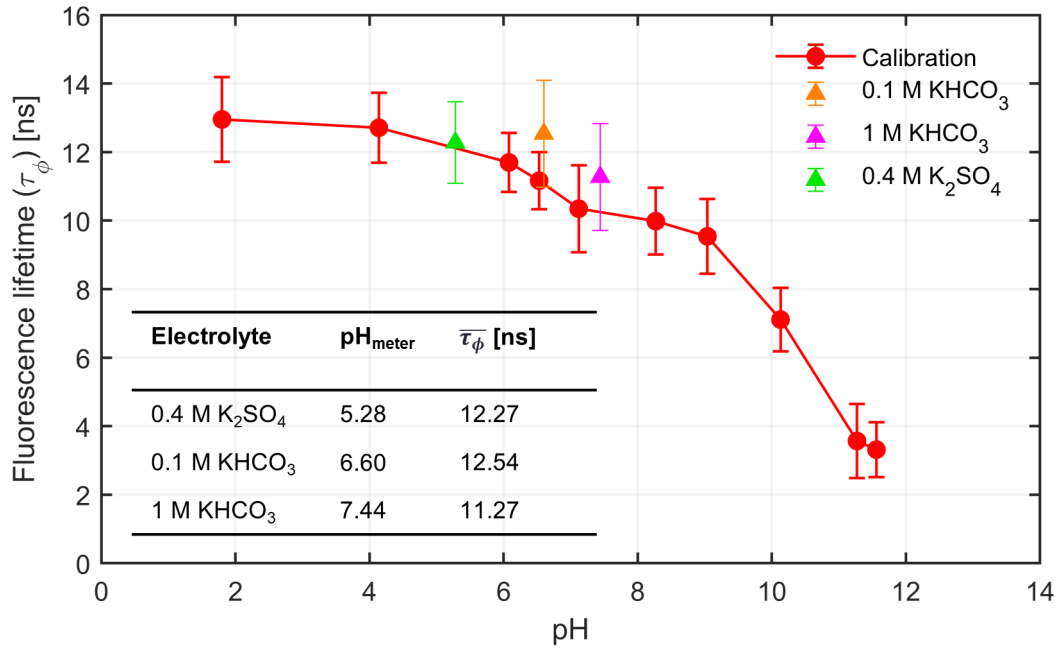

Figure 4.4: The bulk measurements for the three electrolytes displayed in the fluorescence lifetime-pH calibration curve of the alpha dye as performed inside the electrochemical cell. For all measurements (bulk and calibration) the phase-shift lifetime (τ_ϕ) is given over the pH. The table gives bulk measurements as they are displayed inside the graph. The pH was measured when the electrolyte was fully saturated with CO_2 and before any current was applied. The average fluorescence lifetime ($\overline{\tau_\phi}$) was obtained from the FLIM images as shown in Figure 4.3.

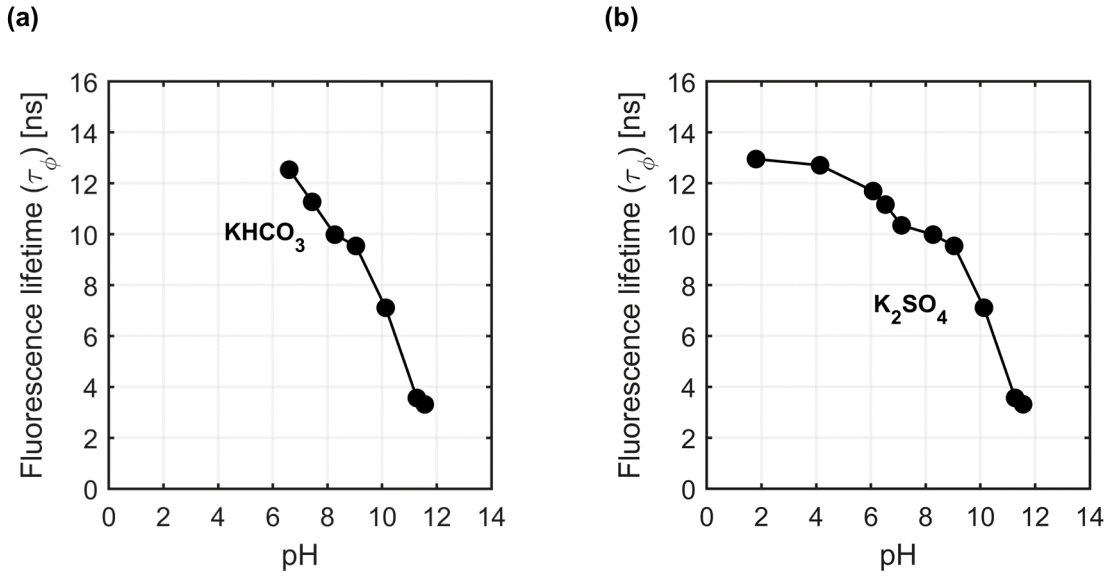

Figure 4.5: The fluorescence lifetime-pH calibration curves of the alpha dye as determined for $KHCO_3$ **(a)** and K_2SO_4 **(b)** samples. These curves are used for conversion of fluorescence lifetime to pH for the electrolytes respectively.

The fluorescence lifetime-pH calibration for the K_2SO_4 electrolyte Figure 4.5 **b** should give reliable results in pH range from 5 to 11.5 as measured with the calibrations in the electrochemical cell. Therefore for this electrolyte the calibration curve inside the electrochemical cell is used. This is the same curve

as shown in red in Figure 4.1 and by the solid red line in Figure 4.4.

4.1.4. Effect of bubble formation

In the electrochemical cell gas bubbles can occur. This happens because of the production of CO and H_2 which both have a lower solubility than CO_2 in aqueous liquids. These bubbles have some effects on the obtained FLIM images. Mainly three types of bubbles were observed when performing the FLIM measurements. These three types are shown and indicated in Figure 4.6.

The first type is a large bubble (Figure 4.6 **a**). Larger bubbles grow on the electrode surface and can grow to be roughly the size of the channel. These bubbles were easily observed in the intensity images. These bubbles could lead to the channel being blocked. This then lead to low intensity as can be seen in **a**. Because of this low intensity it was more difficult to obtain an accurate FLIM image. The lower intensity resulted in a higher variance in the observed fluorescence lifetime. This is indicated in **d**.

The second type are the bubbles growing at the electrode surface (Figure 4.6 **b** and **c**). These develop to be the large bubbles as shown in **a**. These bubbles were also easily observed in the intensity images and similar to large bubbles resulted in a higher variance in fluorescence lifetime as can be seen in **e** and **f**. In some cases the presence of a growing bubble lead to an increased lifetime behind a growing bubble as indicated by the box in **f**.

Very small bubbles (around 0.1 mm) are the third type of bubble inside the electrochemical cell. These could only be observed when looking at the intensity images Figure 4.6 **b**. When a FLIM measurement was done the actual bubbles were no longer visible. Sometimes some artefacts because of a large stream of smaller bubbles could be seen. This showed up as streaky lines over the height of the image. The box with arrow in **e** shows the location of the moving bubbles. These are no longer clearly visible in the image.

Different types of bubbles were dealt with different. When a large bubble that was blocking the electrolyte channel was in the view of the microscope the following was done: a slightly different position inside the cell was chosen to obtain an image free of large bubbles to ensure the fluorescence lifetime was not affected majorly. The smaller bubbles as well as growing bubbles were more difficult to avoid and therefore were accepted inside the FLIM frame.

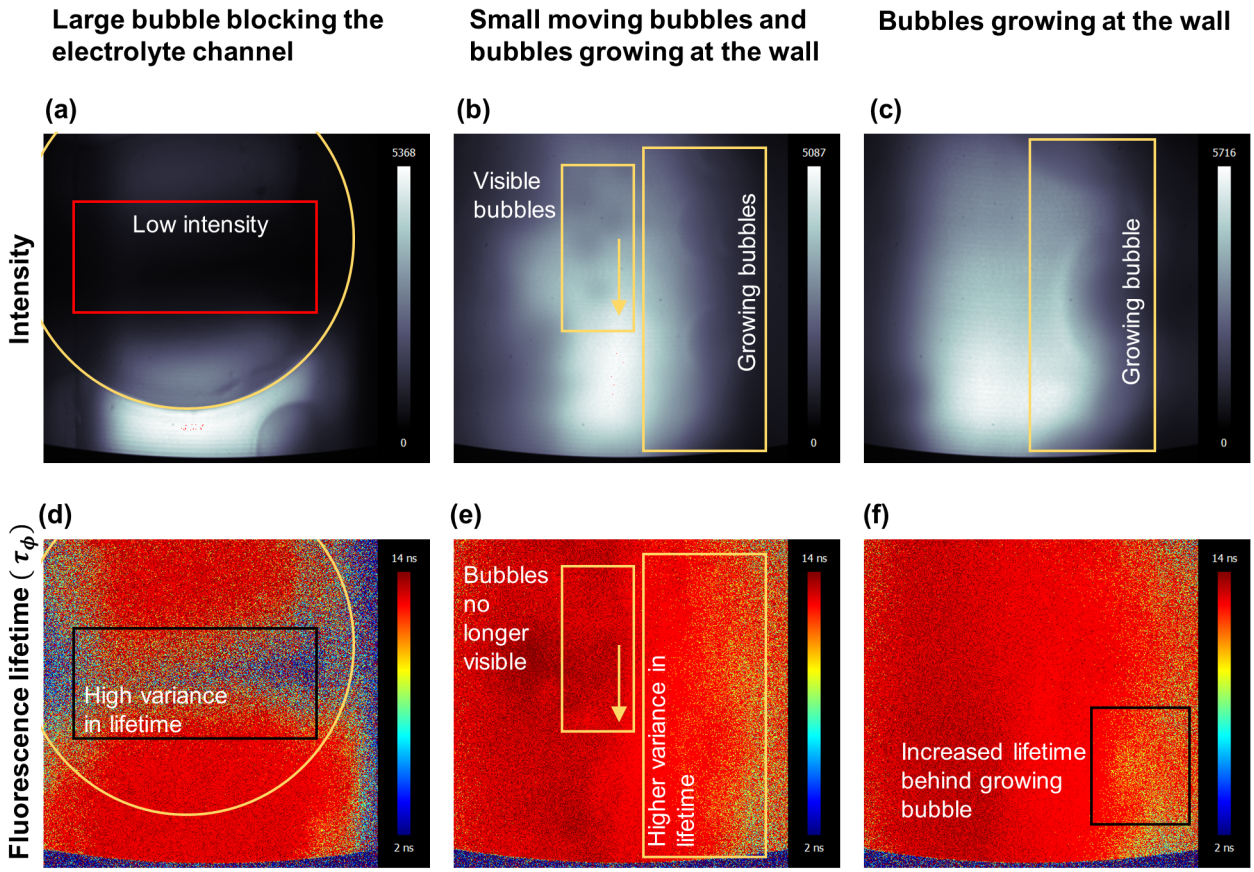

Figure 4.6: Different types of bubbles shown in intensity images and the effect of said bubbles onto the fluorescence lifetime images taken. Three types of bubbles can be distinguished. In **a** and **d** a large bubble indicated by the yellow circle can be seen. The bubble is blocking the entire electrolyte channel. In the middle part of the bubble the intensity is very low (**a**). This leads to a high variance in fluorescence lifetime (**d**). On the outer parts of the bubble the lifetime does not seem to be affected. In **b** and **e** two types of bubbles can be detected. In the yellow box with the arrow small moving bubbles are indicated. They result in a slight variance in the lifetime. The other yellow box indicated bubbles growing at the wall. This type of bubbles is also found in **c**. Both **e** and **f** show a higher variance in fluorescence lifetime near the wall where the bubbles are growing. This is also indicated by the black box in **f**.

4.2. Effect of electrolyte concentration and anion type

Experiments were done with three different electrolytes. The electrolytes used are: 0.4 M K_2SO_4, 0.1 M $KHCO_3$ and 1 M $KHCO_3$. These electrolytes differ in concentration and in anion type. These two result in a difference in buffer capacity and in conductivity. The buffer capacity shows to have an effect on the pH change near the electrode. Together with the conductivity it can have an effect on the potential as a current density is applied to the cell.

4.2.1. Effect of buffer capacity

The buffer capacity is calculated per electrolyte and an overview is given in Table 4.1. The K_a is converted from the acid dissociation constant (pKa) as given in Table 4.1 [37]. To calculate the buffer capacity the concentration of H^+ is calculated from the pH as measured with the pH-meter.

Table 4.1: Buffer capacities for the three electrolytes together with the conjugate acid and base pair, the measured pH and the acid dissociation constant pKa [37].

Electrolyte	HA	A^-	pH_{meter}	pKa	β
0.4 M K_2SO_4	HSO_4^-	SO_4^{2-}	5.3	1.9	4.6×10^{-4} mol L^{-1}
0.1 M $KHCO_3$	H_2CO_3	HCO_3^-	6.6	6.4	7.5×10^{-2} mol L^{-1}
1 M $KHCO_3$	H_2CO_3	HCO_3^-	7.4	6.4	1.8×10^{-1} mol L^{-1}

Beside the more common buffer capacity we also decided to look at the concentration of bicarbonate. This ion is an important player in the buffering reactions inside the electrolyte as they were given in subsection 2.2.2. In general the decision for a $KHCO_3$ electrolyte is also often based on the buffering effect and the reduction of CO_2 consumption because of the presence of HCO_3^-.

An overview of the concentrations of the different ions in the electrolytes is given in Table 4.2. All three of the electrolytes are fully saturated with CO_2. The concentration of CO_2 is equal to the concentration at $T = 292.15$ K and a partial pressure of CO_2 $P_{CO_2} = 101\,325$ Pa. These calculations are described more in depth in section B.1. To calculate the concentration of CO_2 the salting out effect was not taken into account. The other ion concentrations were calculated using the buffering reactions as described in subsection 2.2.2 and using the reaction rate constants as provided in Table 2.1 [42]. A description of these calculations is given in section B.2.

We also did calculations for the concentrations taking into account the salting out effect. The results of these are given in section B.3. The concentration of CO_2 stayed in the same order of magnitude for the three electrolytes. Because of this the concentrations of the other ions did not change drastically. Therefore for simplicity the salting out effect is not taken into account.

Table 4.2: Initial equilibrium values for CO_2, HCO_3^-, HCO_3^{2-}, OH^- and the measured and calculated pH at different electrolytes at 19 °C and $101\,325$ Pa CO_2 partial pressure. The salting out effect was not taken into account.

Electrolyte	pH_{meter}	$c_{CO_{2(aq)}}$	$c_{HCO_3^-}$	$c_{CO_3^{2-}}$	c_{OH^-}	pH_{calc}
0.4 M K_2SO_4	5.3	3.9×10^{-2}	1.3×10^{-4}	4.7×10^{-11}	7.6×10^{-11}	3.9
0.1 M $KHCO_3$	6.6	3.9×10^{-2}	0.1	2.7×10^{-8}	5.7×10^{-11}	6.8
1 M $KHCO_3$	7.4	3.9×10^{-2}	1.0	2.6×10^{-3}	5.7×10^{-7}	7.8

From Table 4.2 can be seen that the concentration of bicarbonate, the main buffering component, differs largely for the three electrolytes. We expected that the electrolyte with higher HCO_3^- concentration should have more buffering effect and show little to no increase in pH at the cathode. The more common buffer capacity β follows these same difference between the three electrolytes. From this we expect the same.

In Figure 4.7 the electrolytes are given from left to right in order of increasing buffer capacity and HCO_3^- concentration. The bulk pH of these electrolytes also is increasing with buffer capacity and bicarbonate concentration. This was also shown in subsection 4.1.3. The difference between the phase-shift fluorescence lifetime inside the bulk and at the cathode is the largest for the least buffered electrolyte, 0.4 M K_2SO_4. The pH change between the bulk and the cathode surface is decreasing with

increasing buffer capacity. This is clearly shown in figures **g**, **h** and **f**. Here the pH profile is displayed over the width of the electrolyte channel.

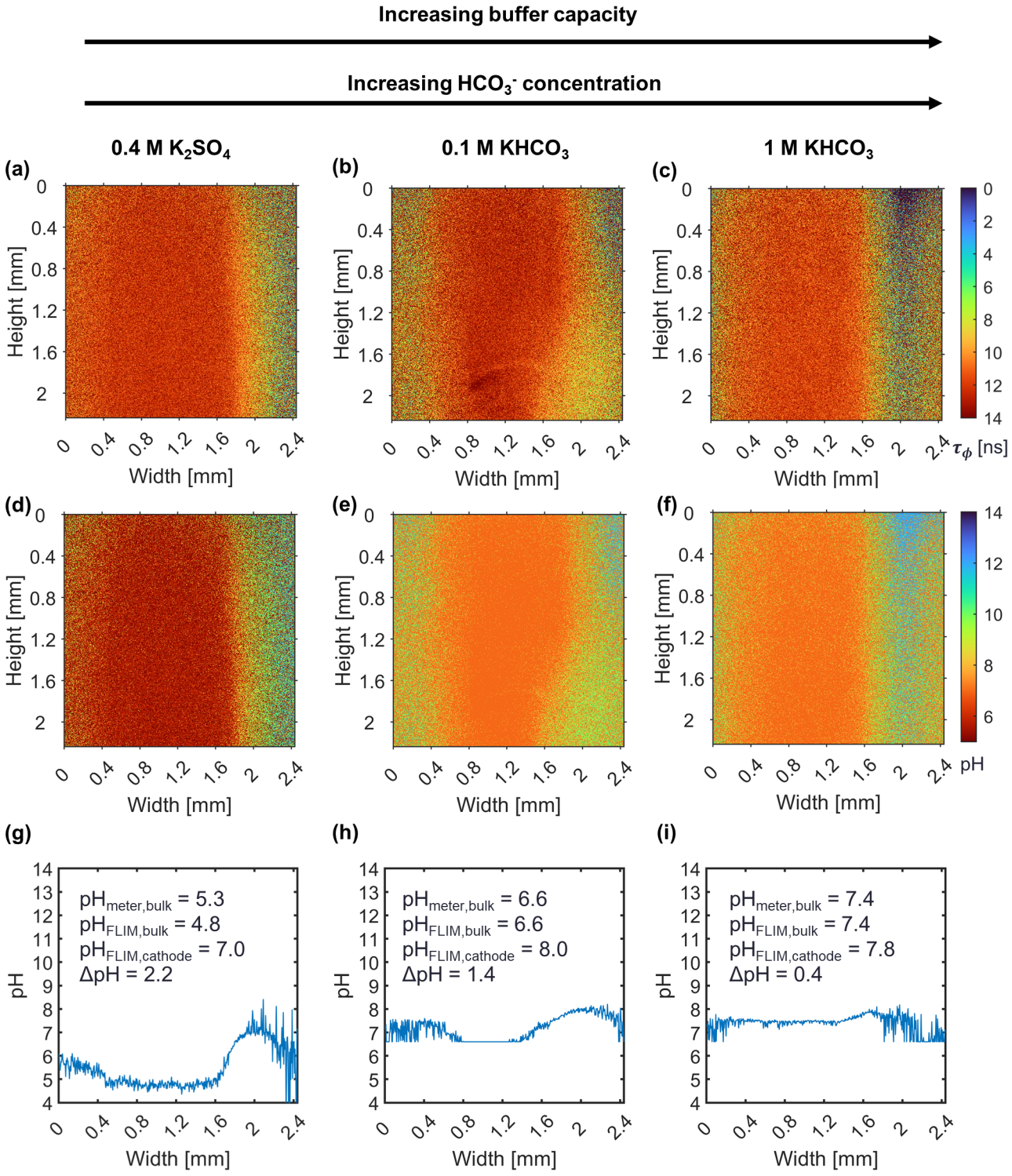

Figure 4.7: Decreasing fluorescence lifetime and increasing pH at the cathode compared to bulk pH with decreasing buffer capacity of the electrolyte. The same parameter set for three different electrolytes: $-10\,\mathrm{mA\,cm^{-2}}$, $Re = 8$, in the middle of the cell (position 2) and $2\,\mathrm{mm}$ as channel thickness. Figures **a**, **b** and **c** display the local phase-shift fluorescence lifetime (τ_ϕ) in ns over the height and width of the frame for the three different electrolytes. The fluorescence lifetime (τ_ϕ) ranges from 0 to 14 ns. Figures **d**, **e** and **f** display the calculated local pH from the lifetime-pH calibration curve for both $KHCO_3$ and K_2SO_4. The final three figures **g**, **h** and **i** show the pH profile which is the average over the height of the frame. This average is taken from 100 to 400 pixels (the image has a total of ± 500pixels. This is according to $4.76\,\mu\mathrm{m} = 1$pixel with an 5x objective.

The increase in pH compared to the bulk and the increase in OH^- concentration are the following for

each electrolyte:

- for 0.4 M K_2SO_4: $\Delta pH = 2.2$, $\Delta c_{OH^-} = 9.9 \times 10^{-8}\,\text{mol}\,\text{L}^{-1}$,
- for 0.1 M $KHCO_3$: $\Delta pH = 1.4$, $\Delta c_{OH^-} = 9.6 \times 10^{-7}\,\text{mol}\,\text{L}^{-1}$,
- for 1 M $KHCO_3$: $\Delta pH = 0.4$, $\Delta c_{OH^-} = 3.8 \times 10^{-7}\,\text{mol}\,\text{L}^{-1}$.

The bulk pH for each of the electrolytes is similar to the initial bulk pH as measured at the start of the experiment. This pH is dependent on the type and concentration of the electrolyte. Only K_2SO_4 shows a difference between the pH measured with the pH-meter and the pH obtained via the fluorescence lifetime-pH calibration curve. The reason for this can be that the trend between τ_ϕ and the pH is plateau like in the region around pH 6. We can see this in Figure 4.5 **b**. Therefore it is more difficult to distinguish an accurate pH in this region.

To validate these observed changes in pH estimations of the theoretical pH change were done. The increase in OH^- concentration due to an applied current density of $-10\,\text{mA}\,\text{cm}^{-2}$ is $2.2 \times 10^{-3}\,\text{mol}\,\text{L}^{-1}$. To do these calculations on the final ion concentrations the following assumptions were made:

- The following 3 reactions are taking place inside the electrolyte: $CO_{2,(aq)} + OH^- \rightleftarrows HCO_3^-$, $HCO_3^- + OH^- \rightleftarrows CO_3^{2-} + H_2O$ and $H_2O \rightleftarrows OH^- + H^+$.
- The electrolyte is homogeneously mixed over the entire width of the channel.
- The current density is $-10\,\text{mA}\,\text{cm}^{-2}$.
- The charge is balanced.
- $Re = 8$, this corresponds to a flow velocity of $1.4\,\text{mL}\,\text{min}^{-1}$.

A full description of these calculations is given in Appendix C. Half way in the channel ($y = 1.25\,\text{mm}$) the theoretical pH change is as follows:

- for 0.4 M K_2SO_4: pH increases from 3.9 to 8.7
- for 0.1 M $KHCO_3$: pH increases from 6.8 to 8.3
- for 1 M $KHCO_3$: pH increases from 7.8 to 8.0

For the two bicarbonate electrolytes the estimation of the pH is slightly off for both the initial and the final pH. This could mean that our initial estimations for the concentrations of the species present in the electrolyte are not completely true as given in Table 4.2.

For the K_2SO_4 electrolyte however both pH values are even further apart from the measured or seen pH in the figure. An explanation for the lower initial pH value compared to the one measured with the pH meter could be that the presence of SO_4^{2-} can buffer the acidification of the electrolyte when it is saturated with CO_2. For the higher estimated pH in the middle of the channel when applying a current density the same can be stated. In the theoretical pH change calculations we do not take into account buffering of SO_4^{2-}. This buffer capacity is very small with its acid dissociation constant $pKa = 1.9$. We do only take this buffering into acccount for our calculations of the buffer capacity as given in Table 4.1.

The increase in pH at the cathode is different for each of the electrolytes, because of the different buffer capacities of the electrolyte. This buffer capacity (β) is quantitatively described in Table 4.1. It is also quantitatively shown in Table 4.2 in the concentration of the bicarbonate ions inside the electrolyte.

The buffering reactions as described in subsection 2.2.2 stabilize the pH. This buffering can be explained by the stoichiometry and the reaction rates of the buffering reactions. Both reactions are influenced by the pH as they both have OH^- as a reactant species. These two buffering reactions are given below with their reaction rate constant.

$$\frac{c_{HCO_3^-}}{c_{CO_2(aq)} c_{OH^-}} = \frac{k_1^f}{k_1^b} = \frac{2.23\,\text{m}^3\,\text{mol}^{-1}\,\text{s}^{-1}}{5.23\,\text{s}^{-1}} = K_1 = 4.44 \times 10^4\,\text{m}^3\,\text{mol}^{-1} \tag{4.1}$$

$$\frac{c_{CO_3^{2-}}}{c_{HCO_3^-} c_{OH^-}} = \frac{k_2^f}{k_2^b} = \frac{6 \times 10^6\,\text{m}^3\,\text{mol}^{-1}\,\text{s}^{-1}}{1.25 \times 10^6\,\text{s}^{-1}} = K_2 = 4.8\,\text{m}^3\,\text{mol}^{-1} \tag{4.2}$$

According to the stoichiometry of the reaction of conversion of CO_2 to HCO_3 is responsible for the unwanted consumption of the aqueous CO_2. We do not want this consumption, because then this CO_2 can no longer react to form CO in the electrochemical conversion. The consumption reaction of CO_2 with OH^- has a forward reaction rate that is magnitudes slower than the reaction rate of the reaction between bicarbonate and hydroxide to carbonate. The bicarbonate is consumed as it reacts with OH^-. This will reduce the rate at which the pH increases (buffering effect). It also leads to an decrease in $HCO_3{}^-$ concentration. This shifts the balance in the first reaction and leads to an increased rate of CO_2 consumption [10].

This description of what happens within the electrolyte and the different buffering reactions shows us two parts of this buffering effect with $HCO_3{}^-$. The first is rate decreasing of the pH increase. The second is the impact of these reaction on the CO_2 concentration within the electrolyte. It is interesting to also investigate different buffering electrolytes such as those containing a phosphate buffer, since these inhabit the buffering effect without impacting the availability of CO_2 [47].

An interesting observation is the rather small increase in pH and OH^- concentration for the 0.4 M K_2SO_4 electrolyte. From the small buffer capacity and the low concentration of $HCO_3{}^-$ we would expect a larger increase near the electrode. Overall the lowest pH near the electrode is for the least buffered solution (0.4 M K_2SO_4). It is followed by the most buffered electrolyte 1 M $KHCO_3$. The 0.1 M $KHCO_3$ electrolyte has the highest pH near the electrode. Therefore we assume that buffering still happens inside the sulphate electrolyte. Here the main buffering species would be CO_2 instead of $HCO_3{}^-$. The concentration of CO_2 is relatively large compared to $HCO_3{}^-$. The production of OH^- via the electrochemical route can lead to the increase of $HCO_3{}^-$ via the first buffering reaction. This produced $HCO_3{}^-$ can then act as the buffering species. Another buffering species can be $SO_4{}^{2-}$. However, the pKa of the this species is very low and we therefore do not expect that this is the main reason for the lower than expected increase in pH.

In Appendix D we have calculated the buffer capacity of all the buffering species inside the electrolyte. We have done this to obtain an insight in the main buffering species of the electrolyte. The data in Table D.1 however cannot explain the relatively low increase in pH in the K_2SO_4 electrolyte.

4.2.2. Effect of conductivity

The three electrolytes are also different in their conductivity, because of the ion concentration and types of ions. The conductivity was measured for each electrolyte (κ_{measured} in S cm^{-1}). The theoretical ohmic drop over the electrolyte can be calculated from this measured conductivity, the current density and the width of the channel. These values are given in Table 4.3.

In Table 4.3 we can see that the measured conductivity is increasing in the following order: 0.1 M $KHCO_3$ < 1 M $KHCO_3$ < 0.4 M K_2SO_4. The conductivity of an electrolyte is made up of the number of ions, the charge of the ions and the mobility of those ions [60]. From the number of ions it is as expected that the 0.1 M $KCHO_3$ has the lowest conductivity. The concentration of ions present in the electrolyte is as follows: 0.2 mol L^{-1} in 0.1 M $KHCO_3$, 2 mol L^{-1} in 1 M $KHCO_3$ and 1.2 mol L^{-1} in 0.4 M K_2SO_4. The $SO_4{}^{2-}$ however has a larger charge than the $HCO_3{}^-$ ion. This difference can explain the closeness of the conductivity of 0.4 M K_2SO_4 and 0.1 M $KHCO_3$. We expect the cell potential increases with decreasing conductivity. This is also reflected into the theoretical ohmic drop as shown in Table 4.3. The ohmic drop increases with decreasing conductivity of the electrolyte.

Table 4.3: The effect of different conductivity per electrolyte: 0.4 M K_2SO_4, 0.1 M $KHCO_3$, 1 M $KHCO_3$. As well as the effect of the different catholyte thicknesses according to the following equation: $\eta_{\text{catholyte}} = \frac{jl}{\kappa}$.

Electrolyte	κ_{measured} [S cm^{-1}]	$\eta_{\text{catholyte}}$ [mV] at -10 mA cm^{-2}		
		0.25 mm	1 mm	2 mm
0.1 M $KHCO_3$	7.7×10^{-3}	32.5	130	260
1 M $KHCO_3$	5.1×10^{-2}	4.9	19.7	39.4
0.4 M K_2SO_4	6.8×10^{-2}	3.7	14.7	29.4

The initial plan for this thesis was to also investigate the effect of the channel thickness. Three widths

were used: 0.25 mm, 1 mm and 2 mm. The effect of the channel width of the overall cell potential is displayed in Appendix E. It was expected that the overpotential over the catholyte channel would be smaller with a thinner channel width. However, from the experiments it was concluded that bubbles were getting stuck inside the channel. This lead to very high potentials. The catholyte channel with a thickness of 2 mm has given us the reliable results as well as the possibility to look inside with the use of FLIM. Therefore we decided to only look into the 2 mm case.

In Figure 4.8 the effect of the current density on the potential for the three different electrolytes is displayed. In the figure the potential is given from the cathode to the micro-reference electrode between the anode and the membrane (MRE_{AEM}). The case displayed is the 2 mm case.

In general we see that the potential is increasing with the increasing current density. This is according to expectations since the ohmic potential is a function of the current density. Another observation are the large error bars. We have calculated both the error over the current density as well as over the potential. These larger error bars are especially visible for the higher current densities. Here we can also see the error bar in the current density. This is because the maximum potential of the potentiostat was reached. The potential is therefore more stable at this maximum potential while the current density is fluctuating more to try to reach the set current density of $50\,\mathrm{mA\,cm^{-2}}$. The reason for these larger error bars can be due to gas bubble formation inside the electrolyte. Lee, Zhao, Lee, *et al.* describe that the production of syngas inside the electrolyzer leads to an unstable cell voltage rather than the presence of CO_2 bubbles inside their electrolyzer [61]. When gas bubbles are released the potential drops slightly. The charge path is decreased when the bubbles are removed or there are less bubbles inside the channel. However, we do not expect the electrolyte type to have an effect of the amount of gas bubbles present inside the channel.

The potential from the cathode to AEM can contain some measurement error since different measurement methods were used for different cases due to some technical issues.

Figure 4.8 also show an increasing potential with a less conductive electrolyte (0.1 M $KHCO_3$). It shows lower potentials with higher conductivity of the used electrolyte (1 M $KHCO_3$ and 0.4 M K_2SO_4).

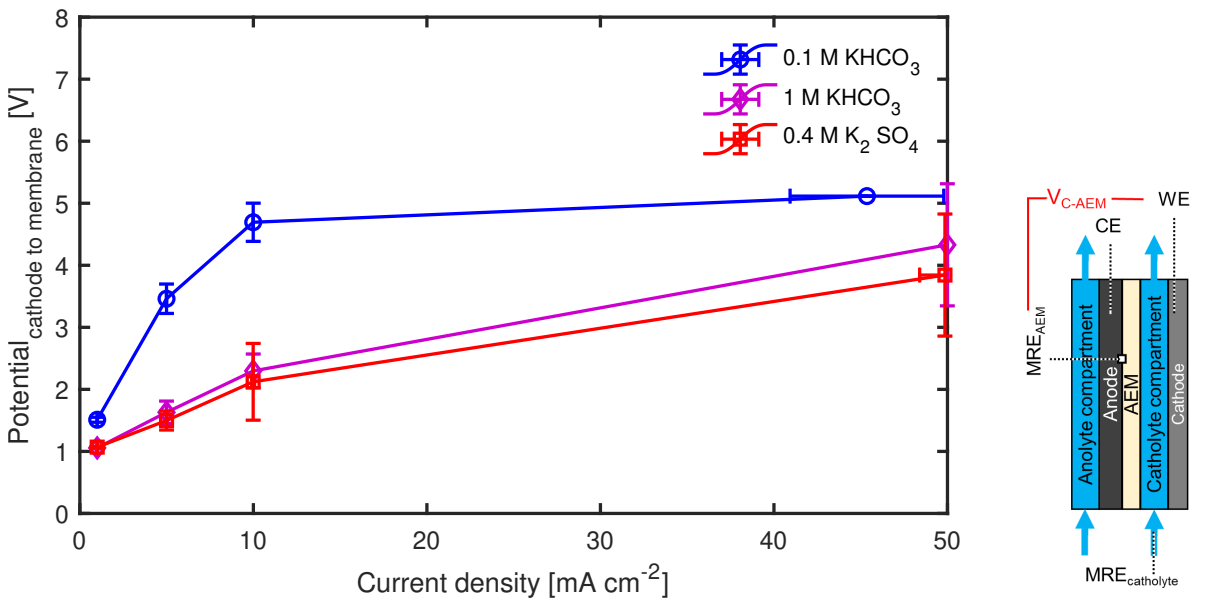

Figure 4.8: Increasing potential with increasing current density and with decreasing electrolyte conductivity of the three different electrolytes. The potential is measured from cathode (WE) to the membrane ($MRE_{membrane}$) (E) displayed in V with its standard deviation. The current density (j) is displayed in $\mathrm{mA\,cm^{-2}}$ with its standard deviation. $Re = 8$. On the right of the graph an overview of the cell is displayed and where the different electrodes are located.

To further investigate the differences in potential for the different conductivities of the electrolytes Fig-

ure 4.9 is used. In Figure 4.9 four components are shown for each of the electrolytes. The cathode potential is displayed in V vs SHE. This is to show that the cathode potential is not affected by the conductivity of the electrolyte. Here we can not detect a correlation between the different electrolyte and the cathode potential.

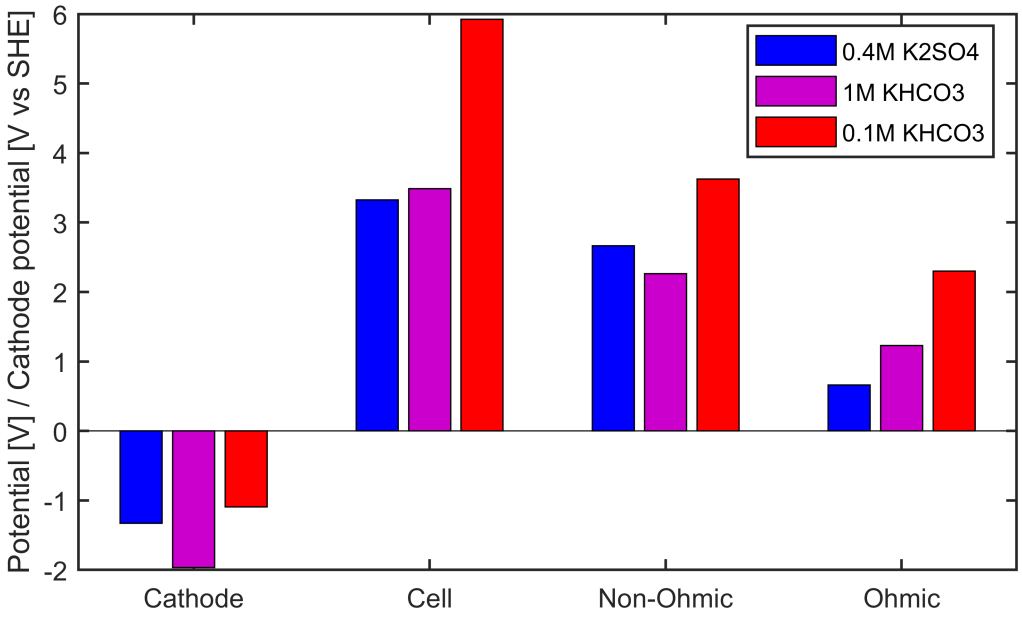

Figure 4.9: The cathode potential, the cell potential and its ohmic and non-ohmic parts displayed for the three electrolytes. The parameter set is as follows: 2 mm catholyte channel thickness, $Re = 8$, $j = -10\,\mathrm{mA\,cm^{-2}}$

The second component is the overall cell potential. This cell potential is broken up into its non-ohmic and ohmic parts. In the method that was used the ohmic part of the potential is overestimated since the measurement time step was too large to accurately estimate the ohmic part of the potential.

We would expect to see the main effect of the different electrolyte in the ohmic part of the cell potential. The theoretical ohmic drop over the electrolyte is a function of the conductivity as shown earlier. When comparing the ohmic parts to the theoretical ohmic drop in Table 4.3 we see however that the ohmic drop over the catholyte is magnitudes smaller than the ohmic part of the cell potential.

The overpotential over the electrolyte however can also be influenced by other aspects inside the electrolyte: the presence of bubbles and the concentration overpotential. Decrease in buffering capacity would lead to increase in pH difference between bulk and cathode. Which could be described as an increase in the concentration differences between bulk and electrode surface leading to increase in concentration overpotential. The concentration differences between the bulk and at the cathode are given in the previous section. The concentration overpotential is a function of the logarithmic of the ratio between the concentration at the cathode and the bulk concentration.

$$\eta_{\mathrm{conc}} = \frac{RT}{nF} \ln \frac{c_{\mathrm{surface}}}{c_{\mathrm{bulk}}} \tag{4.3}$$

The values of the pH and concentration of OH^- in the bulk and at the cathode, the difference between those, the ratio between those and the logarithmic of this ratio are given in Table 4.4. From this we would expect that the concentration overpotential is the largest for 0.4 M K_2SO_4 electrolyte. However, we can also see that the order of magnitude for the calculated concentration overpotentials is much smaller than the potentials as given in Figure 4.9. Therefore we cannot detect a relation in the non-ohmic component of the cell potential in Figure 4.9.

Table 4.4: Overview of pH values near the cathode and inside the bulk together with the corresponding OH^- concentration, the difference in concentration, the ratio between these two concentration and the concentration overpotential calculated with Equation 4.3. All the concentration are given in mol L^{-1} and the concentration overpotential is given in V

Electrolyte	$pH_{\textbf{bulk}}$	$c_{OH^-}^{\textbf{bulk}}$	$pH_{\textbf{cathode}}$	$c_{OH^-}^{\textbf{cathode}}$	Δc_{OH^-}	$\frac{c_{OH^-}^{cathode}}{c_{OH^-}^{bulk}}$	η_{conc} [V]
0.4 M K_2SO_4	4.8	$6.309\,57 \times 10^{-10}$	7	1×10^{-7}	9.9×10^{-8}	158.5	6.4×10^{-2}
0.1 M $KHCO_3$	6.6	4.0×10^{-8}	8	1×10^{-6}	9.6×10^{-7}	25.1	4.1×10^{-2}
1 M $KHCO_3$	7.4	2.5×10^{-7}	7.8	6.3×10^{-7}	3.8×10^{-7}	2.5	1.2×10^{-2}

4.3. Effect of current density

In this section the effect of applying a current density is reported. The first case that is shown is the 0.4 M K_2SO_4 electrolyte which as discussed in the previous section shows less buffering effects because of its lower buffer capacity and lower HCO_3 concentration. This case is used to show that with FLIM we can clearly see a difference in pH near the electrode between no current density applied and our largest current density ($-50\,\mathrm{mA\,cm^{-2}}$). In the second part of this section we show the effect of four different current densities on one case of $KHCO_3$ electrolyte. This electrolyte is known to have buffering capacities and therefore it is interesting to see what the effects are of increasing the current density and if these buffer capacities can keep up or if also other effects might be playing a role in pH changes.

4.3.1. Effect of applying a current density on K_2SO_4 electrolyte

Two cases for the $0.4\,\mathrm{mol\,L^{-1}}$ K_2SO_4 electrolyte are investigated to display the effect of applying a current on both the phase-shift fluorescence lifetime and the pH near the cathode and in the bulk electrolyte. These two cases are shown in Figure 4.10. The current density applied is $-50\,\mathrm{mA\,cm^{-2}}$.

The pH of $0.4\,\mathrm{mol\,L^{-1}}$ K_2SO_4 electrolyte is around pH 5.3 according to the measurement with the pH-meter at the start of an experiment. This should correspond to a phase-shift fluorescence lifetime (τ_ϕ) of $12.3\,\mathrm{ns}$ according to Figure 4.4. In Figure 4.10 **e** the average pH over the entire channel before applying a current is around pH 4.9. This is slightly lower than the measured pH with the pH-meter. The small difference can be explained by the measurement error as we see the error bars in Figure 4.4.

The figures where a current is applied (**b**, **d** and **f**) show a decrease in lifetime at the cathode side (**b**), an increase in pH at cathode (**d** and **f**). The pH near the electrode in **f** is close to pH 10.2. In comparison to the initial pH this is a change of $5\,\mathrm{pH\,units}$. From comparison of without (**e**) and with (**f**) a current density applied can also be stated that the bulk pH shows a slight increase in pH of about $1.5\,\mathrm{pH\,units}$. The pH increases to 6.5.

The increase in pH and thus the decrease in lifetime at the cathode can be linked to the production of OH^- at the cathode. These hydroxide ions are produced via the electrochemical reactions of CO_2 reduction and HER occurring at the cathode. We can clearly show that an effect of applying a current density can be observed in the decrease in lifetime and increase in pH.

The obtained images can be used to make an estimate of the thickness of the boundary layer. The cathode seems to be located at around $2\,\mathrm{mm}$. As stated in the earlier section on the FLIM validation it is rather difficult to indicate where the cathode is located in these FLIM images. The boundary layer is around $0.4\,\mathrm{mm}$ in thickness.

4.3.2. Effect of increasing current density on $KHCO_3$ electrolyte

In Figure 4.11 the effect of an increasing current density is displayed. The current density is varied from $j = -1, -5, -10$ and $-50\,\mathrm{mA\,cm^{-2}}$. The parameter set is as follows: 1 M $KHCO_3$, $Re = 8$, middle of the cell (position 2) and $2\,\mathrm{mm}$ as channel thickness. The effects are shown in three types of images per current density: phase-shift fluorescence lifetime image, pH image and the pH profile over the width of the channel.

The first important observation to make is the difference between the bulk pH as determined using FLIM and its phase-shift fluorescence lifetime to pH calibration curve. For each of the current densities a lower bulk pH is seen than the bulk pH of 7.4 as measured with the pH meter at the start of the experiment. This difference is most likely due to relatively large error inside the calibration curve.

However, when comparing the lowest to the highest current density ($-1\,\mathrm{mA\,cm^{-2}}$ to $-50\,\mathrm{mA\,cm^{-2}}$) we can see an increase in bulk pH determined from fluorescence lifetime obtained via FLIM and converted through the calibration curve. as determined using FLIM. This increase is equal to $0.4\,\mathrm{pH\,units}$.

As the current density is increasing we see the pH at the cathode increasing. Most prominently visible in the two cases with the largest current densities ($j = -10\,\mathrm{mA\,cm^{-2}}$ and $j = -50\,\mathrm{mA\,cm^{-2}}$ we observe an increase in pH near the cathode compared to the initial bulk pH of 7.4. For both these

current densities this increase is equal to 0.7 pH units. For the $-50\,\mathrm{mA\,cm^{-2}}$ case both the pH of the bulk and near the cathode are higher in comparison to both of these of the $-10\,\mathrm{mA\,cm^{-2}}$ case.

For the lower current densities no effect can be seen in the pH profiles over the channel width.

At higher current densities more OH^- is produced. An overview of the concentration of OH^- per current density being produced is given in Table 4.5. This table gives an overview of the amount of OH^- being produced per current density ($\dot{N_{OH^-}}$) as according to the equation below. It also gives the value for the increase in OH^- concentration (P_{OH^-}) half way inside the channel, at 1.25 cm of 2.5 cm long electrode. From this increase in concentration and the initial pH of 7.4 the new pH is calculated. This pH does not take into account any consumption of OH^- via the buffering reactions.

$$\dot{N_{OH^-}} = \frac{j \cdot A_{\text{electrode}}}{F} \tag{4.4}$$

$$P_{OH^-} = \frac{\dot{N_{OH^-}}}{\dot{V}} \cdot \frac{y = 1.25\,\text{cm}}{y = 2.5\,\text{cm}} \tag{4.5}$$

j	$\dot{N_{OH^-}}$	P_{OH^-} at $y = 1.25$ cm	pH without buffering effects
$1\,\mathrm{mA\,cm^{-2}}$	$1.0 \times 10^{-8}\,\mathrm{mol\,s^{-1}}$	$0.2\,\mathrm{mol\,m^{-3}}$	10.3
$5\,\mathrm{mA\,cm^{-2}}$	$5.2 \times 10^{-8}\,\mathrm{mol\,s^{-1}}$	$1.1\,\mathrm{mol\,m^{-3}}$	11.0
$10\,\mathrm{mA\,cm^{-2}}$	$1.0 \times 10^{-7}\,\mathrm{mol\,s^{-1}}$	$2.2\,\mathrm{mol\,m^{-3}}$	11.3
$50\,\mathrm{mA\,cm^{-2}}$	$5.2 \times 10^{-7}\,\mathrm{mol\,s^{-1}}$	$11.1\,\mathrm{mol\,m^{-3}}$	12.0

Table 4.5: An overview of the amount of OH^- being produced, the increase in OH^- concentration half way inside the channel and the value for the pH when no buffering effect are taken into account to consume OH^-.

From Table 4.5 we can tell that large amounts of OH^- are produced within the cell. This can lead to an increase of pH at the electrode when the buffering capacity of the electrolyte is no longer large enough.

In our case the production of OH^- via the HER or COER should not lead to an overall increase of the bulk pH. This is because the Reynolds number that is used in the displayed case would lead to laminar flow profile. Since we assume the flow similar to that as pipe flow a laminar flow profile is expected. Also the pH boundary layer that we see is not reaching very far into the channel. From these assumptions it is not expected that the overall pH inside the bulk will be influenced by the reactions at the cathode.

An explanation to the overall increase of pH is seen for $-50\,\mathrm{mA\,cm^{-2}}$ should be that there is also mixing perpendicular to the flow direction. Vortexes can be created through the surface roughness of the GDE. However, a better explanation for this mixing is the presence of gas bubbles inside the channel or at the cathode. With the increase in current density also the amount of gas present inside the channel will increase because more H_2 or CO is formed. Both these species have a lower solubility than CO_2, the dissolved gas reacting towards CO. The presence of these gas bubbles as well as the increase in amount of gas bubbles can lead to more lateral mixing inside the electrolyte channel. This in its turn would lead to improved mass transfer. Therefore it decreases the boundary layer near the electrode. It also can increase the bulk pH.

Since the effect of these gas bubbles is quite important we would suggest to further investigate this by using particle image velocimetry (PIV) to measure the flow profile. Within the research group F. Wiegel has researched this in a different electrochemical cell.

For the $50\,\mathrm{mA\,cm^{-2}}$ case the images of the fluorescence lifetime and pH are more disrupted. This also translates into the pH profile over the width of the channel. The cause for this can be the presence of more gas bubbles. Since the current density is higher more H_2 or CO is produced. These both have a lower solubility in the electrolyte causing more gas bubbles to form. These gas bubbles can disrupt the flow as well as lead to irregularities in the fluorescence lifetime values obtained. The irregularities can be due to reflection as well as higher variance in fluorescence lifetime.

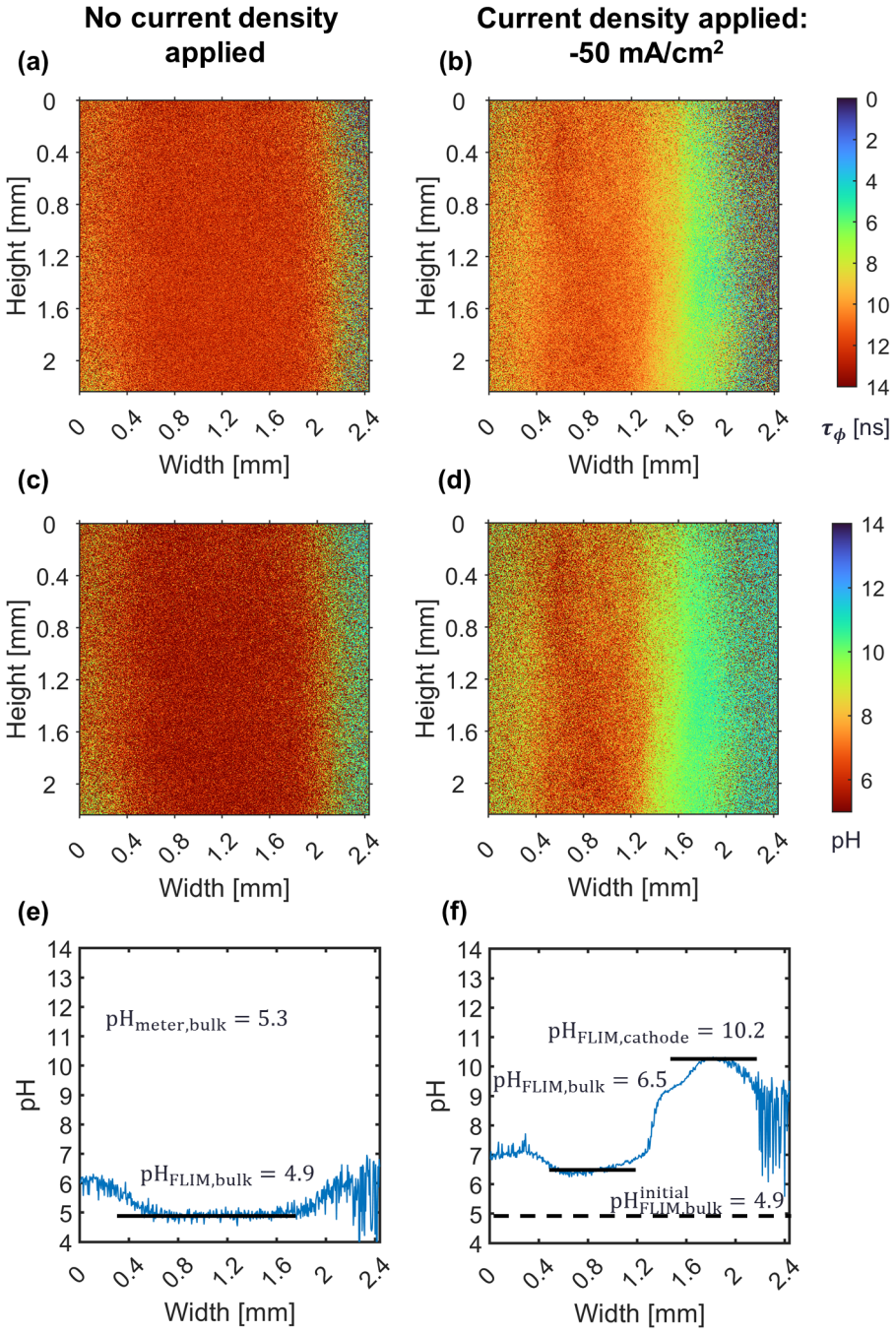

Figure 4.10: A decrease in phase-shift fluorescence lifetime (τ_ϕ) and an increase in pH at the cathode as a result of applying a current density. Two cases are displayed for 0.4 M K_2SO_4 electrolyte. The left three figures (**a**, **c** and **e**) are for the case where no current is applied. The three right figures (**b**, **d** and **f**) display the case where there is a current density applied of $-50\,\mathrm{mA\,cm^{-2}}$. The flow rate inside the cell is $1.4\,\mathrm{mL\,min^{-1}}$ and the part of the electrochemical cell in view is the middle of the channel (position 2). In **a** and **b** the local phase-shift fluorescence lifetime, τ_ϕ, is displayed over the view on the catholyte channel. In **c** and **d** the pH calculated from the calibration curve over the view on the catholyte channel is shown. **e** and **f** show the pH profile over the width of the frame. The pH increases from 4.9 to 10.2 at the cathode and 6.5 inside the bulk of the electrode.

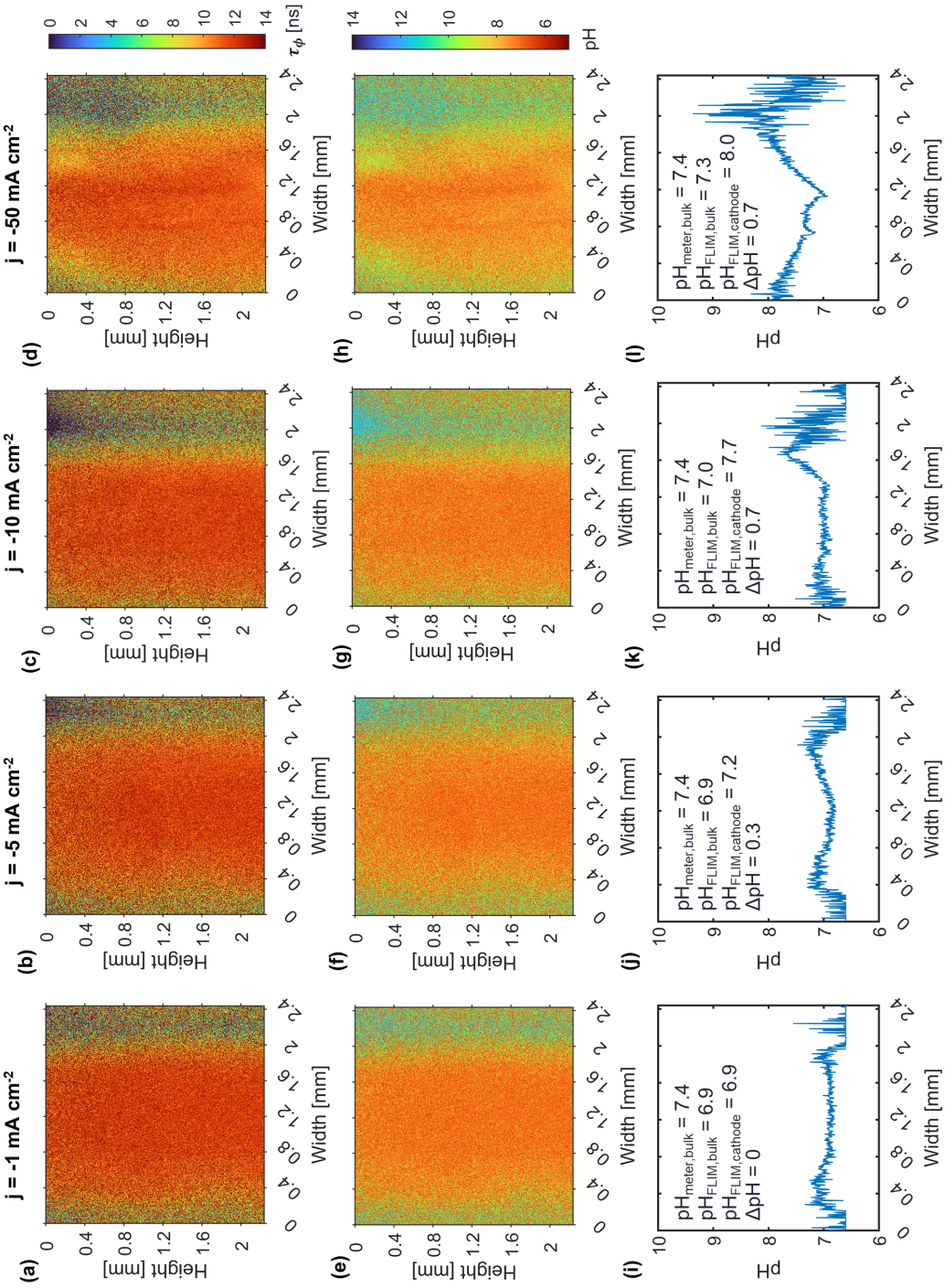

Figure 4.11: Increasing pH near the cathode and in the electrolyte bulk as an effect of increasing the current density. The same parameter set for four different current densities: $Re = 8$, 1 M $KHCO_3$, middle of the catholyte channel (position 2). **a**, **b**, **c** and **d** show the local phase-shift fluorescence lifetime (τ_ϕ) in ns displayed over the view of the catholyte channel. In **e**, **f**, **g** and **h** the local pH calculated from the fluorescence lifetime-pH calibration curve over the catholyte channel. Figures **i**, **j**, **k** and **l** show the pH profile over the width of the frame. The pH near the cathode is increasing with increasing current density and the bulk pH for the $-50\,\mathrm{mA\,cm^{-2}}$ has also increased slightly.

4.4. Effect of the Reynolds number

In this thesis three Reynolds numbers are used to perform experiments: $Re = 0.8, 8$ and 47. Since we also used different channel thickness this means that the flow rate is varying dependent on the Reynolds number we want to achieve. The Reynolds number is a function of both the flow speed and the hydraulic diameter (and thus the channel width). The different Reynolds number therefore have an effect on both the flow inside the catholyte and anolyte channel. For the catholyte channel we can more in depth study this effect by using FLIM. However, we should also be able to see the effect of both catholyte and anolyte flow rate in the overall cell potential.

We expect an increasing Reynolds number to have the following effects:

1. The pH near the electrode increases less with an increasing Re number. This is because the electrolyte near the electrolyte should be renewed often since the overall flow in line with the wall is larger.
2. The pH inside the bulk of the electrode is expected not to change since with the current Re numbers used the flow profile should be described as laminar flow. Therefore no convection perpendicular to the flow direction should occur. The only mass transfer mechanisms we should encounter are migration and diffusion.
3. The overall cell potential is expected to decrease with increasing Re number, because the concentration overpotential should be lower if as expected the concentration at the electrode is roughly equal to the concentration in the bulk because of renewal of electrolyte happens faster because of the faster flow rate.
4. The overall cell potential is expected to decrease with increasing Re number, because the ohmic overpotentials should be lower. This is expected because with larger flow rate the relative gas fraction should be lower since these gas bubbles are more easily removed from the electrolyte channel as well as from the electrode.

The results of changing the Reynolds number are shown in two figures. Figure 4.12 shows us three cases with a different Reynolds number increasing from left to right. The case is as follows: $-10\,\text{mA cm}^{-2}$, 1 M $KHCO_3$ and at the end of the catholyte channel (position 1). In the figures **g**, **h** and **i** we can best distinguish the effects. The main observations made are:

- The bulk pH of the lowest Reynolds number ($Re = 0.8$) has increased in comparison to the pH measured with the pH-meter at the start of the experiment ($pH = 7.4$). It also increased in comparison to the two other Re numbers where the pH is around 7.
- The pH near the cathode is increasing with a decreasing Reynolds number: $pH = 9.2 > 7.9 > 7.6$.
- The thickness of the boundary layer is increasing with a decreasing Reynolds number. Our estimations for the boundary layer thickness are: $d = 1 > 0.5 > 0.3$ cm.

The cell is designed such that the flow at the electrode is a fully developed laminar flow. This means that the velocity boundary layer is stable over the whole electrode length. However, the development of the concentration boundary layer (and with that the pH boundary layer) is not yet fully developed.

In general we would expect the increasing velocity of the liquid and thus the increasing Reynolds number $Re \sim v$ from $Re = \frac{vD_H}{\nu}$.

Since we use $Re < 5 \times 10^5$ and we assume the flow to be similar to laminar flow in a pipe we can use the following relation between Sherwood, Schmidt and Reynolds numbers:

$$Sh = \frac{k_m d_c}{D} = 1.86 \frac{ReSh}{L/d_c} \tag{4.6}$$

So from theory we would expect the following for an increasing Reynolds number:

- Increasing velocity corresponds to an increasing Reynolds number.
- With an increase in the Reynolds number the Sherwood number increases with $Re^{1/3}$
- Sherwood gives the ratio between convective mass transfer to diffusive mass transfer and gives a relation to the mass transfer coefficient (k_m). With an increase in the Sherwood number the mass transfer coefficient increases similarly.

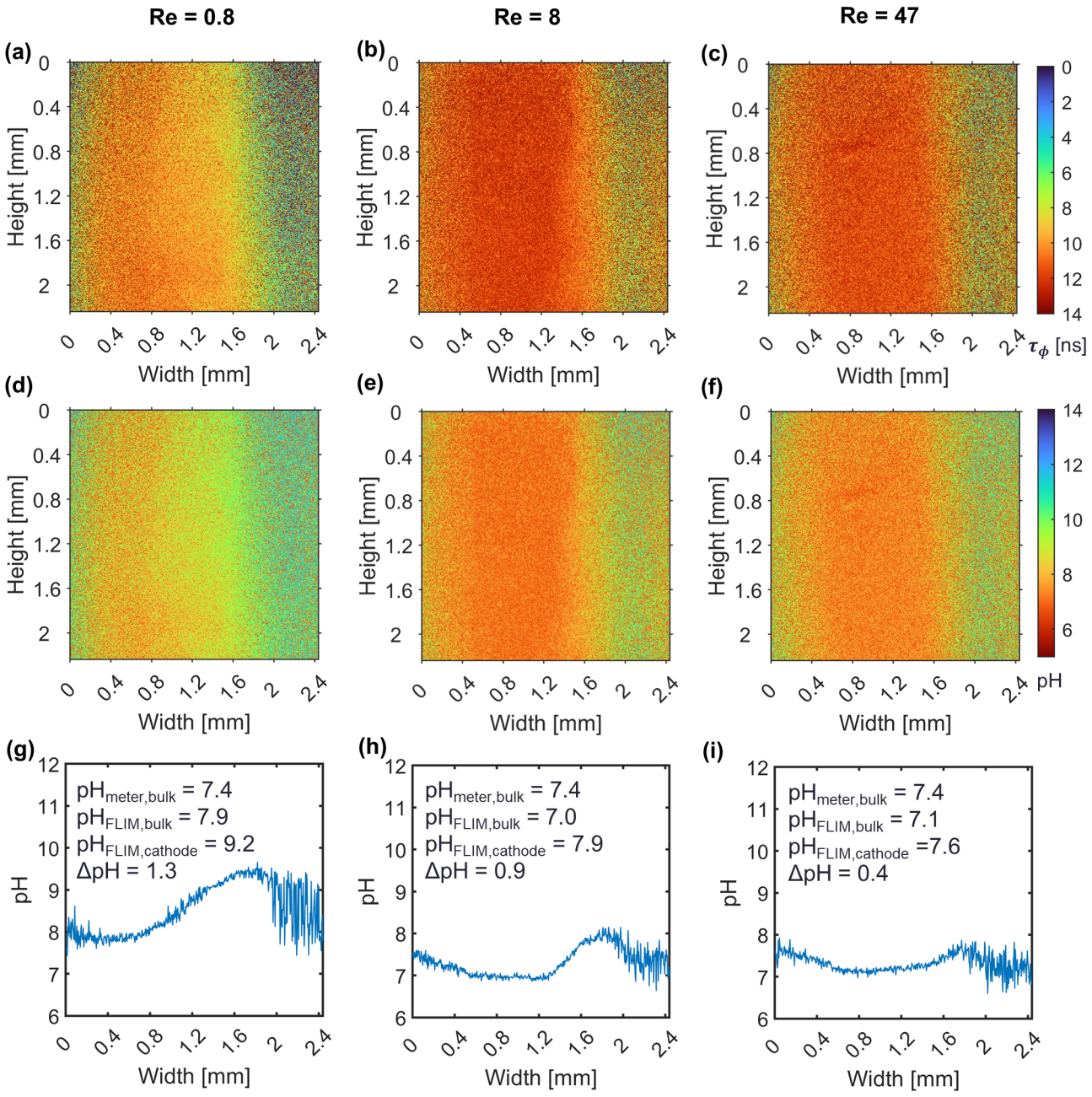

Figure 4.12: Increasing pH and pH boundary layer near the cathode and increasing pH of the electrolyte bulk as an effect of decreasing the Reynolds number. The same parameter set for three order of Reynolds number: $-10\,\mathrm{mA\,cm^{-2}}$, 1 M $KHCO_3$, end of the catholyte channel (position 1). **a**, **b** and **c** show the local phase-shift fluorescence lifetime (τ_ϕ) in ns displayed over the view of the catholyte channel. In **d**, **e** and **f** the local pH calculated from the fluorescence lifetime-pH calibration curve over the catholyte channel. Figures **g**, **h** and **i** show the pH profile over the width of the frame.

Similarly we can relate the channel width to the Sherwood number. So from theory we would expect the following for an increasing channel width:

- Increasing channel width leads to an increase in the hydraulic diameter.
- With an increase in the hydraulic diameter the Lewis number decreases.
- the Lewis number relates to the Sherwood number: $Sh \sim Le^{1/3}$. Therefore Sherwood decreases with $Le^{1/3}$
- With a decrease in the Sherwood number the mass transfer coefficient decreases similarly.

Next, Figure 4.13 shows us the effect of the Reynolds number on the potential from the cathode to the AEM. In this figure the three channel widths are displayed. The potential is given as a function of the Reynolds number. As already discussed earlier the smaller channel thickness are less reliable.

We observe a decrease in potential with increasing Re number for the 1 mm and 2 mm cases. We can explain this effect by looking at the different effect the Reynolds number can have on the potential.

- A higher Reynolds number and thus a higher flow rate can lead to better gas removal.
- A higher Reynolds number as shown in Figure 4.12 leads to less differences between the cathode and the bulk pH or concentrations. These lower concentrations differences can lead to less concentration overpotential.

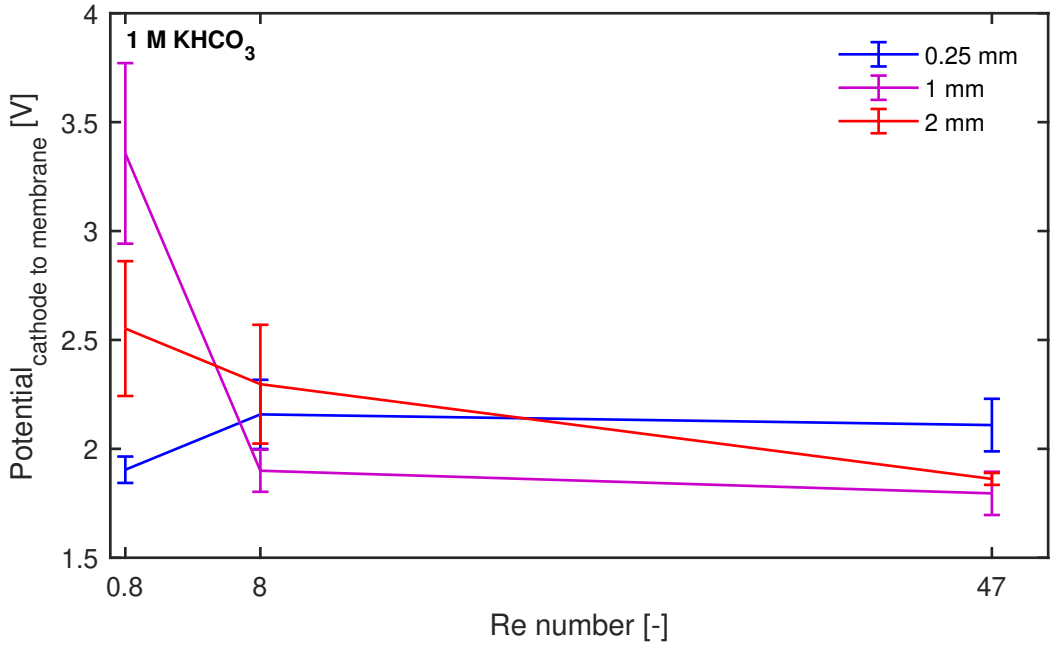

Figure 4.13: The potential from the membrane to the cathode displayed in V over the Reynolds number (dimensionless) for the three different channel width. The case is 1 M $KHCO_3$ at $-10\,\mathrm{mA\,cm^{-2}}$.

5

Conclusions

In this study, the influence of different process parameters (anion type and concentration of the electrolyte, current density and the Reynolds number) on the pH profile inside the catholyte channel of a CO_2 electrolyzer and on the cell potential was studied. This was done with the use of Fluorescence Lifetime Imaging Microscopy and by performing electrochemical tests.

What is the pH accuracy and spatial resolution of using FLIM in an electrochemical cell?
From the two calibration curves could be concluded that it is important to keep the same settings with FLIM experiments and the calibration to eliminate effects of the settings. However, this study did not find any clear correlation between the settings and its effect on the obtained phase-shift fluorescence lifetime. We also recommend that a new calibration needs to be performed when using a different reservoir. This was recommended even though no clear effect of the material or thickness of the container was distinguished.

The error bars of the calibration curve are quite large and in combination with the trend of the curve it is difficult to obtain a clear relation between the phase-shift fluorescence lifetime and the pH at a pH below 9. If we assume linearity for the region above pH 9 we can translate the error on the pH to be 0.38 pH units. In comparison to the region below pH 9 were we can translate this error onto the pH to be 2.1 pH units. These translations are a simplification since the fluorescence lifetime-pH relation is not a linear relation. When we convert the fluorescence lifetime images into a pH profile we take the average over 400 pixels in the length of the image. Therefore we assume the accuracy of these pH profiles to be rather good.

We also conclude that the used salt $KHCO_3$ is likely to have an effect on the performance of the alpha dye. This was shown by the bad fit of the bulk measurements of the two $KHCO_3$ electrolytes inside the calibration curve. This resulted in the use of two pH-fluorescence lifetime calibration curves in this project, one for each of the salts.

Insights into the spatial resolution of FLIM let us conclude that we have a spatial resolution of 4.76 µm. From the obtained 2D images as well as the profile of the phase-shift fluorescence lifetime could be seen that the end and beginning or membrane and cathode inside the part in view were difficult to distinguish.

An unexpected effect of using FLIM onto the resolution in an electrolyzer was due to the presence of bubbles. It was thought that the bubbles would not influence the 2D image of the fluorescence lifetime. However, the gas bubbles showed to have effect in the form of low intensity and lead to high variance in fluorescence lifetime. The gas bubbles also showed reflection of the light coming from elsewhere inside the channel.

What are the effects of the concentration and the anion type of the catholyte on the local and bulk pH inside the catholyte channel?
The three electrolytes were ranked to their buffer capacity. The effect of this buffer capacity as well as the bicarbonate concentration was shown with FLIM in terms of their increase in bulk pH and increase of pH between bulk and at the cathode. With increasing buffer capacity and increasing bicarbonate concentration of the electrolyte the pH difference between the bulk and near the cathode decreased. For the K_2SO_4 electrolyte the pH difference was 2.2 pH units for an applied current density of $-10\,\mathrm{mA\,cm^{-2}}$. The pH differences for the two bicarbonate electrolytes (0.1 M and 1 M) the values were 1.4 and 0.4 pH units respectively. From this we can conclude that we can clearly see a pH boundary layer near the cathode as well as make an estimation of the thickness of the boundary layer. We also conclude that the buffering species have an effect on the pH, since the amount of hydroxide ions produced is much larger in comparison to the increase in hydroxide ions as calculated from the change in pH. We have shown this with the theoretical calculations of the pH change for the 0.1 M and 1 M $KHCO_3$ electrolyte. However, the overall increase of hydroxide anions when comparing bulk to near the cathode was the lowest for the sulphate electrolyte. This was not as expected and even when splitting the buffer capacity of all buffering species could not be explained.

What are the effects of the concentration and the anion type of the catholyte on the cell potential?
The effect of the concentration and anion type of the electrolyte onto the cell potential was also studied. For this the conductivity of the electrolytes was measured. The overall cell potential at an applied current of $-10\,\mathrm{mA\,cm^{-2}}$ was the highest for the electrolyte with the lowest electrolyte conductivity (0.1 M $KHCO_3$, $\kappa_{\text{measured}} = 7.7 \times 10^{-3}\,\mathrm{S\,cm^{-1}}$). Similarly the lowest cell potential was recorded for the highest conductive electrolyte (0.4 M K_2SO_4, $\kappa_{\text{measured}} = 6.8 \times 10^{-2}\,\mathrm{S\,cm^{-1}}$).

With the use of micro reference electrodes as well as a current interrupt measurement the potential over different parts of the cell were calculated and their corresponding ohmic and non-ohmic potentials. However, this method prove to be not successful. Therefore only the non-ohmic and ohmic parts of the overall cell potential were investigated. The comparison of these potentials among the different electrolytes could not be linked to a clear effect of the anion type of concentration. We also conclude that the effect of bubbles is much larger than expected beforehand. We had also expected the effect of the concentration overpotential to be more apparent.

What are the effects of the flow rate and thus the Reynolds number of the catholyte on the local and bulk pH inside the catholyte channel?
From the study on the effect of the current density on the pH profile was concluded that other than expected there was mass transfer perpendicular to the flow of the electrolyte. We concluded that this mass transport could be an effect of the formation of hydrogen or carbon monoxide bubbles inside the electrolyte. These gas bubbles lead to more mixing of the bulk pH and especially for the $-50\,\mathrm{mA\,cm^{-2}}$ this shows an overall increase of the pH.

This was further illustrated with the study into the effect of the flow rate or the Reynolds number onto the pH profile inside the catholyte channel. The Reynolds number was low enough to assume laminar flow inside the channel. With the design of the cell the velocity boundary layer was fully developed. However, the concentration boundary layer and thus the pH boundary layer is still developing over the length of the channel or length of the cathode. The effect of increasing the Reynolds number is as expected. With the use of FLIM was proven that the pH near the electrode stayed more constant with an increasing Reynolds numbers. Following this reasoning the concentration overpotential would stay lower. We cannot distinguish the concentration overpotential in the overall cell potential. The potential decreased with an increasing Reynolds number. Beside the decrease in concentration overpotential due to more renewal of the electrolyte with a higher Reynolds number the removal of gas bubbles is also improved with a higher flow rate. We conclude that a combination of better gas removal and lower concentration overpotential is an explanation of the decrease in potential.

6

Recommendations

FLIM

The results of the two calibration curves and bulk measurements obtained with FLIM lead to the question on how the settings of the FLIM system influence the obtained fluorescence lifetime. An elaborate study into these effects is suggested to be done.

The results on the pH resolution of FLIM make us recommend to further research the effect of different anions, namely $KHCO_3$. The effect of $KHCO_3$ on the lifetime of the alpha dye should be further researched with a calibration using a $KHCO_3$ buffer series. Aside this it is also recommended to use different dye molecules dependent on the pH range of interest. The pH range studied in this project lies slightly below the region where the alpha dye shows a trend.

From our results on the spatial limitations we would recommend to further develop a method to obtain similar images with regards to the wall of the cell. Using an electronically controlled xy stage is suggested. In this way it would be easier to subtract the parts of the images that are outside the actual electrolyte channel. A study into the effect of different materials used inside the electrochemical cell onto the fluorescence of the dye and the materials their fluorescence is also interesting and might be able to subtract these effects on the obtained fluorescence lifetime.

Influences of mass transport

We would recommend that to support FLIM measurements Particle Image Velocimetry (PIV) used to obtain more insights in the flow profile inside the catholyte channel. The use of PIV can help us obtain more insight into the mass transfer due to the formation and removal of bubbles.

A deeper investigation into the effects of bubbles and the pH boundary layer is suggested. Especially, it is interesting to research the specific effects of these phenomena onto the distribution of the cell potential over the different components. It is suggested to further work out the multiple MRE method to obtain the potentials over different parts of the cell. Here we would recommend to do multiple experiments to make sure potentials are indeed a result of the current density over the component and not due to effect on the MRE itself. In combination with ratio between the conductivity and the effective conductivity of the electrolyte gap we can determine the gas fraction inside the electrolyte.

Implementation of more complexity into the system

It is recommended to implement the gas channel back into the electrochemical cell. Because of issues with the pressure balancing between the catholyte channel and the gas channel the gas channel was disregarded during this project. Therefore an important metric in CO_2 reduction was not discussed, the Faradaic efficiency towards CO. For the production of hydroxide ions and therefore the increase in pH this is still relevant. If the gas channel is implemented back into the electrochemical cell the CO_2 inside the electrolyte should no longer be consumed in large numbers in the electrochemical cell since this CO_2 now comes from the gas channel. Then the CO_2 inside the electrolyte can be used to further buffer the produced hydroxide anions. It is interesting to investigate this since it is closer to cell configurations that achieve higher current densities and Faradaic efficiency and therefore the favored system.

When the gas channel is implemented back into the electrochemical cell it can also be interesting to investigate the effect of the channel thickness. We would assume that the produced gas that lead

to blockage of the thinner catholyte channels could be led away via the gas channel. Therefore it is recommended to research this since according to theory a smaller catholyte channel would result in less ohmic overpotential over the channel.

Finally, the effect of the use of a different membrane such as a Bipolar Membrane (BPM) is interesting to be studied. The use of a BPM leads to acidification near the membrane and with insufficient mixing inside the channel this could lead to a decrease of pH near the membrane while near the cathode the pH increasing. This is interesting to be tested and further researched if this is indeed the case. In this case it is recommended that a different fluorescent dye is used with a more neutral pH range.

Acknowledgements

First, I would like to thank Lorenz Baumgartner for being my daily supervisor. I have learned a lot from you and you have helped me tremendously in shaping this project and your guidance in experiments, writing and planning.

Aside Lorenz I would also like to thank David Vermaas for being the head of the EFS group as well as for your support and knowledge you have shared during this thesis.

I would also like to thank Aron Kahn for his expertise with the FLIM setup. Without him the already 10 hour long experiment days would have gone outside of office hours. Thank you for helping me on those long days and making it more entertaining with some Dutch hits.

I would also like to thank my committee members, Wolter Jager and Hans Geerlings, for taking the time to review my work and help me defend my thesis.

For their technical assistance in the lab I would like to thank Aron, Christiaan and Stefan.

Jorrit Bleeker also deserves my gratitude for helping me in harder times and supporting me in the final writing process by setting some fun bets. I would like to thank you on getting me through these last couple of weeks.

Finally, I would like to thank my parents, sister, boyfriend, friends and roommates. They have been very supportive and were always willing to listen to experimental or theoretical problems even with their lack of expertise on the subject. The TP group also was a fun and supportive group.

Maxime Hoogland
Delft, April 2023

Bibliography

[1] Klimaatberaad, "Klimaatakkoord," 2019. [Online]. Available: https://www.klimaatakkoord.nl/documenten/publicaties/2019/06/28/klimaatakkoord.

[2] P. D. Luna, C. Hahn, D. Higgins, S. A. Jaffer, T. F. Jaramillo, and E. H. Sargent, "What would it take for renewably powered electrosynthesis to displace petrochemical processes?" *Science*, vol. 364, no. 6438, eaav3506, 2019. DOI: 10.1126/science.aav3506. [Online]. Available: https://www.science.org/doi/abs/10.1126/science.aav3506.

[3] W. Smith, T. Burdyny, D. Vermaas, and H. Geerlings, "Pathways to industrial-scale fuel out of thin air from co2 electrolysis," English, *Joule*, vol. 3, no. 8, pp. 1822–1834, 2019, Accepted Author Manuscript, ISSN: 2542-4351. DOI: 10.1016/j.joule.2019.07.009.

[4] D. M. Weekes, D. A. Salvatore, A. Reyes, A. Huang, and C. P. Berlinguette, "Electrolytic co2 reduction in a flow cell," *Accounts of Chemical Research*, vol. 51, no. 4, pp. 910–918, 2018, PMID: 29569896. DOI: 10.1021/acs.accounts.8b00010. eprint: https://doi.org/10.1021/acs.accounts.8b00010. [Online]. Available: https://doi.org/10.1021/acs.accounts.8b00010.

[5] R. G. Grim, Z. Huang, M. T. Guarnieri, J. R. Ferrell, L. Tao, and J. A. Schaidle, "Transforming the carbon economy: Challenges and opportunities in the convergence of low-cost electricity and reductive co2 utilization," *Energy Environ. Sci.*, vol. 13, pp. 472–494, 2 2020. DOI: 10.1039/C9EE02410G. [Online]. Available: http://dx.doi.org/10.1039/C9EE02410G.

[6] M. G. Kibria, J. P. Edwards, C. M. Gabardo, *et al.*, "Electrochemical co2 reduction into chemical feedstocks: From mechanistic electrocatalysis models to system design," *Advanced Materials*, vol. 31, no. 31, p. 1 807 166, 2019. DOI: https://doi.org/10.1002/adma.201807166. eprint: https://onlinelibrary.wiley.com/doi/pdf/10.1002/adma.201807166. [Online]. Available: https://onlinelibrary.wiley.com/doi/abs/10.1002/adma.201807166.

[7] S. Garg, M. Li, A. Z. Weber, *et al.*, "Advances and challenges in electrochemical co2 reduction processes: An engineering and design perspective looking beyond new catalyst materials," *J. Mater. Chem. A*, vol. 8, pp. 1511–1544, 4 2020. DOI: 10.1039/C9TA13298H. [Online]. Available: http://dx.doi.org/10.1039/C9TA13298H.

[8] M. Jouny, W. Luc, and F. Jiao, "General techno-economic analysis of co2 electrolysis systems," *Industrial & Engineering Chemistry Research*, vol. 57, no. 6, pp. 2165–2177, 2018. DOI: 10.1021/acs.iecr.7b03514. eprint: https://doi.org/10.1021/acs.iecr.7b03514. [Online]. Available: https://doi.org/10.1021/acs.iecr.7b03514.

[9] S. Hernández, M. Amin Farkhondehfal, F. Sastre, M. Makkee, G. Saracco, and N. Russo, "Syngas production from electrochemical reduction of co2: Current status and prospective implementation," *Green Chem.*, vol. 19, pp. 2326–2346, 10 2017. DOI: 10.1039/C7GC00398F. [Online]. Available: http://dx.doi.org/10.1039/C7GC00398F.

[10] R. Kas, A. G. Star, K. Yang, T. Van Cleve, K. C. Neyerlin, and W. A. Smith, "Along the channel gradients impact on the spatioactivity of gas diffusion electrodes at high conversions during co2 electroreduction," *ACS Sustainable Chemistry & Engineering*, vol. 9, no. 3, pp. 1286–1296, 2021. DOI: 10.1021/acssuschemeng.0c07694. eprint: https://doi.org/10.1021/acssuschemeng.0c07694. [Online]. Available: https://doi.org/10.1021/acssuschemeng.0c07694.

[11] R. A. Critelli, M. Bertotti, and R. M. Torresi, "Probe effects on concentration profiles in the diffusion layer: Computational modeling and near-surface ph measurements using microelectrodes," *Electrochimica Acta*, vol. 292, pp. 511–521, 2018, ISSN: 0013-4686. DOI: https://doi.org/10.1016/j.electacta.2018.09.157. [Online]. Available: https://www.sciencedirect.com/science/article/pii/S0013468618321534.

[12] N. Pande, S. K. Chandrasekar, D. Lohse, *et al.*, "Electrochemically induced ph change: Time-resolved confocal fluorescence microscopy measurements and comparison with numerical model," *The Journal of Physical Chemistry Letters*, vol. 11, no. 17, pp. 7042–7048, 2020, PMID: 32787336. DOI: 10.1021/acs.jpclett.0c01575. eprint: https://doi.org/10.1021/acs.jpclett.0c01575. [Online]. Available: https://doi.org/10.1021/acs.jpclett.0c01575.

[13] J.-B. Vennekoetter, R. Sengpiel, and M. Wessling, "Beyond the catalyst: How electrode and reactor design determine the product spectrum during electrochemical co2 reduction," *Chemical Engineering Journal*, vol. 364, pp. 89–101, 2019, ISSN: 1385-8947. DOI: https://doi.org/10.1016/j.cej.2019.01.045. [Online]. Available: https://www.sciencedirect.com/science/article/pii/S1385894719300518.

[14] Y. Birdja, E. Pérez-Gallent, M. Figueiredo, A. Göttle, F. Calle-Vallejo, and M. Koper, "Advances and challenges in understanding the electrocatalytic conversion of carbon dioxide to fuels," English, *Nature Energy*, vol. 4, no. 9, pp. 732–745, Sep. 2019, ISSN: 2058-7546. DOI: 10.1038/s41560-019-0450-y.

[15] A. J. Bard and L. R. Faulkner, *Electrochemical methods : fundamentals and applications*, Second edition. Hoboken, NJ: John Wiley & Sons, Inc., 2001, ISBN: 9780471043720.

[16] Y. Hori, "Electrochemical co2 reduction on metal electrodes," in *Modern Aspects of Electrochemistry*, C. G. Vayenas, R. E. White, and M. E. Gamboa-Aldeco, Eds. New York, NY: Springer New York, 2008, pp. 89–189, ISBN: 978-0-387-49489-0. DOI: 10.1007/978-0-387-49489-0_3. [Online]. Available: https://doi.org/10.1007/978-0-387-49489-0_3.

[17] G. Jerkiewicz, "Standard and reversible hydrogen electrodes: Theory, design, operation, and applications," *ACS Catalysis*, vol. 10, no. 15, pp. 8409–8417, 2020. DOI: 10.1021/acscatal.0c02046. eprint: https://doi.org/10.1021/acscatal.0c02046. [Online]. Available: https://doi.org/10.1021/acscatal.0c02046.

[18] S. Liang, N. Altaf, L. Huang, Y. Gao, and Q. Wang, "Electrolytic cell design for electrochemical co2 reduction," *Journal of CO2 Utilization*, vol. 35, pp. 90–105, 2020, ISSN: 2212-9820. DOI: https://doi.org/10.1016/j.jcou.2019.09.007. [Online]. Available: https://www.sciencedirect.com/science/article/pii/S2212982019308261.

[19] S. Hernandez-Aldave and E. Andreoli, "Fundamentals of gas diffusion electrodes and electrolysers for carbon dioxide utilisation: Challenges and opportunities," *Catalysts*, vol. 10, no. 6, 2020, ISSN: 2073-4344. [Online]. Available: https://www.mdpi.com/2073-4344/10/6/713.

[20] B. Endrődi, G. Bencsik, F. Darvas, R. Jones, K. Rajeshwar, and C. Janáky, "Continuous-flow electroreduction of carbon dioxide," *Progress in Energy and Combustion Science*, vol. 62, pp. 133–154, 2017, ISSN: 0360-1285. DOI: https://doi.org/10.1016/j.pecs.2017.05.005. [Online]. Available: https://www.sciencedirect.com/science/article/pii/S0360128517300333.

[21] R. B. Kutz, Q. Chen, H. Yang, S. D. Sajjad, Z. Liu, and I. R. Masel, "Sustainion imidazolium-functionalized polymers for carbon dioxide electrolysis," *Energy Technology*, vol. 5, no. 6, pp. 929–936, 2017. DOI: https://doi.org/10.1002/ente.201600636. eprint: https://onlinelibrary.wiley.com/doi/pdf/10.1002/ente.201600636. [Online]. Available: https://onlinelibrary.wiley.com/doi/abs/10.1002/ente.201600636.

[22] Y. C. Li, Z. Yan, J. Hitt, R. Wycisk, P. N. Pintauro, and T. E. Mallouk, "Bipolar membranes inhibit product crossover in co2 electrolysis cells," *Advanced Sustainable Systems*, vol. 2, no. 4, p. 1 700 187, 2018. DOI: https://doi.org/10.1002/adsu.201700187. eprint: https://onlinelibrary.wiley.com/doi/pdf/10.1002/adsu.201700187. [Online]. Available: https://onlinelibrary.wiley.com/doi/abs/10.1002/adsu.201700187.

[23] M. Ma, S. Kim, I. Chorkendorff, and B. Seger, "Role of ion-selective membranes in the carbon balance for co2 electroreduction via gas diffusion electrode reactor designs," *Chem. Sci.*, vol. 11, pp. 8854–8861, 33 2020. DOI: 10.1039/D0SC03047C. [Online]. Available: http://dx.doi.org/10.1039/D0SC03047C.

[24] B. Endrődi, E. Kecsenovity, A. Samu, *et al.*, "High carbonate ion conductance of a robust piperion membrane allows industrial current density and conversion in a zero-gap carbon dioxide electrolyzer cell," *Energy Environ. Sci.*, vol. 13, pp. 4098–4105, 11 2020. DOI: 10.1039/D0EE02589E. [Online]. Available: http://dx.doi.org/10.1039/D0EE02589E.

[25] D. A. Vermaas and W. A. Smith, “Synergistic electrochemical co2 reduction and water oxidation with a bipolar membrane,” *ACS Energy Letters*, vol. 1, no. 6, pp. 1143–1148, 2016. DOI: 10.1021/acsenergylett.6b00557. eprint: https://doi.org/10.1021/acsenergylett.6b00557. [Online]. Available: https://doi.org/10.1021/acsenergylett.6b00557.

[26] R. A. Tufa, M. A. Blommaert, D. Chanda, Q. Li, D. A. Vermaas, and D. Aili, “Bipolar membrane and interface materials for electrochemical energy systems,” *ACS Applied Energy Materials*, vol. 4, no. 8, pp. 7419–7439, 2021. DOI: 10.1021/acsaem.1c01140. eprint: https://doi.org/10.1021/acsaem.1c01140. [Online]. Available: https://doi.org/10.1021/acsaem.1c01140.

[27] M. A. Blommaert, R. Sharifian, N. U. Shah, N. T. Nesbitt, W. A. Smith, and D. A. Vermaas, “Orientation of a bipolar membrane determines the dominant ion and carbonic species transport in membrane electrode assemblies for co2 reduction,” *J. Mater. Chem. A*, vol. 9, pp. 11 179–11 186, 18 2021. DOI: 10.1039/D0TA12398F. [Online]. Available: http://dx.doi.org/10.1039/D0TA12398F.

[28] Á. Vass, A. Kormányos, Z. Kószó, B. Endrődi, and C. Janáky, “Anode catalysts in co2 electrolysis: Challenges and untapped opportunities,” *ACS Catalysis*, vol. 12, no. 2, pp. 1037–1051, 2022. DOI: 10.1021/acscatal.1c04978. eprint: https://doi.org/10.1021/acscatal.1c04978. [Online]. Available: https://doi.org/10.1021/acscatal.1c04978.

[29] C. C. L. McCrory, S. Jung, J. C. Peters, and T. F. Jaramillo, “Benchmarking heterogeneous electrocatalysts for the oxygen evolution reaction,” *Journal of the American Chemical Society*, vol. 135, no. 45, pp. 16 977–16 987, 2013, PMID: 24171402. DOI: 10.1021/ja407115p. eprint: https://doi.org/10.1021/ja407115p. [Online]. Available: https://doi.org/10.1021/ja407115p.

[30] Á. Vass, B. Endrődi, G. F. Samu, *et al.*, “Local chemical environment governs anode processes in co2 electrolyzers,” *ACS Energy Letters*, vol. 6, no. 11, pp. 3801–3808, 2021. DOI: 10.1021/acsenergylett.1c01937. eprint: https://doi.org/10.1021/acsenergylett.1c01937. [Online]. Available: https://doi.org/10.1021/acsenergylett.1c01937.

[31] A. Peugeot, C. E. Creissen, M. W. Schreiber, and M. Fontecave, “Advancing the anode compartment for energy efficient co2 reduction at neutral ph,” *ChemElectroChem*, vol. 8, no. 14, pp. 2726–2736, 2021. DOI: https://doi.org/10.1002/celc.202100742. eprint: https://chemistry-europe.onlinelibrary.wiley.com/doi/pdf/10.1002/celc.202100742. [Online]. Available: https://chemistry-europe.onlinelibrary.wiley.com/doi/abs/10.1002/celc.202100742.

[32] J.-B. Vennekötter, T. Scheuermann, R. Sengpiel, and M. Wessling, “The electrolyte matters: Stable systems for high rate electrochemical co2 reduction,” *Journal of CO2 Utilization*, vol. 32, pp. 202–213, 2019, ISSN: 2212-9820. DOI: https://doi.org/10.1016/j.jcou.2019.04.007. [Online]. Available: https://www.sciencedirect.com/science/article/pii/S2212982019301817.

[33] G. Marcandalli, M. C. O. Monteiro, A. Goyal, and M. T. M. Koper, “Electrolyte effects on co2 electrochemical reduction to co,” *Accounts of Chemical Research*, vol. 55, no. 14, pp. 1900–1911, 2022, PMID: 35772054. DOI: 10.1021/acs.accounts.2c00080. eprint: https://doi.org/10.1021/acs.accounts.2c00080. [Online]. Available: https://doi.org/10.1021/acs.accounts.2c00080.

[34] M. C. Monteiro, F. Dattila, B. Hagedoorn, R. García-Muelas, N. López, and M. Koper, “Absence of co2 electroreduction on copper, gold and silver electrodes without metal cations in solution,” *Nature Catalysis*, vol. 4, no. 8, pp. 654–662, 2021.

[35] A. Xu, N. Govindarajan, G. Kastlunger, S. Vijay, and K. Chan, “Theories for electrolyte effects in co2 electroreduction,” *Accounts of Chemical Research*, vol. 55, no. 4, pp. 495–503, 2022, PMID: 35107967. DOI: 10.1021/acs.accounts.1c00679. eprint: https://doi.org/10.1021/acs.accounts.1c00679. [Online]. Available: https://doi.org/10.1021/acs.accounts.1c00679.

[36] M. R. Singh, Y. Kwon, Y. Lum, J. W. Ager, and A. T. Bell, “Hydrolysis of electrolyte cations enhances the electrochemical reduction of co2 over ag and cu,” *Journal of the American Chemical Society*, vol. 138, no. 39, pp. 13 006–13 012, 2016, PMID: 27626299. DOI: 10.1021/jacs.6b07612. eprint: https://doi.org/10.1021/jacs.6b07612. [Online]. Available: https://doi.org/10.1021/jacs.6b07612.

[37] K. N. Han, “Characteristics of precipitation of rare earth elements with various precipitants,” *Minerals*, vol. 10, no. 2, p. 178, 2020.

[38] S. Verma, X. Lu, S. Ma, R. I. Masel, and P. J. A. Kenis, “The effect of electrolyte composition on the electroreduction of co2 to co on ag based gas diffusion electrodes,” *Phys. Chem. Chem. Phys.*, vol. 18, pp. 7075–7084, 10 2016. DOI: 10.1039/C5CP05665A. [Online]. Available: http://dx.doi.org/10.1039/C5CP05665A.

[39] C. J. Bondue, M. Graf, A. Goyal, and M. T. M. Koper, “Suppression of hydrogen evolution in acidic electrolytes by electrochemical co2 reduction,” *Journal of the American Chemical Society*, vol. 143, no. 1, pp. 279–285, 2021, PMID: 33356205. DOI: 10.1021/jacs.0c10397. eprint: https://doi.org/10.1021/jacs.0c10397. [Online]. Available: https://doi.org/10.1021/jacs.0c10397.

[40] V. Chiriac and G. Balea, “Buffer index and buffer capacity for a simple buffer solution,” *Journal of chemical education*, vol. 74, no. 8, p. 937, 1997.

[41] N. Gupta, M. Gattrell, and B. MacDougall, “Calculation for the cathode surface concentrations in the electrochemical reduction of co2 in khco3 solutions,” *Journal of Applied Electrochemistry*, vol. 36, Jan. 2006. DOI: 10.1007/s10800-005-9058-y.

[42] K. G. Schulz, U. Riebesell, B. Rost, S. Thoms, and R. Zeebe, “Determination of the rate constants for the carbon dioxide to bicarbonate inter-conversion in ph-buffered seawater systems,” *Marine chemistry*, vol. 100, no. 1-2, pp. 53–65, 2006.

[43] T. L. Bergman, T. L. Bergman, F. P. Incropera, D. P. Dewitt, and A. S. Lavine, *Fundamentals of heat and mass transfer*. John Wiley & Sons, 2011.

[44] D. Pickett and K. Ong, “The influence of hydrodynamic and mass transfer entrance effects on the operation of a parallel plate electrolytic cell,” *Electrochimica Acta*, vol. 19, no. 12, pp. 875–882, 1974, ISSN: 0013-4686. DOI: https://doi.org/10.1016/0013-4686(74)85036-X. [Online]. Available: https://www.sciencedirect.com/science/article/pii/001346867485036X.

[45] T. Ralph, M. Hitchman, J. Millington, and F. Walsh, “Mass transport in an electrochemical laboratory filterpress reactor and its enhancement by turbulence promoters,” *Electrochimica Acta*, vol. 41, no. 4, pp. 591–603, 1996, Electrochemical Engineering, ISSN: 0013-4686. DOI: https://doi.org/10.1016/0013-4686(95)00346-0. [Online]. Available: https://www.sciencedirect.com/science/article/pii/0013468695003460.

[46] L.-C. Weng, A. T. Bell, and A. Z. Weber, “Modeling gas-diffusion electrodes for co2 reduction,” *Phys. Chem. Chem. Phys.*, vol. 20, pp. 16 973–16 984, 25 2018. DOI: 10.1039/C8CP01319E. [Online]. Available: http://dx.doi.org/10.1039/C8CP01319E.

[47] H. Hashiba, L.-C. Weng, Y. Chen, *et al.*, “Effects of electrolyte buffer capacity on surface reactant species and the reaction rate of co2 in electrochemical co2 reduction,” *The Journal of Physical Chemistry C*, vol. 122, no. 7, pp. 3719–3726, 2018. DOI: 10.1021/acs.jpcc.7b11316. eprint: https://doi.org/10.1021/acs.jpcc.7b11316. [Online]. Available: https://doi.org/10.1021/acs.jpcc.7b11316.

[48] D. Salvatore and C. P. Berlinguette, “Voltage matters when reducing co2 in an electrochemical flow cell,” *ACS Energy Letters*, vol. 5, no. 1, pp. 215–220, 2020. DOI: 10.1021/acsenergylett.9b02356. eprint: https://doi.org/10.1021/acsenergylett.9b02356. [Online]. Available: https://doi.org/10.1021/acsenergylett.9b02356.

[49] H. Vogt, “The concentration overpotential of gas evolving electrodes as a multiple problem of mass transfer,” *Journal of The Electrochemical Society*, vol. 137, no. 4, pp. 1179–1184, Apr. 1990. DOI: 10.1149/1.2086624. [Online]. Available: https://doi.org/10.1149/1.2086624.

[50] A. Angulo, P. van der Linde, H. Gardeniers, M. Modestino, and D. Fernández Rivas, “Influence of bubbles on the energy conversion efficiency of electrochemical reactors,” *Joule*, vol. 4, no. 3, pp. 555–579, 2020, ISSN: 2542-4351. DOI: https://doi.org/10.1016/j.joule.2020.01.005. [Online]. Available: https://www.sciencedirect.com/science/article/pii/S2542435120300325.

[51] A. Taqieddin, Y. Liu, A. N. Alshawabkeh, and M. R. Allshouse, "Computational modeling of bubbles growth using the coupled level set—volume of fluid method," *Fluids*, vol. 5, no. 3, 2020, ISSN: 2311-5521. DOI: 10.3390/fluids5030120. [Online]. Available: https://www.mdpi.com/2311-5521/5/3/120.

[52] D. A. Henckel, M. J. Counihan, H. E. Holmes, *et al.*, "Potential dependence of the local ph in a co2 reduction electrolyzer," *ACS Catalysis*, vol. 11, no. 1, pp. 255–263, 2021. DOI: 10.1021/acscatal.0c04297. eprint: https://doi.org/10.1021/acscatal.0c04297. [Online]. Available: https://doi.org/10.1021/acscatal.0c04297.

[53] M. C. Monteiro and M. T. Koper, "Measuring local ph in electrochemistry," *Current Opinion in Electrochemistry*, vol. 25, p. 100 649, 2021, ISSN: 2451-9103. DOI: https://doi.org/10.1016/j.coelec.2020.100649. [Online]. Available: https://www.sciencedirect.com/science/article/pii/S2451910320301903.

[54] J. R. Lakowicz, H. Szmacinski, K. Nowaczyk, K. W. Berndt, and M. Johnson, "Fluorescence lifetime imaging," *Analytical Biochemistry*, vol. 202, no. 2, pp. 316–330, 1992, ISSN: 0003-2697. DOI: https://doi.org/10.1016/0003-2697(92)90112-K. [Online]. Available: https://www.sciencedirect.com/science/article/pii/000326979290112K.

[55] R. Datta, T. M. Heaster, J. T. Sharick, A. A. Gillette, and M. C. Skala, "Fluorescence lifetime imaging microscopy: fundamentals and advances in instrumentation, analysis, and applications," *Journal of Biomedical Optics*, vol. 25, no. 7, p. 071 203, 2020. DOI: 10.1117/1.JBO.25.7.071203. [Online]. Available: https://doi.org/10.1117/1.JBO.25.7.071203.

[56] W. F. Jager, T. S. Hammink, O. van den Berg, and F. C. Grozema, "Highly sensitive water-soluble fluorescent ph sensors based on the 7-amino-1-methylquinolinium chromophore," *The Journal of Organic Chemistry*, vol. 75, no. 7, pp. 2169–2178, 2010, PMID: 20196564. DOI: 10.1021/jo902225k. eprint: https://doi.org/10.1021/jo902225k. [Online]. Available: https://doi.org/10.1021/jo902225k.

[57] D. M. Jameson and T. L. Hazlett, "Time-resolved fluorescence in biology and biochemistry," in *Biophysical and Biochemical Aspects of Fluorescence Spectroscopy*, T. G. Dewey, Ed. Boston, MA: Springer US, 1991, pp. 105–133, ISBN: 978-1-4757-9513-4. DOI: 10.1007/978-1-4757-9513-4_4. [Online]. Available: https://doi.org/10.1007/978-1-4757-9513-4_4.

[58] W. BECKER, "Fluorescence lifetime imaging – techniques and applications," *Journal of Microscopy*, vol. 247, no. 2, pp. 119–136, 2012. DOI: https://doi.org/10.1111/j.1365-2818.2012.03618.x. eprint: https://onlinelibrary.wiley.com/doi/pdf/10.1111/j.1365-2818.2012.03618.x. [Online]. Available: https://onlinelibrary.wiley.com/doi/abs/10.1111/j.1365-2818.2012.03618.x.

[59] H. Kaneko, I. Putzier, S. Frings, U. B. Kaupp, and T. Gensch, "Chloride accumulation in mammalian olfactory sensory neurons," *Journal of Neuroscience*, vol. 24, no. 36, pp. 7931–7938, 2004, ISSN: 0270-6474. DOI: 10.1523/JNEUROSCI.2115-04.2004. eprint: https://www.jneurosci.org/content/24/36/7931.full.pdf. [Online]. Available: https://www.jneurosci.org/content/24/36/7931.

[60] W. Zhang, X. Chen, Y. Wang, L. Wu, and Y. Hu, "Experimental and modeling of conductivity for electrolyte solution systems," *ACS Omega*, vol. 5, no. 35, pp. 22 465–22 474, 2020, PMID: 32923805. DOI: 10.1021/acsomega.0c03013. eprint: https://doi.org/10.1021/acsomega.0c03013. [Online]. Available: https://doi.org/10.1021/acsomega.0c03013.

[61] C. Lee, B. Zhao, J. K. Lee, K. F. Fahy, K. Krause, and A. Bazylak, "Bubble formation in the electrolyte triggers voltage instability in co2 electrolyzers," *iScience*, vol. 23, no. 5, p. 101 094, 2020, ISSN: 2589-0042. DOI: https://doi.org/10.1016/j.isci.2020.101094. [Online]. Available: https://www.sciencedirect.com/science/article/pii/S2589004220302790.

[62] S. Weisenberger and A. Schumpe, "Estimation of gas solubilities in salt solutions at temperatures from 273 k to 363 k," *AIChE Journal*, vol. 42, no. 1, pp. 298–300, 1996. DOI: https://doi.org/10.1002/aic.690420130. eprint: https://aiche.onlinelibrary.wiley.com/doi/pdf/10.1002/aic.690420130. [Online]. Available: https://aiche.onlinelibrary.wiley.com/doi/abs/10.1002/aic.690420130.

[63] R. Sander, “Compilation of henry’s law constants (version 4.0) for water as solvent,” *Atmospheric Chemistry and Physics*, vol. 15, no. 8, pp. 4399–4981, 2015. DOI: 10.5194/acp-15-4399-2015. [Online]. Available: https://acp.copernicus.org/articles/15/4399/2015/.

[64] A. Schumpe, “The estimation of gas solubilities in salt solutions,” *Chemical Engineering Science*, vol. 48, no. 1, pp. 153–158, 1993, ISSN: 0009-2509. DOI: https://doi.org/10.1016/0009-2509(93)80291-W. [Online]. Available: https://www.sciencedirect.com/science/article/pii/000925099380291W.

A

Cell assembly images of the electrochemical cell

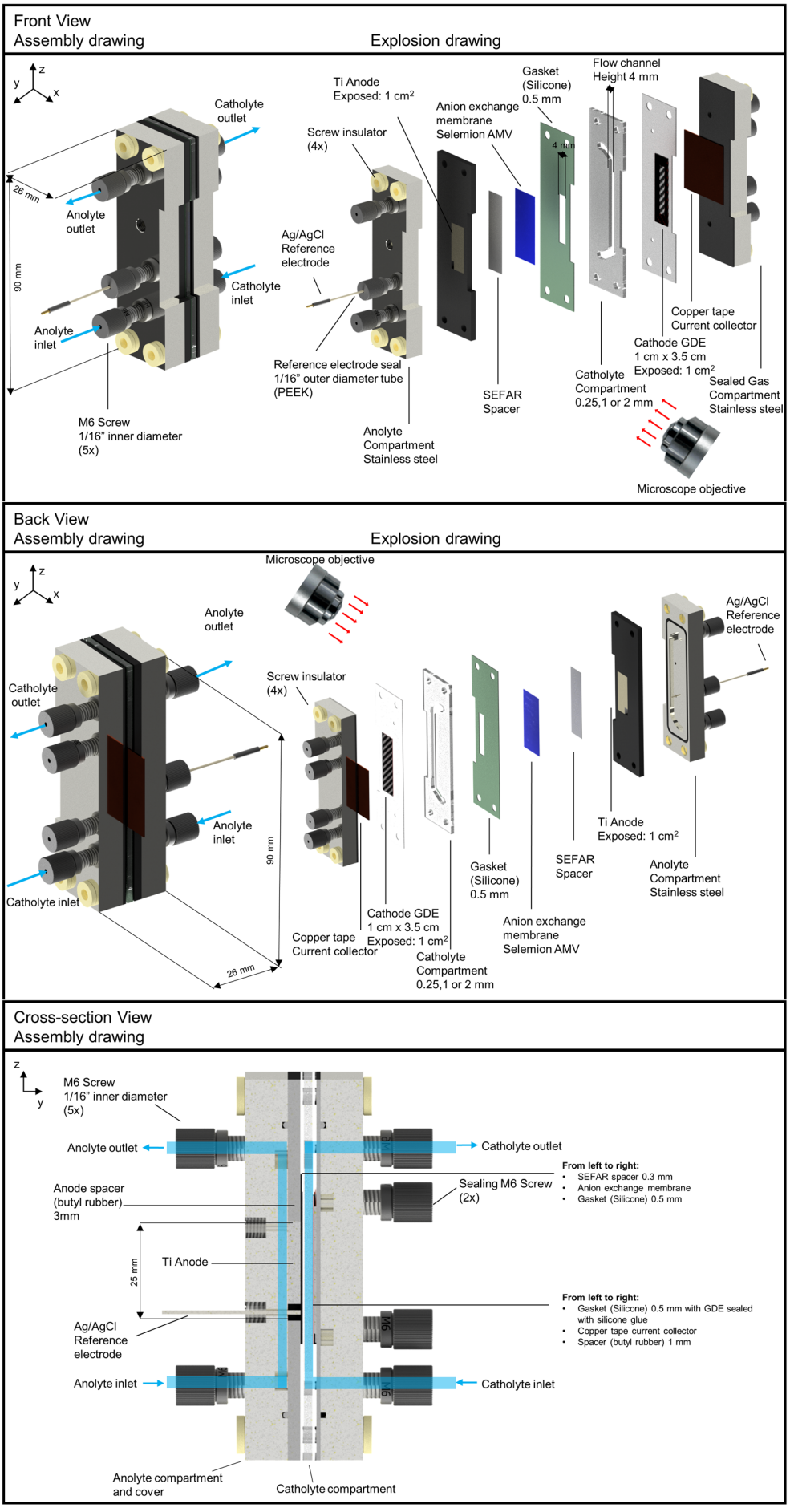

Figure A.1: Cell assembly images of the electrochemical cell used for CO_2 electrolysis including indications of the direction of the flow, measurements for the cell and its parts.

B

Calculations for the CO_2 and ion concentrations

B.1. Calculations for the CO_2 concentration at $292.15\,\mathrm{K}$

The concentration of CO_2 can be calculated from the Henry's constant and the CO_2 partial pressure.

$$c_{CO_2} = H_{CO_2} \cdot p_{CO_2} \tag{B.1}$$

We can correct Henry's constant for the right temperature using the Van 't Hoff equation and rewriting this equation to obtain a relation for the Henry's constant as a function of the temperature.

$$\frac{d \ln H_{CO_2}}{dT} = \frac{\Delta_{sol} H_{CO_2}}{RT^2} \tag{B.2}$$

$$H_{CO_2}(T) = H_{CO_2,ref} \exp\left\{ \frac{-\Delta_{sol} H_{CO_2}}{R} \left(\frac{1}{T} - \frac{1}{T_{ref}} \right) \right\} \tag{B.3}$$

In this equation we have the following parts: $\Delta_{sol} H_{CO_2}$ is the enthalpy of CO_2 dissolution, T_{ref} the reference temperature, T the temperature, $H_{CO_2,ref}$ the reference Henry's constant and R the universal gas constant. We use the following values to calculate this temperature dependent Henry's constant [62], [63]. We first show the Henry's constant followed by the concentration of CO_2.

$$\begin{aligned} T_{ref} &= 298.15\,\mathrm{K} \\ T &= 292.15\,\mathrm{K} \\ H_{CO_2,ref} &= 3.3 \times 10^{-4}\,\mathrm{mol\,m^{-3}\,Pa} \\ \frac{-\Delta_{sol} H_{CO_2}}{R} &= 2400\,\mathrm{K} \end{aligned}$$

$$H_{CO_2} = 3.8932 \times 10^{-4}\,\mathrm{mol\,m^{-3}\,Pa^{-1}} \text{ at } T = 292.15\,\mathrm{K}$$

$$c_{CO_2} = H_{CO_2} \cdot p_{CO_2} = 39.448\,\mathrm{mol\,m^3} \text{ with } P_{CO_2} = 101\,325\,\mathrm{Pa}$$

B.2. Calculations for the ion concentrations in the saturated electrolyte

To obtain the ion concentrations for the different electrolytes the following calculations need to be made. A system is setup with three equations and either of the two charge balances (dependent on the electrolyte) to solve the four unknowns: $c_{HCO_3^-}$, $c_{CO_3^{2-}}$, c_{OH^-} and c_{H^+}.

$$c_{OH^-}\, c_{H^+} = K_W = 1 \times 10^{-14}\,\text{mol}^2\,\text{L}^{-2} \tag{B.4}$$

$$\frac{c_{HCO_3^-}}{c_{CO_3^{2-}}\, c_{OH^-}} = K_1 = 4.44 \times 10^{7}\,\text{mol}\,\text{L}^{-1} \tag{B.5}$$

$$\frac{c_{CO_3^{2-}}}{c_{HCO_3^-}\, c_{OH^-}} = K_2 = 4.66 \times 10^{3}\,\text{mol}\,\text{L}^{-1} \tag{B.6}$$

$$c_{K^+} + c_{H^+} = c_{HCO_3^-} + 2c_{CO_3^{2-}} + c_{OH^-} \tag{B.7}$$

$$c_{K^+} + c_{H^+} = c_{HCO_3^-} + 2c_{CO_3^{2-}} + c_{OH^-} + 2c_{SO_2^{2-}} \tag{B.8}$$

B.3. Calculations for the CO_2 concentration taking into account salting-out effects

The salting-out effect is the effect of the gas solubility decreasing with an increasing salt concentration. It is given by the following equation where we find a relation between $c_{g,0}$, the solubility of the gas in pure water, and c_g, the solubility of that gas in a liquid with salt concentration c_s. We have a constant K that is specific for the gas and salt.

$$\log \frac{c_{g,0}}{c_g} = K c_s \tag{B.9}$$

In a case where we have multiple salts in the liquid the equation is as follows [64]:

$$\log \frac{c_{g,0}}{c_g} = \sum \left(h_i + h_G\right) c_i \tag{B.10}$$

In this equation we have multiple constants specific per ion (h_i and h_G) and its concentration (c_i). h_G is temperature dependent and is calculated with Equation B.11.

$$h_G = h_{G,0} + h_T \left(T - 298.15\,\text{K}\right) \tag{B.11}$$

By rewriting we can summarize the multiple specific constants per salt in K_s. We have given the parameters to estimate this constant in Table B.1. This K_s we can implement back into Equation B.13.

$$K_s = \sum_i \left(h_i + h_G\right) n_i \tag{B.12}$$

$$\log \frac{c_{g,0}}{c_g} = \sum_s K_s c_s \tag{B.13}$$

Table B.1: Parameters to estimate K_s. [62]

Parameter	Unit	Species	Value
		H^+	0
		K^+	0.0922
h_i	[$m^3\,kmol^{-1}$]	OH^-	0.0839
		HCO_3^-	0.0967
		CO_3^{2-}	0.1423
		SO_4^{2-}	0.1117
$h_{G,0}$	[$m^3\,kmol^{-1}$]	CO_2	−0.0172
$h_T \times 10^3$	[$m^3\,kmol^{-1}\,K^{-1}$]	CO_2	−0.338

From Table B.1 and Equation B.11 we can calculate h_G for CO_2. We can also calculate the values for the different salts from Table B.1. These are given in Table B.2.

$$h_G = -0.0152\,\text{K} \tag{B.14}$$

Table B.2: K_s calculated for the four different salts present in the electrolytes [62].

Salt	K_s [$m^3\,kmol^{-1}$]
$KHCO_3$	0.1586
K_2CO_3	0.2812
KOH	0.1458
K_2SO_4	0.2506

Combining Equation B.13 and Equation B.1 and rewriting we obtain the last two equations. We can use these to calculate the Henry's constants that takes into account the salting-out effect.

$$\log \frac{H_{CO_2,T=292.15K} p_{CO_2}}{H_{CO_2} p_{CO_2}} = \sum_s K_s c_s \tag{B.15}$$

$$H_{CO_2} = H_{CO_2,T=292.15K} \cdot 10^{-\left(K_{KHCO_3} c_{HCO_3^-} + K_{K_2CO_3} c_{CO_3^{2-}} + K_{KOH} c_{OH^-} + K_{K_2SO_4} c_{SO_4^{2-}}\right)} \tag{B.16}$$

Table B.3 shows us the concentration of CO_2, the four ions and the calculated pH.

Table B.3: Equilibrium values with taking into account the salting-out effect for CO_2, HCO_3^-, HCO_3^{2-}, OH^- and the measured and calculated pH at different electrolyte concentrations and types at 19 °C and 101 325 Pa CO_2 partial pressure.

Electrolyte	$c_{CO_{2(aq)}}$	$c_{HCO_3^-}$	$c_{CO_3^{2-}}$	c_{OH^-}	**$pH_{calculated}$**
0.4 M K_2SO_4	0.0313	1.18×10^{-4}	4.66×10^{-11}	8.48×10^{-11}	3.93
0.1 M $KHCO_3$	0.0380	0.099	2.76×10^{-5}	5.92×10^{-8}	6.77
1 M $KHCO_3$	0.0274	0.992	3.77×10^{-3}	8.16×10^{-7}	7.91

C

Calculations to obtain the theoretical pH change over the channel

To determine the pH change over the channel due to the production of hydroxide ions we first determine the initial concentrations of the ions: $c_{HCO_3^-}$, $c_{CO_3^{2-}}$, c_{OH^-} and c_{H^+}. We also assume the CO_2 concentration being equal to the concentration at $T = 292.15\,\text{K}$ and a partial pressure of CO_2 of $101\,325\,\text{Pa}$. $CO_2 = 39\,\text{mol}\,\text{m}^{-3}$. These calculations follow the way described in Appendix A.
From this we obtain the following initial values, or the concentration of the ions at the start of the electrode:

$$c^i_{HCO_3^-}$$
$$c^i_{CO_3^{2-}}$$
$$c^i_{OH^-}$$
$$c^i_{H^+}$$

In the electrolyte channel multiple processes are taking place:

- The production of OH^- ions via the HER. We assume that only HER is taking place as the electrochemical reaction. This leads to a simplification since we can eliminate the consumption of CO_2 in COER.
- The consumption of bicarbonate and carbonate ions. These are not consumed but move through the membrane and therefore can no longer play a role in the catholyte. We assume that for every OH^- ion $1/2$ bicarbonate ion and $1/4$ carbonate ion moves through the membrane. This is also to ensure charge balance over the electrolyte.
- The three buffering reactions are taking place. These are the formation of bicarbonate from hydroxide and aqueous CO_2 (R1), the formation of carbonate from bicarbonate and hydroxide (R2) and the dissociation reaction of water (RW).

We want to obtain the concentration of the species at the middle of the channel, because this is also the part we obtain an image over using FLIM.

The first process, the production of OH^- (P_{OH^-} in $\text{mol}\,\text{m}^{-3}$), is described by the following equations over half the length of the channel. These equations can also be related to the consumption of bicarbonate and carbonate ions.

$$P_{OH^-} = \frac{N_{OH^-}}{\dot{V}} \cdot \frac{y_{\text{half}}}{y_{\text{total}}} \tag{C.1}$$

$$N_{OH^-} = \frac{i}{nF} \tag{C.2}$$

We use $\dot{V}$ the volumetric flow rate in $\text{m}^3\,\text{s}^{-1}$ calculated from the liquid flow rate, N_{OH^-} the moles of OH^- being produced in $\text{mol}\,\text{s}^{-1}$ from i the current applied, n the number of electrons involved in the

equations and F the Faraday constant.

The third process of the buffering reactions is given in the equation below. This equation give the production or consumption of each of the species, i. $\nu_{\#,1}$ are the stoichiometric coefficients of the species i in the buffering reaction as indicated by the number or W. Number 1 is the formation of bicarbonate, 2 the formation of carbonate and W the dissociation reaction of water. The forward and backward rate constants of the buffering reactions are given by $k_{\#,f/b}$

$$\begin{aligned} R_i =& \nu_{1,i}(k_{1,f}c^f_{CO_2}c^f_{OH^-} - k_{1,b}c^f_{HCO_3^-}) \\ & \nu_{2,i}(k_{2,f}c^f_{HCO_3^-}c^f_{OH^-} - k_{2,b}c^f_{CO_3^{2-}}) \\ & \nu_{W,i}(k_{W,f} - k_{W,b}c^f_{OH^-}c^f_{H^+}) \end{aligned} \tag{C.3}$$

Mass balances were set up over the catholyte channel. The final concentration of the species (c^f_i) are calculated as follows:

$$c^f_{OH^-} = c^i_{OH^-} + P_{OH^-} + \frac{R_{OH^-}V}{\dot{V}} \tag{C.4}$$

$$c^f_{HCO_3^-} = c^i_{HCO_3^-} - \frac{1}{2}P_{OH^-} + \frac{R_{HCO_3^-}V}{\dot{V}} \tag{C.5}$$

$$c^f_{CO_3^{2-}} = c^i_{CO_3^{2-}} - \frac{1}{4}P_{OH^-} + \frac{R_{CO_3^{2-}}V}{\dot{V}} \tag{C.6}$$

$$c^f_{H^+} = c^i_{H^+} + \frac{R_{H^+}V}{\dot{V}} \tag{C.7}$$

$$c^f_{CO_2} = c^i_{CO_2} + \frac{R_{CO_2}V}{\dot{V}} \tag{C.8}$$

In these equations we also have $\dot{V}$ the volumetric flow rate in $m^3\,s^{-1}$ calculated from the liquid flow rate and $V = zy_{half}W$ the volume already passed with the width of the electrode $z = 0.4$ cm, the width of the catholyte channel $W = 0.2$ cm and $y_{half} = 1.25$ cm.

From the final concentration of OH^- we calculate the pH.

D

Buffer capacity of different buffering species in the electrolyte

In Table D.1 an overview of the buffer capacities of all the species inside the different electrolytes are given. From this we can determine the main buffering species inside the electrolyte. Especially for 0.4 M K_2SO_4 this is interesting since we did not take into account the buffering of the aqueous CO_2 in the previous buffer capacity calculations as given in Table 4.1.

Table D.1: An overview of the buffer capacity (β) for each of the buffering species present in the electrolytes.

	0.1 M KHCO3		**1 M KHCO3**		**0.4 K2SO4**		
HA	H_2CO_3	HCO_3^-	H_2CO_3	HCO_3^-	HSO_4^{2-}	H_2CO_3	HCO_3^-
H^-	HCO_3^-	CO_3^{2-}	HCO_3^-	CO_3^{2-}	SO_4^{2-}	HCO_3^-	CO_3^{2-}
pH	6.6	6.6	7.44	7.44	5.3	5.3	5.3
pKa	6.38	10.34	6.38	10.34	2	6.38	10.34
$Ka =$	4.2×10^{-7}	4.6×10^{-11}	4.2×10^{-7}	4.6×10^{-11}	0.01	4.2×10^{-7}	4.6×10^{-11}
C_{total}	1.39×10^{-1}	0.1	1.039	1.0026	0.4	3.90×10^{-2}	1.30×10^{-4}
β	**7.50E-02**	**4.18E-05**	**1.76E-01**	**2.90E-03**	**4.61E-04**	**6.36E-03**	**2.73E-09**

E

Effect of the channel width on the potential

In this appendix the effect of the channel width of the cell potential is discussed. In Figure E.1 the cell potential is displayed over the channel width. This is done for the 1 M $KHCO_3$ electrolyte case at an applied current of $-50\,\mathrm{mA\,cm^{-2}}$.

In this figure we see a decreasing cell potential with increasing channel width for the two higher Reynolds numbers ($Re = 8 \text{and} 47$). We would expect at least the ohmic part over the electrolyte channel to decrease with decreasing channel width. This is linked to the relation of the ohmic drop over the electrolyte to the width of the channel (l): $\eta_{\text{electrolyte}} = \frac{jl}{\kappa}$.

With this relation we cannot explain the increasing cell potential with decreasing channel width. We therefore come up with a more likely explanation of this high potential. We expect that bubbles are getting stuck inside the thinner channels. Since the fraction of gas is higher in a smaller channel we think this reduces the effective conductivity of the electrolyte. This results in a higher potential.

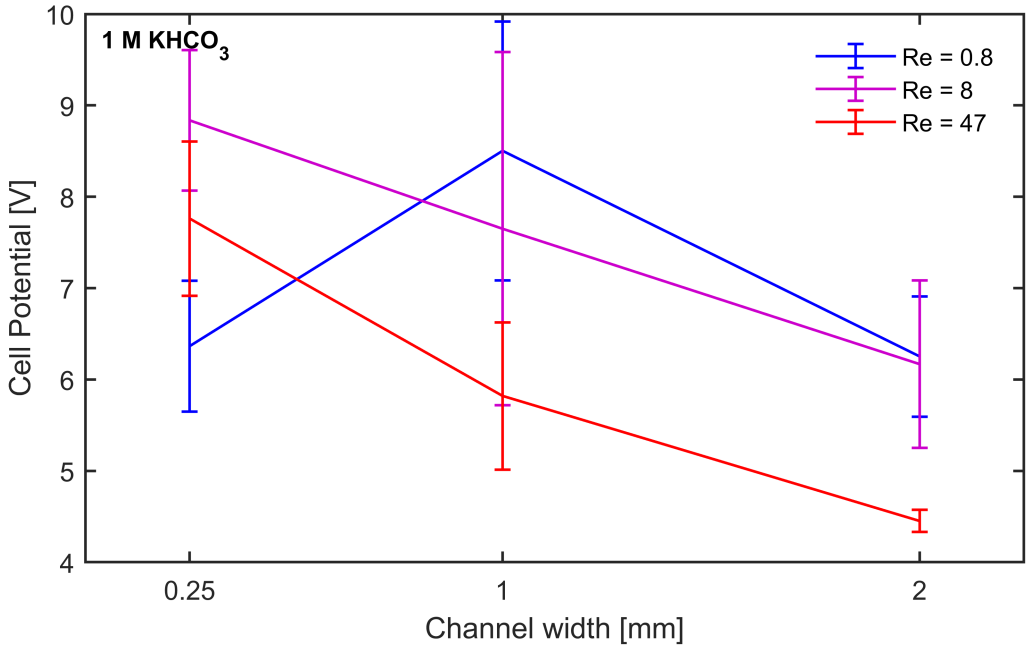

Figure E.1: The cell potential displayed in V over the channel width in mm for the three Reynolds numbers. The case is 1 M $KHCO_3$ electrolyte at $-50\,\mathrm{mA\,cm^{-2}}$.

The channel width has some counter-intuitive effects on the cell potential distribution. These are most likely do to the bubble formation and two-phase flow dynamics. Therefore we would recommend to further study the efficient removal of bubbles for thinner channels. Since this can decrease the cell potential by several volts.

From Figure E.1 we can also see the large error bars for the smaller channel width. Aside this we did not obtain any FLIM results on the smaller channels and the 1 mm was only tested for one electrolyte. For these reasons we have not looked further into the results for the smaller channel width.